Pre-supernova Neutrinos at Super-Kamiokande with Gadolinium

Charles H. Simpson

Keble College, Oxford

Trinity Term, 2019

Thesis submitted in partial fulfilment of the requirements for the degree of Doctor of Philosophy at the University of Oxford

Abstract

Supernova detection is a major objective of the Super-Kamiokande (SK) experiment. In the next stage of SK (SK-Gd), gadolinium (Gd) sulfate will be added to the detector, which will improve the ability of the detector to identify neutrons. A core-collapse supernova will be preceded by an increasing flux of neutrinos and anti-neutrinos, from thermal and weak nuclear processes in the star, over a timescale of hours; some of which may be detected at SK-Gd. This could provide an early warning of an imminent core-collapse supernova, hours earlier than the detection of the neutrinos from core collapse. Electron anti-neutrino detection will rely on inverse beta decay events below the usual analysis energy threshold of SK, so Gd loading is vital to reduce backgrounds while maximising detection efficiency. Assuming normal neutrino mass ordering, more than 200 events could be detected in the final 12 hours before core collapse for a 15-25 solar mass star at around 200 pc, which is representative of the nearest red supergiant to Earth, α Ori (Betelgeuse). At a statistical false alarm rate of 1 per century, detection could be up to 10 hours before core collapse, and a pre-supernova star could be detected by SK-Gd up to 600 pc away. A pre-supernova alert could be provided to the astrophysics community following gadolinium loading.

Acknowledgements

This degree took me away from home for a long time; I'd like to thank my friends and family in the UK, especially Mansi, for putting up with my absence. Thank you to my friends and colleagues at Kamioka Observatory and in Oxford for welcoming me and teaching me so much, and the support staff who made it all possible.

Thanks to Mark for suggesting the project. Thanks also to everyone who helped me in some way with this project, or asked useful questions; especially Nakahata, Michael, and Dave.

Contents

1 Introduction **1**

2 Neutrinos **3**

2.1 The State of the Art 4

2.2 Neutrino Interactions 6

2.3 Three Neutrinos 9

2.4 The MSW Effect 13

3 Supernovae and Pre-supernovae **16**

3.1 Stellar Evolution 19

3.2 Supernova Explosion Mechanism 26

3.3 SN1987A 30

3.4 21^{st} Century Supernova Neutrino Detection 33

3.5 Supernova Relic Neutrinos 35

3.6 Pre-SN Neutrino Signal 39

4 The Super-Kamiokande Detector **48**

4.1 Cherenkov Emission 48

4.2 Periods of Data Collection 49

4.3 Detector Structure 50
4.4 Water Systems 55
4.4.1 Pure Water 55
4.4.2 $Gd_2(SO_4)_3$ Loaded Water 56
4.5 DAQ and Electronics 61
4.6 Trigger Conditions 63
4.7 WIT 65
4.8 Calibration 66
4.9 Event Reconstruction 70
4.9.1 Vertex Reconstruction 70
4.9.2 Direction Reconstruction 72
4.9.3 Energy Reconstruction 73
4.9.4 Isotropy Parameters 74

5 Gadolinium Loading **78**
5.1 Motivation 79
5.2 Radiopurity 82
5.3 EGADS 87
5.4 Monitoring Gd Concentration 93
5.5 Simulation Studies on the Characteristics of Emitted γ-rays . 97
5.6 Measurements in EGADS 105
5.7 Summary 107

6 Detecting Low Energy IBD at SK-Gd **108**
6.1 Thresholds and Triggering 109
6.2 Sources of Background 111

6.2.1 Intrinsic Background . . . 111
6.2.2 Additional Radioactive Decay Backgrounds . . . 112
6.2.3 Spallation . . . 113
6.3 Reactor Neutrinos . . . 117
6.4 Single Neutron Event Selection . . . 118
6.5 Delayed Coincidence Event Selection . . . 126
6.5.1 Spatial Distribution . . . 126
6.5.2 Timing Distribution . . . 127
6.5.3 Initial Search . . . 127
6.6 Results . . . 130

7 Multivariate Selection 131
7.1 Introduction . . . 131
7.2 Training Considerations . . . 135
7.3 Method . . . 136
7.4 Results . . . 139
7.4.1 Hyperparameters . . . 139
7.4.2 Variable Inclusion . . . 139
7.4.3 Performance . . . 152
7.4.4 Variability . . . 154

8 Sensitivity to Pre-SN Neutrinos 156
8.1 Implementation . . . 157
8.2 Previous Estimates . . . 158
8.3 Final Selection . . . 160
8.4 Detection Strategy . . . 163

8.5 Baseline Results 167
8.6 Low Loading Case 174
8.7 Stability of Event Rate 175
8.8 Next Generation Detectors 179
8.9 Combining Multiple Detectors 186

9 Conclusion **187**

Appendices

A Catalogue of Nearby RSGs **191**

List of Figures

2.1 Effective neutrino cross sections taking into account threshold and resolution effects for a water Cherenkov detector. 7

2.2 IBD cross section against neutrino energy using accurate approximation from [1]. 8

3.1 The evolutionary paths of stellar models with two different initial masses are plotted in core temperature and density. . . 20

3.2 Temperature dependence of energy generation by fusion and energy loss by neutrino emission. 22

3.3 Feynman diagrams of some processes leading to thermal neutrino emission. 24

3.4 Characteristics of stellar burning for example stars. 25

3.5 A pre-SN star contains concentric shells of species with decreasing mass number. 27

3.6 Neutrino luminosity (top left), and energy (bottom left) against time from core bounce, and neutrino energy spectrum (right) at various times. 30

3.7 Energy distribution of neutrinos detected in coincidence with SN1987A. 32
3.8 Predictions of DSNB flux spectrum, compared to other neutrino fluxes. 36
3.9 Limits on DSNB flux. 37
3.10 Total emission versus energy for $\overline{\nu}_{\mathrm{e}}$ from pre-SN and from a SN burst 40
3.11 Comparison of L_{ν} number of, and $< E_{\nu} >$ mean energy of emitted $\overline{\nu}_{\mathrm{e}}$, against time to core collapse, in models. 41
3.12 Comparison of neutrino emission against time before and after the start of core collapse. 42
3.13 Comparison of total number of IBDs in a 12 hour window against time to core collapse, and against energy at the final time step, predicted in models. 44
3.14 $\overline{\nu}_{\mathrm{e}}$ emission and average $\overline{\nu}_{\mathrm{e}}$ energy from pair production (the dominant thermal process) and beta processes (β^{-} decay, e^{+} capture) in the model of Patton et al. 45
3.15 Proportion of $\overline{\nu}_{\mathrm{e}}$ emission above 5 MeV $\overline{\nu}_{\mathrm{e}}$ energy originating from beta processes in the model of Patton et al. 46

4.1 Scale diagram of the SK detector 52
4.2 Photograph of the SK inner detector taken during 2018 tank open work. 53
4.3 SK coordinate system. 54
4.4 Schematic of the SK water system. 58

4.5 Water transparency and gadolinium sulfate loading against time in EGADS. 59
4.6 Schematic of the EGADS water system, on which the SK-Gd water system is based. 60
4.7 Vertex resolution for electrons in SK. 70
4.8 Angular resolution for electrons in SK 73
4.9 Energy resolution used in SK-III solar neutrino study. Black points show one standard deviation for electron MC. **Red** shows a polynomial fit to those points. Black line shows the equivalent used for SK-I. Reproduced from [2]. 74
4.10 Distribution of β_1 and reconstructed energy for neutron captures on Gd and background sample. 76

5.1 Proportion of TNC which are on gadolinium against the proportion of gadolinium by mass dissolved in water. 81
5.2 Decay chain of Uranium-238. 83
5.3 Decay chain of Thorium-232. 84
5.4 Decay chain of Actinium-227/Uranium-235. 85
5.5 Schematic of the UDEAL system for automatic water transparency measurements. 88
5.6 Extract from technical drawings of EGADS. 91
5.7 Photograph of PMTs being mounted in EGADS. 92
5.8 Schematic diagram of a single beam spectrophotometer 95

5.9 Drift-corrected UV-absorption spectra of gadolinium sulfate solution at varied dilution. The strength of the absorption increases with concentration. 95
5.10 UV absorption of gadolinium sulfate against dilution. 96
5.11 The results of simple MC assuming accounting only for Compton scattering and assuming equipartition of energy between γ-rays, compared with a full MC treatment in SKDETSIM with the GLG4SIM γ-ray emission model. 98
5.12 TNC on Gd energy spectrum observed in SK with Gd loaded neutron source vessel by Watanabe et al. 100
5.13 Multiplicity of γ-rays in emission models. 102
5.14 Emission energies in γ-ray emission models. 103
5.15 Comparison in some reconstruction and isotropy variables between TNC on Gd γ-ray emission models. 104
5.16 Delayed event time distribution for an AmBe run in Gd-loaded EGADS. 106

6.1 WIT efficiency against electron true total energy, evaluated with simulation. 110
6.2 Distribution of neutron capture times from products of spallation. 116
6.3 Distribution of true β energies (above Cherenkov threshold) of spallation daughters that decay by βn. 116

6.4 Reactor and geo $\overline{\nu}_e$ flux under 2010 and 2017 reactor activity assumptions. Differences in shape are created by different oscillation baselines contributed by different reactors. 119
6.5 Distribution of online selected hits *n18* for events passing the WIT. 121
6.6 Distribution of reconstructed squared radial position for events passing the WIT and volume and n18 cuts. 122
6.7 Distribution of reconstructed vertical position for events passing the WIT and volume and n18 cuts. 123
6.8 Effect of n18 and effwall preselection on n18 distributions of Gd MC and background data. 124
6.9 Effect of n18 and effwall preselection on effwall distributions of Gd MC and background data. 125
6.10 The mean and RMS of dR of simulated DC events decrease with increasing prompt event energy, due to improving vertex resolution, calculated by the detector simulation. 126
6.11 Distribution of coincidence distance and coincidence time for simulated low energy DC IBD events and accidental background. 129

7.1 ROC curves of some example classifiers. The integral of the curve is one way to quantify performance. 136
7.2 Different methods of calculating the effectiveness of classifiers are closely related. 138
7.3 Performance comparison of BDTs with fixed hyperparameters as number of training events is increased. 140

7.4 ROC integral difference between training and test samples, against number of background and signal MC training events. 141
7.5 Performance comparison of BDTs, with varied feature variable inclusion and hyperparameters. 143
7.6 Performance comparison of BDTs, with feature variable changed in order of importance ranking. 145
7.7 Best performing BDTs from this study compared to that used in Simpson et al. There is marginal improvement. 145
7.8 Variables (1-7) selected for inclusion in BDT. 148
7.9 Variables (8-13) selected for inclusion in BDT. 149
7.10 Correlation matrices for signal and background samples. . . . 150
7.11 BDT scores evaluated on large datasets. 153
7.12 Background rejection factor against signal efficiency for final BDT and an LD using the same variables. Evaluated on a test sample independent of the training sample. 154
7.13 Variation in BDT response in background data sample. . . . 155

8.1 Distribution of DC channel variables in final selection for signal and largest backgrounds. 161
8.2 Distribution of single neutron channel variables in final selection for signal and largest background. 162
8.3 Trigger and selection efficiency for DC events against prompt positron true total energy. 163
8.4 Maximum range of detection against signal window size, for different FPR and background case. 165

8.5 Expected maximum range of detection in the final 12 hours before collapse, for 15 $M_\odot$ and 25 $M_\odot$ stars. 168
8.6 Expected early warning against range of detection, for 15 $M_\odot$ and 25 $M_\odot$ stars. 169
8.7 Expected signal events in 12 hour time window, after detection efficiencies are taken into account. 171
8.8 As Figure 8.5, but with reference numbers for KamLAND included. 172
8.9 As Figure 8.6, but for the low (0.02%) gadolinium loading case. 176
8.10 Residuals of data compared to prediction divided by the expected standard deviation. 179
8.11 Effect of background window size on bias and accuracy of the event rate predictions. 180
8.12 Gaussian one-sided likelihood of D_i assuming a Gaussian distribution, including period of deliberate convection, plotted against date. 181
8.13 Histogram of Gaussian one-sided likelihood of D_i. Before and during a period of deliberate convection. 182
8.14 Cross sectional dimensions of a Hyper-Kamiokande water tank. 183
8.15 Schematic cross section of JUNO 184
8.16 Expected maximum range of detection of pre-SN $\overline{\nu}_e$ for Hyper-K and JUNO, for 15 $M_\odot$ and 25 $M_\odot$ stars. 185

List of Tables

4.1 SK-IV Trigger Scheme. 65

5.1 Target activity levels in mBq per kg of gadolinium sulfate from various isotopes. Typical values are given for gadolinium sulfate purchased 'off the shelf'. 86

5.2 Abundance, decay energy and TNC cross sections of Gd isotopes and H. 97

5.3 Comparison in some reconstruction and isotropy variables between TNC on Gd γ-ray emission models. 104

7.1 Variables selected for inclusion in BDT, based on BDT importance scores. 146

7.2 Variables selected for inclusion in BDT, based on trial $\frac{S}{\sqrt{B}}$ impact. 147

8.1 Anti-electron neutrino flux multiplied by IBD cross section for models considered. 165

8.2 Maximum range of detection under various assumptions. . . . 170

8.3 Expected numbers of events at 200 kpc in the final 12 hours before collapse at SK-Gd. Uncertainty comes from TNC γ-ray model only. 171

8.4 Time at which expected signal exceeds threshold, for some assumptions chosen to represent Betelgeuse. 173

8.5 As Table 8.4, but for the low (0.02%) gadolinium loading case. 175

8.6 As Table 8.2, but for the low (0.02%) gadolinium loading case. 177

8.7 Simplified range calculations for combined signal of multiple detectors. 186

A.1 List of nearby red supergiant candidates, with distance estimates when available. 197

Glossary

$M_\odot$ solar masses

α **Ori** Betelgeuse

Ac actinium

AdaBoost adaptive boost

AmBe americium-beryllium

BDT boosted decision tree

C carbon

CC charged current

CCSN core-collapse supernova

DAQ data acquisition

DC delayed coincidence

DSNB diffuse supernova neutrino background

EGADS Evaluating Gadolinium's Action on Detector Systems

Fe iron

FPR false positive rate

FRP fibre reinforced plastic

FV fiducial volume

H hydrogen

HK Hyper-Kamiokande

HPGe hyper-pure germanium

IBD inverse beta decay

ID inner detector

JUNO Jiangmen Underground Neutrino Observatory

LD Fisher's linear discriminant

LMC Large Magellanic Cloud

MO mass ordering

MSW Mikheyev-Smirnov-Wolfenstein

N nitrogen

NC neutral current

Ne neon

NSE nuclear statistical equilibrium

O oxygen

OD outer detector

PE photoelectron

PMT photomultiplier tube

pre-SN pre-supernova

QE total efficiency of a PMT, quantum efficiency × collection efficiency

RSG red supergiant

SF spontaneous fission

Si silicon

SK Super-Kamiokande

SM Standard Model of Particle Physics

SN supernova

SNe supernovae

SRN supernova relic flux

Th thorium

TNC thermal neutron capture

U uranium

WC water-Cherenkov

WIT wideband intelligent trigger

ZAMS zero age main sequence

Chapter 1

Introduction

The topic of this thesis is the potential detection of a transient low energy electron anti-neutrino flux in the hours prior to a core-collapse supernova using the gadolinium-loaded Super-Kamiokande (SK) detector (SK-Gd). These pre-supernova neutrinos are mainly from thermal emission in the final stage of stellar fusion, and would be detected in an energy range below the usual thresholds of SK. They have never before been detected.

Detection of pre-supernova neutrinos would allow early warning of a nearby core-collapse supernova, in advance of the beginning of core collapse. Previous estimates of SK-Gd's ability to detect pre-supernova neutrinos have a very wide range (addressed in section 8.2); ranging from one prediction that not even a very nearby star ($\sim 200\ pc$), such as Antares or Betelgeuse, could be detected with confidence approaching core collapse, and another predicting that sensitivity could extend as far as 2 kpc.

Firstly, in chapter 2 a theoretical introduction is given on the topic of neutrinos in general. Then, in chapter 3, necessary background information

is given concerning stellar evolution and supernovae, and models of pre-supernova neutrino emission are discussed.

SK is a long-running neutrino detection experiment. At the time of writing, preparations are being made to add gadolinium sulfate to the pure water of the detector. This reduces backgrounds for certain types of neutrino event, and so enables the detection of pre-supernova neutrinos. A description of the SK detector is given in chapter 4. Discussion of the purpose, effects, and practical requirements of gadolinium loading is made in chapter 5.

In order to estimate the sensitivity of the Gd loaded SK detector to pre-supernova neutrinos, a model of signal response and background was produced for low energy neutrino events below the usual thresholds of SK. This is described in chapter 6. A multivariate analysis with boosted decision trees was used to identify neutron captures on gadolinium, and so reduce background to the challenging low energy flux, described in chapter 7. In chapter 8, based on this response model, the abilities of SK with gadolinium to detect neutrinos from a pre-supernova star are assessed in terms of distance to the star and time before core collapse. Conclusions are drawn in chapter 9.

Based on the work described in this thesis, a peer-reviewed article has been published in Astrophys. J. [3]. The text, figures and table of the article overlap with this thesis. Both the article and this thesis are the author's original work.

Chapter 2

Neutrinos

Neutrinos are spin-$\frac{1}{2}$ fermions that interact by the weak nuclear and gravitational forces. Neutrinos have the same three generational flavour structure as the charged leptons in the Standard Model of Particle Physics (SM). They have a small (sub eV) but non-zero mass, and oscillations between the flavours can occur as they propagate. The SM does not contain neutrino masses.

Among other theoretical issues with the SM, explanations of gravity and dark matter are not included, and the use of renormalisation in the construction of the theory implies that it is an effective theory, and that there is an energy scale at which new physics exists.

In section 2.1, a brief survey of the state of neutrino theory and experiment is given. Some relevant neutrino interactions are described in section 2.2. Despite its wider importance, neutrino mixing does not feature heavily in this thesis; a very brief explanation of the theory of three neutrino mixing and the effect of matter on neutrino mixing is given in section 2.3

and section 2.4 respectively.

2.1 The State of the Art

Originally proposed by Pauli in order to explain the three-body spectrum and spin statistics of β-decay [4], it was thought that neutrinos might never be directly observed [5]. Fermi's theory of β-decay was a precursor to modern weak interaction theory [6, 7], and directly coupled the neutron to the electron, neutrino, and proton. Modern electroweak theory was developed later by Glashow, Salam, Weinberg and others, introducing W and Z bosons as mediators and unifying the electromagnetic and weak nuclear forces [8, 9, 10]. Reines and Cowan first observed neutrinos from a nuclear reactor, using a heterogeneous detector made from a large quantity of cadmium chloride loaded water surrounded by liquid scintillator and monitored by photomultiplier tubes (PMTs), in the mid-1950s [11].

Much has been learned about particle physics in general, and neutrinos specifically, since the Reines-Cowan experiment. The SM has been developed in this time, which explains the behaviour of the strong and weak nuclear forces, and electromagnetism, in a unified framework. As well as those from nuclear reactors, neutrinos have been detected from the Sun, from cosmic rays, from extragalactic origins, from radioactive decays in the Earth's crust, and from artificial sources including focussed beams of neutrinos (see review [12, Sec. 14]).

Meanwhile, the SM has passed a multitude of precise experimental tests, but faces some contradictions and problems that indicate there is a more

complete theory yet to be discovered. That neutrinos have mass and are mixed is a clear experimental deviation from the SM.

The 2015 Nobel prize in physics was jointly awarded for two experiments, to Takaaki Kajita for SK and Arthur McDonald for the Sudbury Neutrino Observatory (SNO), which respectively proved that neutrinos have mass and that they change flavour [13, 14]. In SK an up-down asymmetry in atmospheric muon neutrino detection was observed. This is due to upgoing atmospheric neutrinos having travelled a larger distance, having come from the atmosphere on the other side of the Earth [15] (L is changed in Equation 2.8, see section 2.3). In the case of SNO, neutrinos from the Sun were detected in different interaction channels that allowed the flux of electron neutrinos and all neutrino flavours to be measured independently, showing that the total solar neutrino flux was as predicted by solar modelling, while the electron neutrino flux was reduced [16] (caused by the Mikheyev-Smirnov-Wolfenstein (MSW) effect, see section 2.4).

At the time of writing there are many neutrino detectors in operation with various aims. These include the precise measurement of the neutrino oscillation parameters (see section 2.3), the neutrino mass ordering (MO), the Dirac or Majorana nature of neutrino masses (e.g. neutrinoless double beta decay experiments), the existence and amount of CP violation in the lepton sector, and the absolute mass of the neutrinos (e.g. tritium decay experiments). There are also experiments trying to resolve apparent anomalies that appear (or appeared) to not fit into the three neutrino mixing model (for more information see review [12, Sec. 14])

More directly relevant to the research described in this thesis are those

experiments capable of observing neutrinos from a core-collapse supernova (CCSN). In 1987, neutrinos were observed from a CCSN in the Large Magellanic Cloud (LMC) by several experiments [17, 18, 19]. More can be read about supernovae (SNe) and their neutrino emissions in chapter 3.

2.2 Neutrino Interactions

Inverse beta decay (IBD) is the interaction $\overline{\nu}_e(A_z, A_{z-1})e^+$, and its cross section is closely related to that of beta decay. In this thesis we are mainly concerned with IBD on hydrogen, as for electron anti-neutrinos at < 10 MeV and a water target, this is the interaction with the largest cross section. Taking into account detection threshold and energy resolution effects for a water Cherenkov detector, Figure 2.1 shows how other processes compare in magnitude depending upon the energy. Below 10 MeV, the IBD cross section is clearly dominant, and grows rapidly with energy. The benefit of neutron capture on detection efficiency will be discussed in chapter 5. In this thesis, IBD will always refer to IBD on hydrogen.

Neglecting the small effect of nuclear recoil, the total energy E_e of a positron produced by IBD is related to the electron anti-neutrino energy E_ν by $E_e = E_\nu - \Delta$, where $\Delta = m_n - m_p = 1.293$ MeV is the nucleon mass difference. The threshold is then the neutrino energy in the limit of positron kinetic energy going to 0, i.e. $E^{IBD}_{thresh} = \Delta + m_e = 1.80\ MeV$. For the studies in this thesis, an accurate approximation of the energy dependent cross section is used [1, Eqn. 25], shown in Figure 2.2. At low energies, the direction of the incoming neutrino cannot be determined from the direction

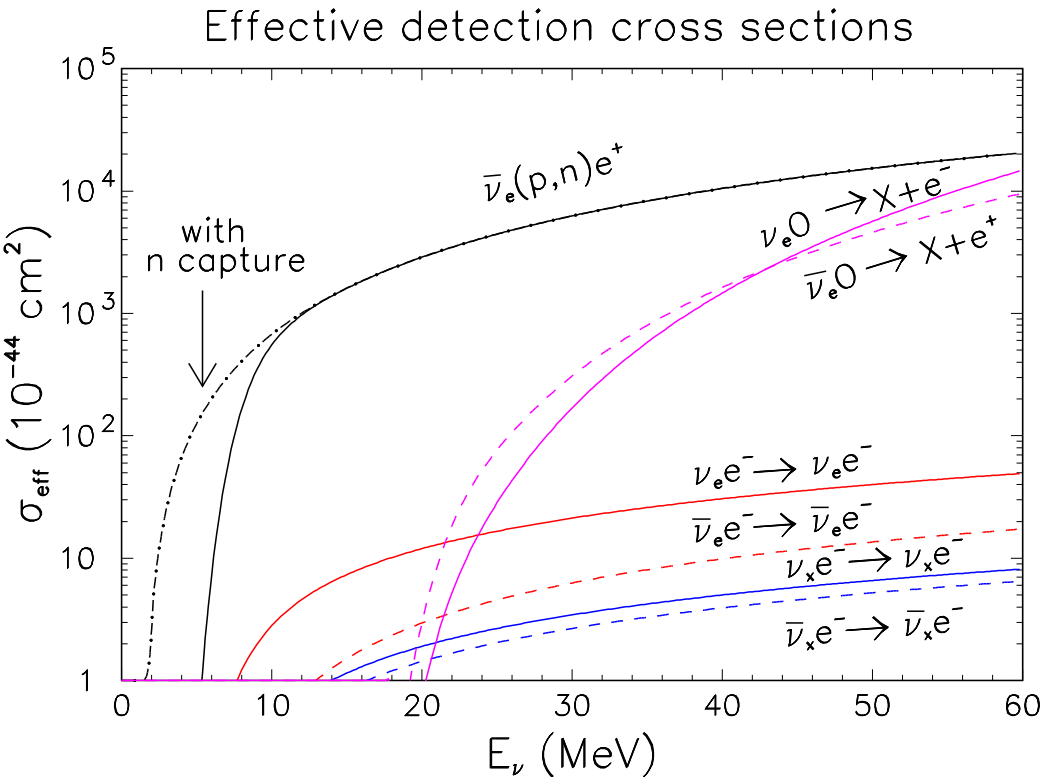


Figure 2.1: Effective neutrino cross sections taking into account threshold and resolution effects for a water Cherenkov detector, reproduced from [20]

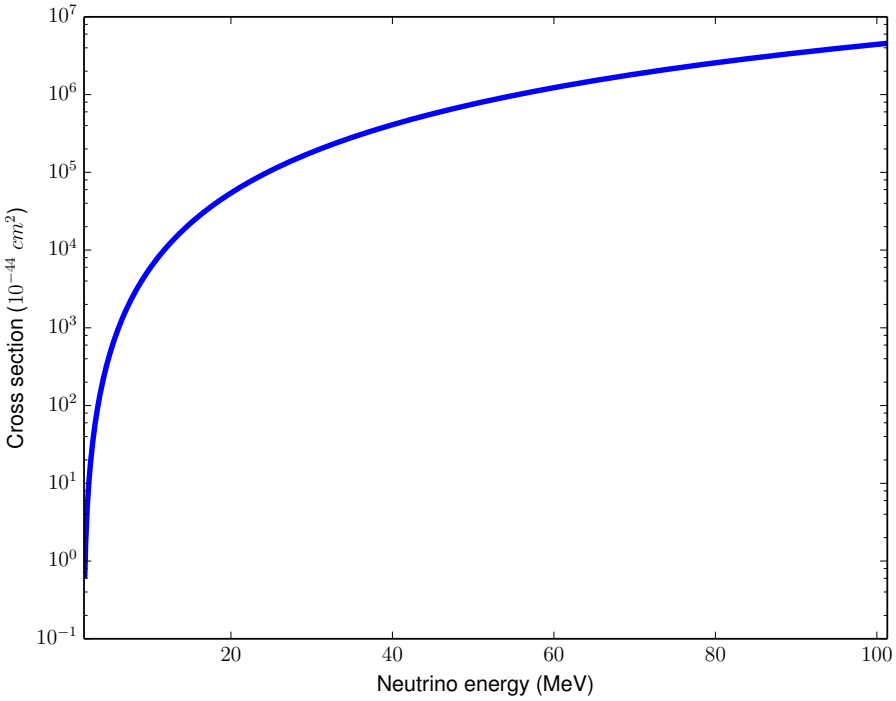


Figure 2.2: IBD cross section against neutrino energy using accurate approximation from [1].

of the IBD positron. The distribution of the positron direction of travel relative to the neutrino only becomes strongly forward peaked at well over 100 MeV [21].

2.3 Three Neutrinos

In the SM, there is a neutrino associated with each charged lepton (electron, muon, and tauon). Neutrino interactions conserve lepton number in the same way as charged leptons.

Measurements of the invisible width of the Z resonance at LEP strongly constrain the number of light neutrinos to 2.984±0.008 [22]. For further light neutrinos to exist, they must not couple to the electroweak force.

The mass eigenstates of neutrinos are not flavour eigenstates, which produces flavour oscillations as the neutrinos propagate. This is analogous to the evolution of a coupled pendulum, or indeed the mixing present in the quark sector described by Cabibbo, Kobayashi and Maskawa [23, 24].

With the flavour components represented by a vector, there is a transformation from the flavour basis to the mass basis denoted by the Pontecorvo Maki Nakagawa Sakata (PMNS) matrix

$$U = \begin{pmatrix} U_{e1} & U_{e2} & U_{e3} \\ U_{\mu 1} & U_{\mu 2} & U_{\mu 3} \\ U_{\tau 1} & U_{\tau 2} & U_{\tau 3} \end{pmatrix}, \tag{2.1}$$

where $U_{\alpha i}$ relates a flavour state α to a mass state i. Without CP violation, this transformation is equivalent to a rotation in a three dimensional space, so

can be described by the usual Eulerian three dimensional rotation matrices. It is from this analogy to rotation matrices that we get the idea of mixing angles. CP violation modifies this slightly by adding the Dirac phase factor $e^{-i\delta}$. If neutrinos are Majorana particles two further phase factors, $e^{i\alpha_1/2}$ and $e^{i\alpha_2/2}$, are required.

$$U = \begin{pmatrix} 1 & 0 & 0 \\ 0 & c_{23} & s_{23} \\ 0 & -s_{23} & c_{23} \end{pmatrix} \begin{pmatrix} c_{13} & 0 & s_{13}e^{-i\delta} \\ 0 & 1 & 0 \\ -s_{13}e^{-i\delta} & 0 & c_{13} \end{pmatrix} \times \begin{pmatrix} c_{12} & s_{12} & 0 \\ -s_{12} & c_{12} & 0 \\ 0 & 0 & 1 \end{pmatrix} \begin{pmatrix} e^{i\alpha_1/2} & 0 & 0 \\ 0 & e^{i\alpha_2/2} & 0 \\ 0 & 0 & 1 \end{pmatrix}, \tag{2.2}$$

where s and c denote the sine and cosine of the mixing angles respectively. When this is expanded, it becomes clear that all oscillations will include at least two of the mixing angles and the CP phase factor, although some terms will have a small magnitude.

$$U = \begin{pmatrix} c_{12}c_{13} & s_{12}c_{13} & s_{13}e^{-i\delta} \\ -s_{12}c_{23} & c_{12}c_{23} - s_{12}s_{23}s_{13}e^{i\delta} & s_{23}c_{13} \\ s_{12}s_{23} - c12c_{23}s_{13}e^{i\delta} & -c_{12}s_{23} - s_{12}c_{23}s13e^{i\delta} & c_{23}c_{13} \end{pmatrix} \times \begin{pmatrix} e^{i\alpha_1/2} & 0 & 0 \\ 0 & e^{i\alpha_2/2} & 0 \\ 0 & 0 & 1 \end{pmatrix} \tag{2.3}$$

In the context of oscillations, the Majorana phase factors cancel and have no effect; this means that oscillation experiments cannot identify if neutrinos are Majorana.

Mass eigenstates will propagate in vaccum according to plane wave solutions

$$|\nu_i(X)\rangle = e^{-iP.X} |\nu_i(0)\rangle , \tag{2.4}$$

where X is the four-vector displacement, P the four momentum.

Detectable neutrinos will generally be ultrarelativistic, as they have MeV scale energy and sub-eV scale mass. Therefore,

$$P.X \approx \frac{m_i^2 L}{2E} \tag{2.5}$$

where L is the spatial displacement, and we have assumed $t = L/c$; this expression is not Lorentz covariant, and neither is the usual treatment of neutrino oscillations. However, the effect of ignoring Lorentz covariance in this way is small enough to ignore on all but the largest scales.

It follows that the probability of observing flavour state β from a neutrino that was produced in a flavour state α is

$$P_{\alpha\to\beta} = |\langle\nu_\beta(L)|\nu_\alpha\rangle|^2 = |\sum_i U^*_{\alpha i} U_{\beta i} e^{-i\frac{m_i^2 L}{2E}}|^2, \tag{2.6}$$

which can be rearranged to be in terms of the mass differences, L and E.

Sometimes a two flavour mixing model is sufficient to broadly understand an experiment, although three flavour models should always be used in serious analysis. Two-flavour mixing works as a simple model because θ_{13} is

a small angle compared to the θ_{12} and θ_{23}; and the neutrino mass differences are very unequal ($|\Delta m^2_{21}| << |\Delta m^2_{32}|$), making the oscillation length scales vastly different. Detection of neutrinos is usually either in electron or muon flavour, depending on the experiment. For example, if the production and detection are both via the electron (or anti-electron) flavour, as is the case in reactor neutrino experiments, the transformed electron component will contain $c_{12}c_{13}$, but one could assume $c_{13} \approx 1$ to simplify consideration of the largest oscillation effects. CP violation is not possible in two flavour oscillations.

In the two flavour case,

$$P_{\alpha\to\beta} = \sin^2(2\theta)\sin^2(\Phi_{osc}), \tag{2.7}$$

for mixing angle θ and oscillation phase Φ_{osc}, provided $\alpha \neq \beta$. A convenient formulation of Φ_{osc} is

$$\Phi_{osc} = 1.27(\frac{GeV}{eV^2 km}) \times \Delta m^2(eV^2) \times \frac{L(km)}{E(GeV)} \tag{2.8}$$

This contains most of the 'big picture' information for a neutrino oscillation experiment, with

- mass splitting (Δm^2), which affects the oscillation length
- energy E, which affects the oscillation length
- baseline L, the distance over which the neutrinos propagate, which will determine at what point in the oscillation the neutrinos are measured.

The mixing angles then determine the amplitude of the oscillations.

Very simply, oscillation experiments have the transition probability as the dependent variable, with propagation length and energy as independent variables, in order to infer the mass differences and mixing angles.

Whether Δm^2_{32} is positive (normal ordered), or negative (inverted ordered), is undetermined at the time of writing, although experiment weakly favours the normal ordering[25].

2.4 The MSW Effect

The above plane wave solution (Equation 2.4) does not hold in the case of neutrinos propagating through matter, as coherent forward scattering affects the energy levels of the propagation eigenstates, giving effective mixing parameters. With a constant matter density along the path of propagation, the effect is to modify the oscillation length and depth. With a decreasing matter density, e.g. exiting the core of a star, it may be that maximal mixing occurs, leading to resonant conversion between neutrino flavours. The effect of matter on neutrino oscillations is named the Mikheyev-Smirnov-Wolfenstein (MSW) effect.

For simplicity, I will describe the minimum necessary details of the two flavour case following [26].

Neutral current scattering affects different flavours equally so will not have an effect. The charged current interaction (W boson mediated $\nu_e e^- \rightarrow \nu_e e^-$) gives an additional term in the propagation Hamiltonian for the electron

neutrino. This leads to an additional effective mass term

$$A = 2\sqrt{2}(G_F Y_e/m_n)\rho E, \tag{2.9}$$

where Y_e is the electron fraction of the matter, m_n the nucleon mass, ρ the density, and G_F is Fermi's constant.

With this additional term the effective mass splitting becomes

$$\sqrt{((\Delta m^2)\cos(2\theta) - A) + ((\Delta m^2)\sin(2\theta))^2}. \tag{2.10}$$

The mass splitting will have a minimum at $A = (\Delta m^2)\cos(2\theta)$ if $(\Delta m^2) > 0$. It is at this minimum in the mass splitting that resonant conversion occurs.

The density at which the resonance occurs is therefore

$$\rho = \frac{(\Delta m^2)\cos(2\theta)}{2E\sqrt{2}G_F}. \tag{2.11}$$

At densities much lower than this, oscillations will be vacuum-like, whereas well above this mixing will be maximal and oscillation will be suppressed.

In the specific case of the Sun, as the neutrinos are produced by nuclear fusion, all will be produced as pure ν_e. At sufficiently high matter density, the effective mass of the ν_e is higher than that of the ν_μ, which will be unchanged. But, exiting the Sun, density decreases slowly so that the effective ν_e mass crosses that of the ν_μ. Provided the oscillation length is small compared to the width of the resonance, i.e. the transition is adiabatic, then neutrinos above a critical energy will be converted into ν_μ. MSW effects become important at around 2 MeV for solar neutrinos. This picture is well supported by the

evidence from solar neutrino experiments.

The MSW resonance in the Sun depends on the mass difference Δm^2_{21}, called the low (L) resonance, and does not apply to anti-neutrinos. A high (H) resonance can also occur at a density determined by Δm^2_{32} (or Δm^2_{31} in the inverted neutrino MO), which does affect anti-neutrinos [27], and so is more directly relevant to the detection of pre-supernova (SN) $\overline{\nu}_{\rm e}$ at SK as discussed later in this thesis.

Chapter 3

Supernovae and Pre-supernovae

SNe are explosions of stars. The energy release is extremely large and rapid: a SN will often be as bright as its entire galaxy. SNe are divided into observational categories by the presence of certain optical spectral lines, and by their light curves. These spectral distinctions are caused by the envelope, which does not affect the neutrino signal. All standard SN spectral types are caused by core collapse except type-Ia, which is caused by thermal runaway. All SN discussed in this thesis are CCSN.

Many of the isotopes present in the universe, affecting the chemical evolution of stars and galaxies, and some necessary for life, are thought to be synthesised and distributed by SNe, especially oxygen (O), and isotopes from neon (Ne) to calcium [28].

Several SNe have been observed historically within our galaxy, and there have been many modern observations of SNe in distant galaxies. The best studied SN is 1987A, which occurred near our galaxy in the LMC, and was observed in neutrinos by multiple detectors and electromagnetically with

multiple modern instruments.

Due to their huge transient neutrino emission, SNe are a good target for neutrino astronomy. Astrophysical neutrinos with identified sources have only ever been detected from the Sun (for a review see [29]), from SN1987A [17, 18, 19], and blazar TXS 0506+056 [30]; but these exemplify the role of neutrino observations in multimessenger astronomy.

A CCSN produces a ∼10 second burst of neutrinos at tens of MeV, which is large enough that it can be detected by SK and other neutrino detectors [31] if it is in or near the Milky Way.

Models of SNe were dramatically confirmed by the detection of SN neutrinos from SN1987A. In the case of another SN in or near our galaxy, the current generation of neutrino detectors would be capable of collecting a much larger sample of SN neutrinos, improving our understanding and resolving outstanding questions about SNe. Neutrinos are produced earlier than electromagnetic radiation in a SN, so can generate a warning enabling astronomers to begin observation as early as possible. Alert systems already exist for this purpose, linking together many detectors for maximum effect [32]. SK, as a large water Cherenkov detector, has the currently unique ability of determining the direction of a SN from elastically scattered electrons, which is useful for guiding optical instruments [33, 31]; SN neutrino detection is a major goal for SK.

The only direct observation of SN neutrinos so far is SN1987A, and neutrino-cooled stars have never been observed, so detection would contribute to our understanding of late stage stellar evolution [34, 35, 36, 37]. The detection of a galactic SN has the potential to resolve the neutrino MO [38, 39, 40],

and open a window on collective neutrino oscillations [41, 42].

Before core collapse occurs, neutrino emission increases over a relatively short time-scale, to what could be detectable levels for a nearby star [43], which could give advanced warning of a nearby SN. This earlier alert to the astronomy community could aid in observing the early light from a SN. Advance warning could prevent SK (and other SN neutrino detectors) from missing a nearby CCSN due to planned down-time. SK has run for over 20 years so far, and has on average $> 90\%$ up-time, making it especially useful for the detection of SNe, which are rare and could happen at any time. KamLAND, another neutrino detection experiment, has a functioning pre-SN alert system [44]. SNe within the Milky Way are expected 2-3 times per century [45, 46].

The focus of this thesis is the possiblity of the detection of pre-supernova (pre-SN) neutrinos at SK-Gd. In order to motivate and give background, a schematic description of stellar evolution is given in section 3.1, and of the CCSN mechanism in section 3.2, focussed on the neutrino signal, with specific discussion of what was learned from SN1987A in section 3.3. Many currently operating and proposed experiments would be capable of detecting a SN at some range, so a brief survey of detection methods is given in section 3.4. The detection of the diffuse supernova neutrino background (DSNB) flux provides the motivation for SK-Gd, and so is covered in section 3.5. The predictions of the neutrino flux used in the original studies in this thesis are described in section 3.6.

The background material relies heavily on the reviews by Woosley, Heger, and Weaver *The evolution and explosion of massive stars* [28]; Arnett, Bah-

call, and Kirschner *Supernova 1987A* [47]; and Giunti and Kim's book *Fundamentals of Neutrino Physics and Astrophysics* [48].

3.1 Stellar Evolution

The composition of a star evolves in time. The determinants in this evolution are (very broadly): heating, cooling, pressure, and gravity. Heating can be caused by the fusion of light nuclei into heavier ones, but also by gravitational contraction. Cooling is caused by the emission of radiation, including of neutrinos and photons. Pressure includes the classical thermodynamic kind, but also electron degeneracy when densities become high enough. Fusion occurs mainly in the core of the star where the temperatures and densities are highest.

Assuming Newtonian gravity, and that the star is comprised of ideal gas, evolution in core temperature (T_c) and core density (ρ_c) will follow a trajectory depending on the mass M and composition

$$\frac{T_c^3}{\rho_c} \propto M^2 \mu^3, \tag{3.1}$$

where $\mu = (\sum_i Y_i + Y_e)^{-1}$ depends on the fraction Y of electrons e and other species i [28]. The tendency is for the stellar core to become denser and hotter through its life, as nuclear fuel is used up. Furthermore, higher mass stars will, in general, have higher temperatures and densities. In detailed stellar models, there are deviations from this simple equilibrium schematic of evolution when new sources of heating or cooling become available, as can

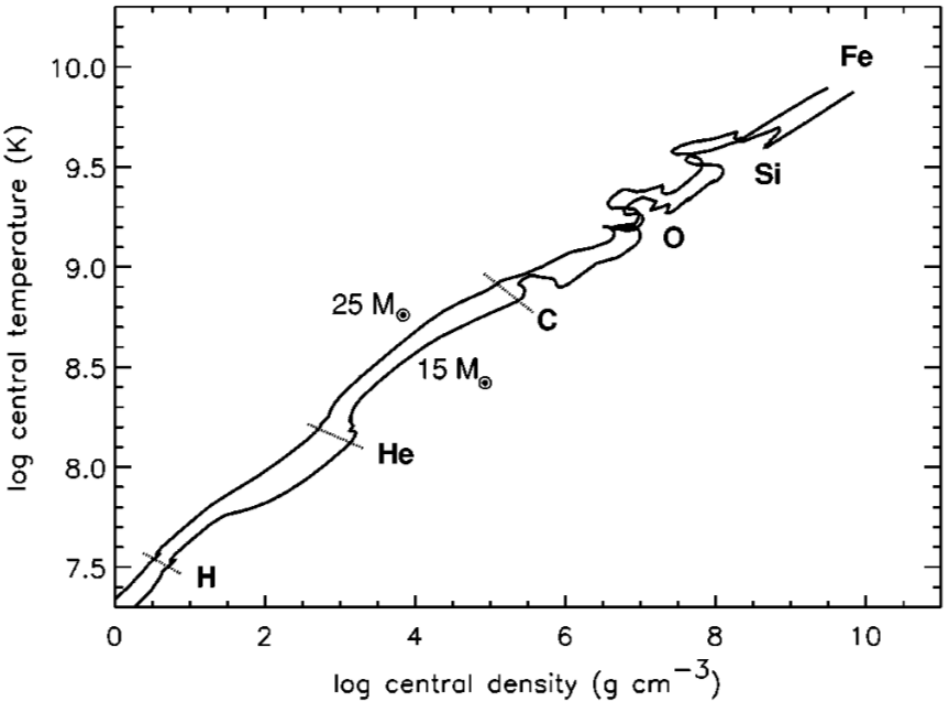


Figure 3.1: The evolutionary paths of stellar models with two different initial masses are plotted in core temperature and density. The tendency is for the core temperature and density to gradually increase. Labels show the point at which different burning processes are active. Reproduced directly from Woosely, Heger, and Weaver [28]

be seen in Figure 3.1. An increase in the rate of cooling, or decrease in the rate of heating, will cause the core of the star to increase in density and, perhaps counter-intuitively, in temperature [28].

Mainly due to the increasing Coulomb barrier with increasing atomic number, nuclear reactions have different temperature dependencies (see Figure 3.2). This leads to stars of different initial masses having different core isotopic composition, depending mainly on their thermal evolution, and therefore their initial mass. In a lower mass star (zero age main sequence (ZAMS)[1] mass <8 solar masses ($M_\odot$)), the core temperature can reach high enough ($\sim 10^8$ K) to fuse helium into carbon (C) and O by the triple-α process. C and O will accumulate in the core, but higher temperatures ($\sim 10^9$ K) are required to fuse them into even heavier isotopes. Electron degeneracy pressure will eventually be sufficient to prevent further gravitational heating, and so no new source of fusion energy will be accessible, with the star ending up as a white dwarf [28].

For ZAMS mass >8 $M_\odot$, C, nitrogen (N), Ne, and silicon (Si) can all be burned. This is because sufficiently high temperatures are reached before density limits due to electron degeneracy kick in. The rate of energy generation due to fusion, and energy loss rates due to thermal emission of neutrinos, are highly temperature dependent, as shown in Figure 3.2. Above $\sim 5 \times 10^8$ K, pair production of neutrinos will be the dominant form of cooling. The new (quasi) equilibrium will then mainly be determined by the balance of nuclear fusion against neutrino emission, i.e the points at which the neutrino cooling and fusion heating lines intersect in Figure 3.2. Thermal

[1] i.e. at the start of hydrogen burning

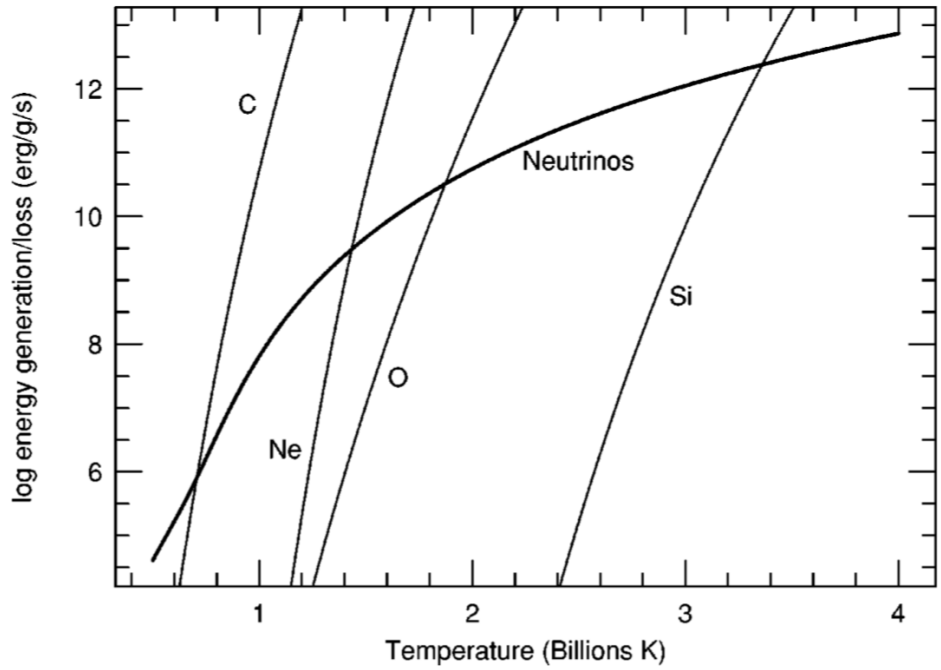


Figure 3.2: Temperature dependence of energy generation by fusion and energy loss by neutrino emission. Reproduced directly from Woosley, Heger, and Weaver [28].

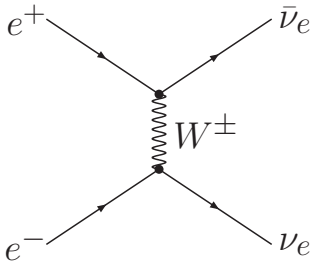
processes leading to neutrino emission are pair production, plasmon decay, and neutrino brehmsstrahlung, illustrated in Figure 3.3 [34]. The rapidly increasing cooling rate with temperature, due to neutrino emission, leads to further contraction and heating, and the fusion of even heavier nuclei.

As a result of Si burning, iron (Fe), which does not undergo further fusion, accumulates in the stellar core. The presence of the heavy species increases the density of the core, leading to the core to exceed the Chandrasekhar limit and collapse [48].

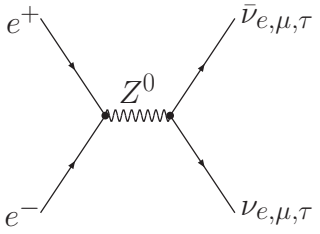
As the dominant cooling mechanism is neutrino emission, these stars are sometimes referred to as neutrino cooled stars. These massive Si burning stars can result in CCSNe, and so are also referred to as pre-SN stars.

The neutrino-cooled stage of a massive star's life is remarkably short compared to usual astrophysical timescales, with the C burning stage lasting hundreds of years, Ne and O stages lasting under a year, and Si burning lasting days or weeks [49, 28]. While these processes occur in the interior of the star, it may be that nothing changes in the star's electromagnetic emissions or at the outer surface of the star, as the thermal timescales of the star's envelope is so much larger than the timescale of core evolution, so such a state would not be observed by electromagnetic astronomy [34]. In the 100 years for which SN1987A's progenitor was observed, no obvious disturbance or variation was identified [47]. Figure 3.4 compares the progressively shorter and hotter burning stages of late stellar evolution.

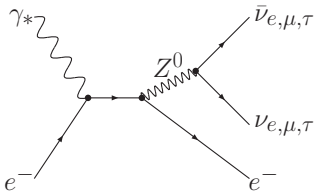
Stars at the lighter end of the CCSN mass range might not enter the Si burning stage, instead undergoing CCSN with an O-Ne-Mg core [34, 35], with Fe formed during the collapse by electron capture. Stars above 25 $M_{\odot}$



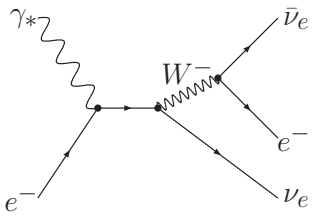
Pair production via W boson



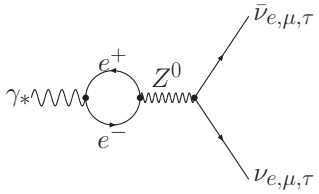
Pair production via Z boson



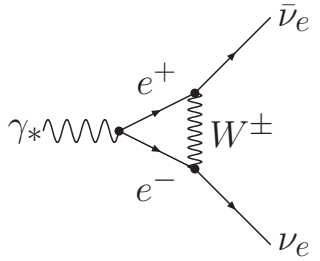
Photoproduction via Z boson



Photoproduction via W boson



Plasmon decay via Z boson



Plasmon decay via W boson

Figure 3.3: Feynman diagrams of some processes leading to thermal neutrino emission. Reproduced from Odrzywolek et al. [34].

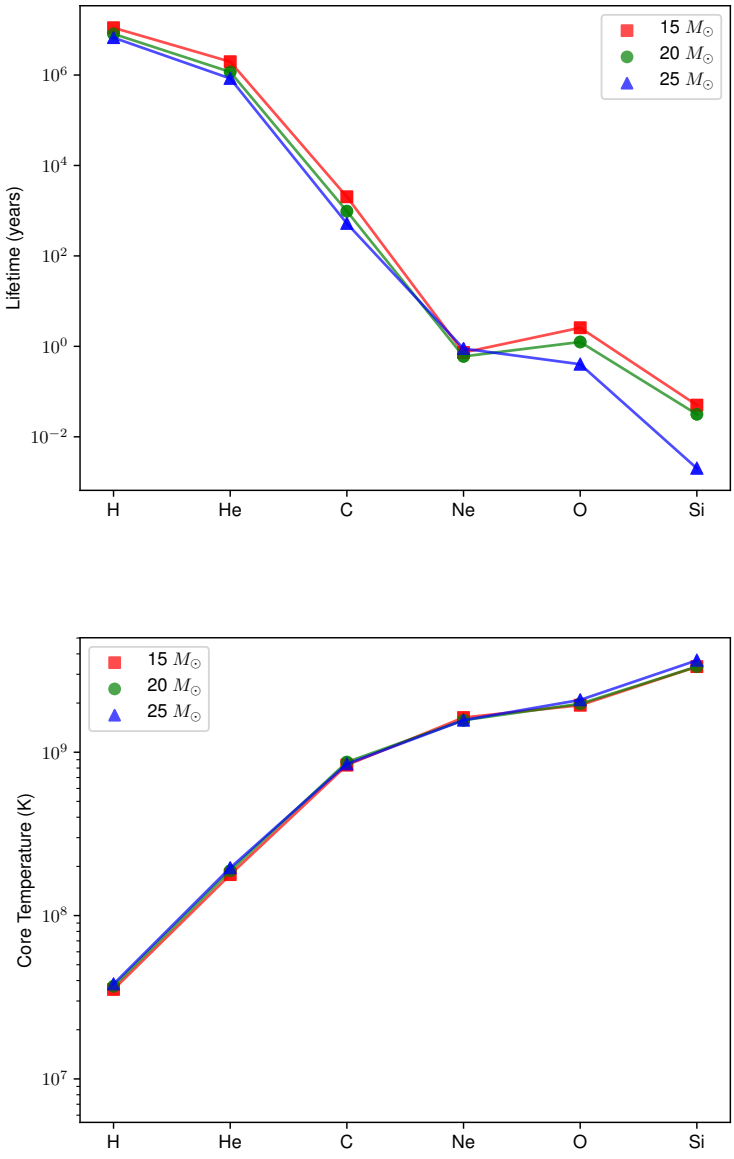


Figure 3.4: Characteristics of stellar burning for example stars, information taken from [28, Table I]. Successive burning generally stages have shorter lifetimes and have higher core temperatures. Core density follows as similar pattern to temperature, see Equation 3.1. Higher mass stars have shorter O and Si burning stages.

are thought to collapse first to a proto-neutron star, before collapsing to a black hole by fallback. Very massive stars >30 $M_\odot$ may collapse directly to a black holes as *failed* SNe, but could still produce an increasing and detectable neutrino flux in late stages prior to collapse [50]. Aside from ZAMS mass, stellar evolution also depends on metallicity and rotation; the models of pre-SN neutrino emission considered in this thesis assume solar metallicity and no rotation effects. Rotation increases the size of the helium core through increased mixing [28], and affects the final fate of the star. Metallicity affects mass loss during stellar evolution, so changes the core mass, and therefore whether a black hole or a neutron star is formed [28, 48]

3.2 Supernova Explosion Mechanism

Prior to collapse, the core, containing a large fraction of Fe, is surrounded by concentric shells of progressively lighter species, as illustrated in Figure 3.5. The core has mass O(1 $M_\odot$), with a density of $\sim 10^{10}$ g cm^{-3}, temperature $\sim$1 MeV. No fusion can occur in the core, which is supported by electron degeneracy pressure, although fusion will still be occurring in the shells [48].

The stability condition of a core supported by electron degeneracy is given by the Chandrasekhar mass

$$M < M_c \approx 5.83 M_\odot Y_e^2. \tag{3.2}$$

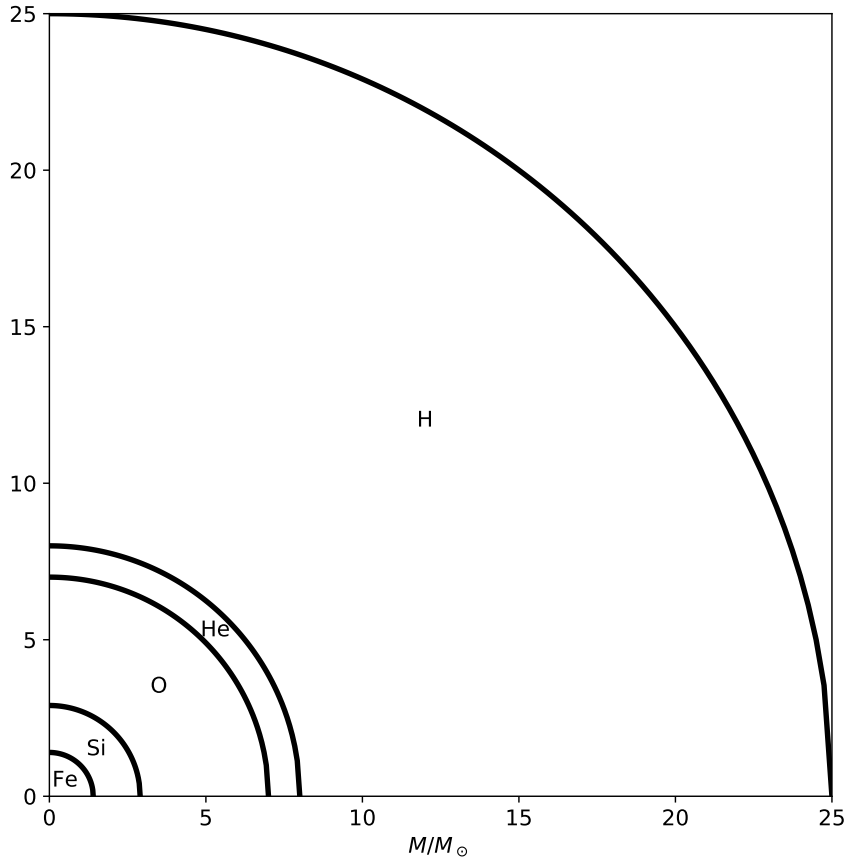


Figure 3.5: A pre-SN star contains concentric shells of species with decreasing mass number. The iron rich core is O(1 $M_\odot$), and the majority of the star's mass is in the hydrogen envelope. Reproduced from [51].

Due to the high temperature and density, photodissociation of Fe

$$\gamma + {}^{56}Fe \rightarrow 13\alpha + 4n \; - \; 124.4 \; MeV, \tag{3.3}$$

electron capture on nuclei and free protons all occur, cooling the core further and reducing the electron fraction. These processes also increase in rate with temperature and density, creating positive feedback. At this stage, the core has begun to collapse. All through collapse, neutrinos of all flavours are produced thermally [48].

The capture phase lasts less than 10 ms, and has very high neutrino instantaneous luminosity from the electron captures in the core. It is cut short as the matter density becomes large enough ($\sim 3 \times 10^{11} \; g \; cm^{-3}$) to be opaque to neutrinos. The inner core therefore collapses with constant lepton number at sub-sonic speed, that is, the collapsing matter is travelling more slowly than waves propagate through the matter. The outer core will however be in free-fall, and so collapse at super-sonic speed [48].

The inner core reaches the density at which nucleon degeneracy pressure will support it after ∼1 s, stopping its collapse abruptly and finding a new equilibrium. The outer core bounces off the hard inner core, creating a shockwave which then propagates outwards. The matter behind this outward shockwave can then accrete slowly to the inner core, now a proto-neutron star. The shockwave disassociates nuclei in the outer core, leading to a high rate of electron capture on free protons, creating a large neutrino flux, which is still trapped behind the shockwave due to its density [48].

Energy is dissipated by photodisintegration and neutrino emission, so

that the shock can stall, delaying the explosion by O(0.5 s). Some numerical SN models therefore fail to explode, or rely on some artificial restart of the shock. Detailed handling of neutrino transport, acoustics waves from the accretion of matter to the proto neutron star, and convection are thought to be important to create the heating to restart the shock. Convection could not be properly incorporated into models with assumed spherical symmetry, making multidimensional SN explosion modelling a hot topic for some years. The delayed explosion leads to a short plateau in thermal neutrino emission called the hump [48].

When the shockwave reaches a sufficiently low density to allow neutrinos to escape, the neutronization burst is produced, lasting a few milliseconds. In fact it is only the outer core which is neutronized, the inner core still has constant lepton number due to being opaque to neutrinos.

The core has a temperature of around 40 MeV at this stage [48], but the neutrino spectrum is much cooler. The maximum density which is transparent is different for each flavour (and anti-flavour), due to differences in interactions with the matter. Electron neutrinos and electron anti-neutrinos are emitted at lower temperatures and densities than other flavours, as the presence of electrons modifies the eigenstates of these flavours through forward scattering. Therefore, neutrinos of different flavours are emitted at different radii called neutrinospheres, with different temperatures. Around 3×10^{53} erg of gravitational energy is released, 99% of which goes to neutrinos, 0.01% into photons, and 1% into kinetic energy ejecting material [48]. Light is produced when the shockwave energises the shells of gas and dust surrounding the star, on a timescale set by the propagation of the shockwave

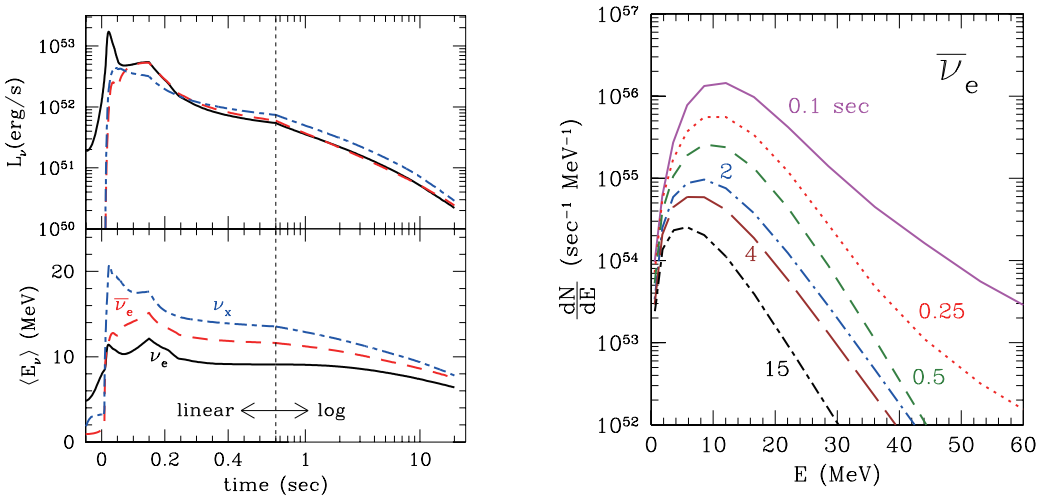


Figure 3.6: Neutrino luminosity (top left), and energy (bottom left), against time from core bounce; and neutrino energy spectrum (right) at various times. Model shown is of 13 $M_\odot$ progenitor with solar metallicity and 100 ms shock revival. Thick lines show output of simulation. Thin lines show Fermi-Dirac distributions at same luminosity and average energy. Reproduced directly from Nakazato et al. [52]

(slower than the speed of light), meaning that light emission is delayed hours after the neutrino burst.

Neutrino oscillation effects during core collapse are complicated by the extreme density. As well as MSW-type transitions, collective oscillation effects and neutrino self-interactions are relevant.

3.3 SN1987A

SN1987A was observed in the LMC, at a distance of $\sim$ 50 *kpc*, in 1987. A $\sim$ 10 *s* burst of O(10 MeV) neutrinos was detected at three detectors: Kamiokande II [17], IMB [18], and Baksan [19]. These events were in time coincidence, within absolute timing uncertainty and expected random fluc-

tuation. SN1987A was the first SN to have its neutrinos detected, was the first naked eye visible SN since Kepler's SN in 1604, and was the first SN to have a known progenitor - identified as a blue supergiant [53]. The identification of the progenitor as a massive star confirmed the origin of SNe [47]. SN1987A was observed in radio, infrared, visible light, ultraviolet, and x-ray (see review [47]).

Kamiokande-II was a water Cherenkov detector with a mass of 2.1 kt, and was a forerunner to SK in the same mine. IMB was a water Cherenkov detector with a mass of 8 kt, also deep underground, and located in Ohio. The configurations of IMB and Kamiokande-II both consisted of PMTs facing a volume of ultra-pure water [17, 18]. However, IMB was much less efficient at low energy compared to Kamiokande-II due mainly to its lower photocathode coverage. Both detectors were designed for proton decay and atmospheric neutrino detection, which have higher typical energies than SN neutrinos. Baksan is a liquid scintillator detector located in Russia; also underground, it has a very different configuration to Kamiokande-II and IMB; and it is still operative. Instead of a single large volume, 3150 separate tanks totalling 330 ton are each monitored by single PMTs [19]. Backgrounds were notably higher at Baksan than at the other two experiments.

LSD, another liquid scintillator detector, reported a burst of events hours before the other detectors. The energy and timing of these events is not at all consistent with the detections at the other detectors, and so these events are not usually included [54]. There is currently no consistent physical explanation for their origin other than a very unlikely random coincidence.

All three of these detectors were mainly sensitive to SN $\overline{\nu}_{\mathrm{e}}$ through IBD,

due to its relatively high cross section (see section 2.2). Kamiokande-II observed 16 events, 4 of which are considered to be background due to being energetically consistent with the background spectrum; IMB observed 8 events, Baksan 5 events [55, Table III]. The time and energy of these events is shown in Figure 3.7. The time axis starts with the first event in each dataset, as the absolute timing uncertainty is quite large.

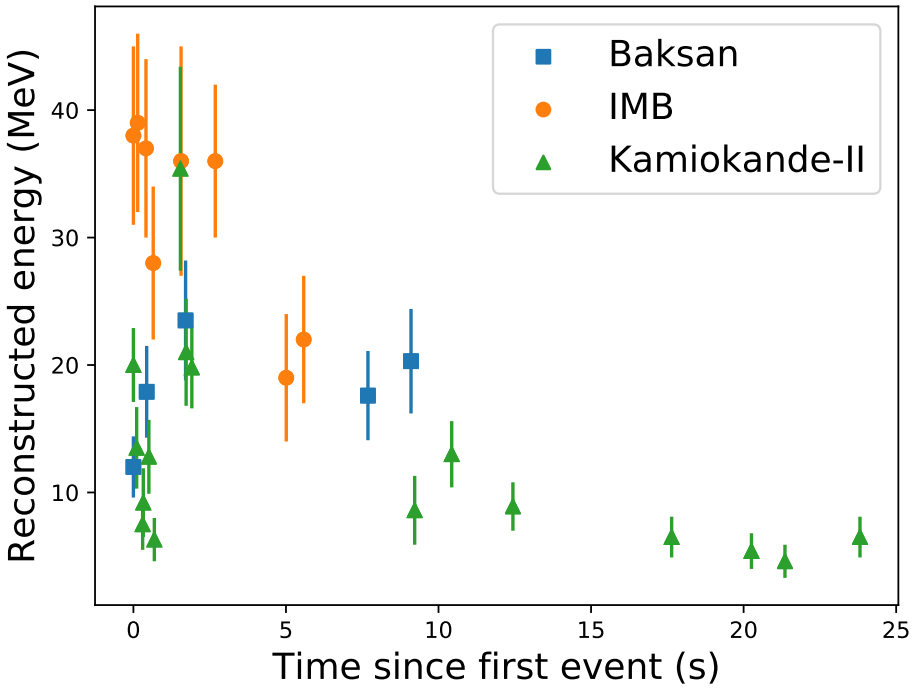


Figure 3.7: Energy distribution of neutrinos detected in coincidence with SN1987A. The time axis starts with the first event in each dataset, as the absolute timing uncertainty is quite large.

This small collection of events generally agree with the expected characteristics of a CCSN. A delayed explosion is preferred over a prompt explosion, and the energy dependent signals at all three detectors were mutually con-

sistent. The average energy of $\overline{\nu}_e$ was estimated to be around 15 MeV, and estimates of total neutrino energy and core radius are consistent with expectation [55].

Despite this, SN1987A is not thought to be a typical CCSN. The very rapid brightening, 10× faster than expected, suggests a more compact object than a red supergiant (RSG). Surprisingly, the progenitor was blue at the time of explosion [47]. Optical observations of the progenitor suggest a luminosity range that was consistent with C burning in a 15-20 $M_\odot$ star [54]; this mass range is consistent with the estimated neutrino energy release. At the time, SN progenitors were generally assumed to be RSGs. The lower metallicity of stars in the LMC may explain this [47].

The detection of $\overline{\nu}_e$ from SN1987A also placed an upper limit on neutrino masses (a high effective mass would spread out the arrival time of the burst), and a lower limit on their lifetime (as they need to travel far enough to reach Earth, their relativistically stretched lifetime must be longer than the time of flight) [54].

3.4 21^{st} Century Supernova Neutrino Detection

Many more detectors are now capable of detecting SN neutrinos than in 1987. Detection of neutrinos is synergistic with optical and near-infra-red observations [46]. As well as probing the physics of the collapse, detection of neutrinos can tell optical astonomers when and where to look for a galactic

SN.

Broadly speaking, desireable features in a SN neutrino detector are

- Mass - more mass means more neutrino interactions.
- Low background - the rate during the burst must be high enough compared to background. Underground detectors are generally better.
- Energy threshold must be low enough to see SN neutrino events
- Energy and time resolution, as these are the features of the burst we are interested in.
- Flavour sensitivity, as different features of the burst appear only in certain flavours.
- Angular resolution for identifying the direction to the SN from elastically scattered electrons.
- Up-time and longevity, as SNe are rare events it is important not to miss them.

Together, this information could be used to discriminate differences between the many CCSN models that have been produced. SK does well on most of these points. To some extent flavour sensitivity and angular resolution will be improved by Gd loading, as IBD events will be increasingly separable from elastic scattering events and quasi-elastic scattering on O (see comparison of effective cross sections in Figure 2.1).

3.5 Supernova Relic Neutrinos

The DSNB flux, also known as the supernova relic flux (SRN), is the isotropic and homogeneous flux created by the sum of all SNe in the history of the universe. Though the DSNB exists in all neutrino flavours, $\overline{\nu}_{\mathrm{e}}$ IBD on hydrogen (H) is the most useful channel for detection due to its high cross section at the relevant energies (see section 2.2). The total flux is small compared to other sources on Earth, such as atmospheric and reactor neutrinos, but occupies an intermediate energy range, giving a window for observation.

The estimated DSNB energy spectrum comes from integrating the SN neutrino energy spectrum over the estimated rate of SNe over the history of star formation in the universe, accounting for redshift. Many different methods have been suggested for estimating the rate of SNe in the universe, mostly based on cosmic chemical abundance; estimates based on the star formation rate, in turn based on observations of the population of young stars, are thought to be particularly accurate [56].

The DSNB flux has never been detected. SK currently sets the best limits, which are close to the upper bound of theoretical predictions [57, 58]. However, SK studies in pure water are background limited, despite the use of neutron tagging on H: gradually increasing the exposure time of SK will not improve the limit. Figure 3.8 shows theoretical spectra for the DSNB flux, compared to other neutrino fluxes. Figure 3.9 shows the limits set by SK, which are within an order of magnitude of some of the flux predictions.

In the 2011 study [58], the largest backgrounds remaining were atmospheric $\nu_{\mu}/\overline{\nu_{\mu}}$ charged current (CC) events, and atmospheric $\nu_{\mathrm{e}}/\overline{\nu_{\mathrm{e}}}$ CC events.

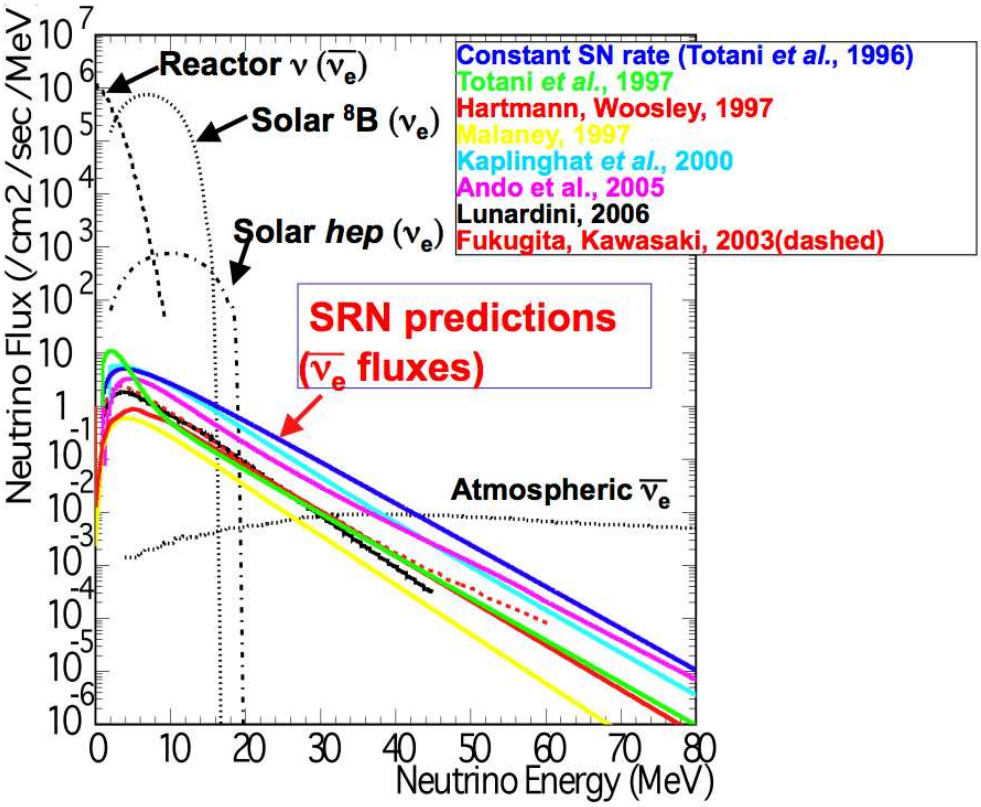


Figure 3.8: Predictions of DSNB/SRN flux spectrum, compared to other neutrino fluxes. Reproduced from [59]. Note that solar neutrinos do not comprise a large background to DSNB as the majority of such events are elastically scattered electrons closely correlated with the solar angle - see [58]. Atmospheric ν_e, ν_μ and reactor neutrinos do contribute to the background.

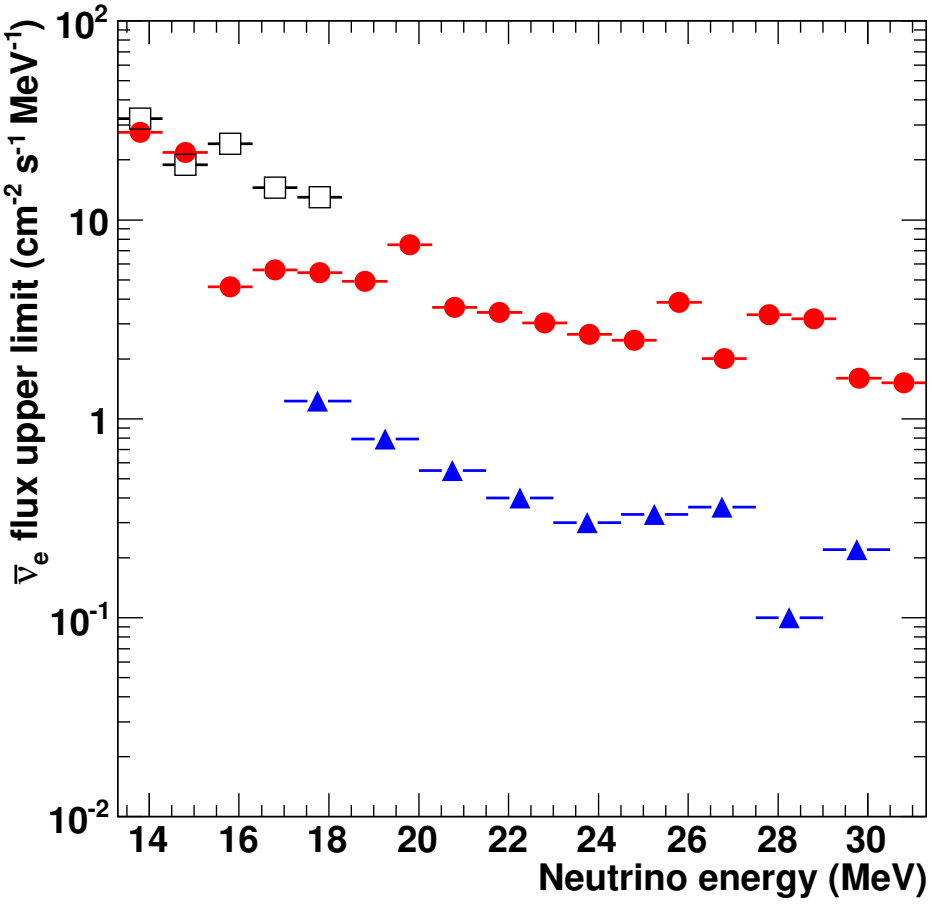


Figure 3.9: Limits on DSNB flux reproduced from [57]. Red circles show limits using SK data using hydrogen tagging published in 2015, blue triangles show limits using SK data taken before hydrogen tagging was available, and open squares show the limits published by KamLAND. Limits are within an order of magnitude of many of the predicted fluxes shown in Figure 3.8.

$\nu_\mu/\overline{\nu_\mu}$ CC can produce muons below the Cherenkov threshold and so go undetected; their decay e^+/e^- then forming the detected background. Atmospheric $\nu_e/\overline{\nu_e}$ CC events cannot be distinguished from DSNB $\overline{\nu_e}$ on an event by event basis but have a very different spectrum. Other backgrounds such as pions are distinguished by their reconstructed Cherenkov angle.

In a later study that made use of neutron tagging with H [57, 60], reduced background allowed the lowering of the energy threshold and reduced overall backgrounds. However, neutron tagging relied on upgrades to the detector DAQ (see section 4.5), so the amount of exposure time analysed was smaller, and therefore stronger limits than those set in 2011 could not be made at higher energies. Atmospheric $\nu_\mu/\overline{\nu_\mu}$ CC only produces neutrons directly 30% of the time, but pions can produce secondary neutrons. Atmospheric $\overline{\nu}_e/\overline{\nu}_\mu$ CC and atmospheric neutrino neutral current (NC) elastic events all make neutrons. However, due to the higher neutrino energies, neutrons produced by atmospheric neutrinos have higher energies so may travel significantly further from the lepton prompt vertex than for the signal. Furthermore, atmospheric NC events can make multiple neutrons, which could lead to their discrimination [60]. The lower threshold was limited by spallation daughters, so improved spallation identification could improve this further.

Through the enhanced neutron tagging provided by Gd, SK will be able to detect the DSNB in a few years; non-detection would require new physics [61, 56]. Detection of the DSNB flux would probe the average supernova neutrino spectrum and rate of SNe.

3.6 Pre-SN Neutrino Signal

In the final stages of stellar fusion before a CCSN, thermal processes, as well as β^- decay and e^+ capture contribute to $\overline{\nu}_e$ emission. At these high temperatures a large equilibrium population of positrons exists, leading to neutrino emission by pair annhiliation

$$e^+e^- \rightarrow \overline{\nu}\nu, \tag{3.4}$$

which is important for detection prospects due to the high flux and relatively high average energy [37, 34]. As shown by Figure 3.10, pre-SN $\overline{\nu}_e$ emission is at much lower energies than those of a SN. Furthermore, the comparison in Figure 3.12 shows that pre-SN emission is over a very long timescale compared to SN emission.

Neutrino emissions are calculated from the thermodynamics of stellar models. Although there are several sets of predictions published for the flux of $\overline{\nu}_e$ from a pre-SN, the studies in this thesis primarily uses the datasets of Odrzywolek and Heger [43] (data downloaded from [62]) and Patton et al. [37] (data downloaded from [63]). Patton et al. [37] predict similar $\overline{\nu}_e$ total emission rates to Odrzywolek and Heger [43] for a $15M_\odot$ star, as shown in Figure 3.11 and Figure 3.13, though the time and energy dependent emission rates differ. The flux estimates of Odrzywolek and Heger [43] are calculated by post-processing the output of an already existing stellar model, and isotopic composition is calculated by assuming nuclear statistical equilibrium (NSE) [64]. The NSE treatment has the computational advantage of depending only on temperature, density, and electron fraction, making it much more

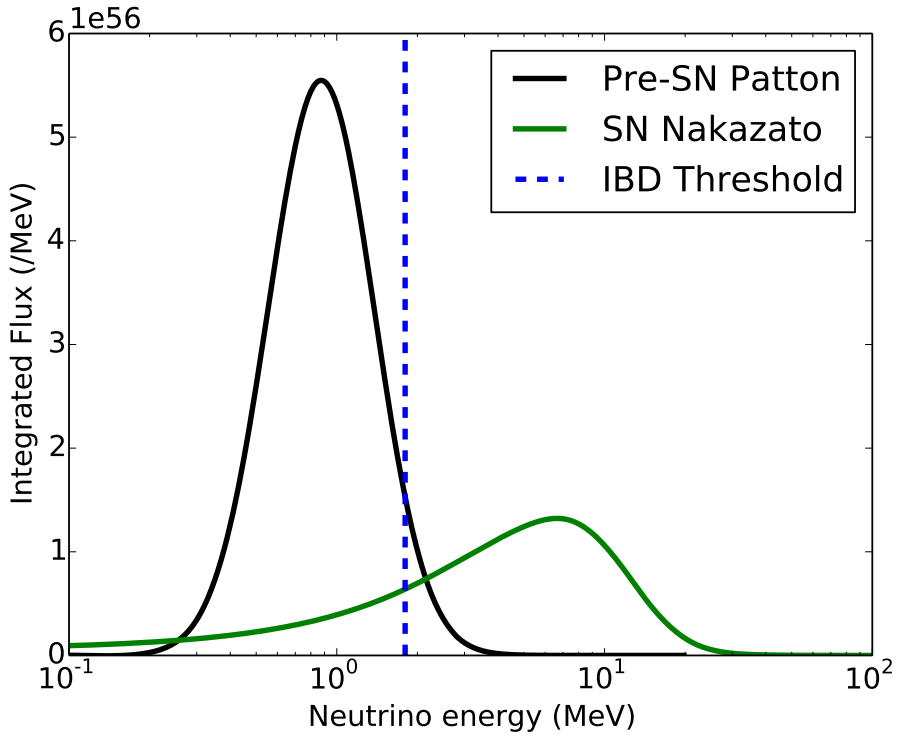


Figure 3.10: Total emission versus energy for $\overline{\nu}_e$ from pre-SN and from a SN burst, integrated over the full time range of the respective models. The dotted line shows reaction threshold of IBD. pre-SN spectrum shown is a 30 $M_\odot$ model from [37], SN spectrum is 30 $M_\odot$ from [52]. 30 $M_\odot$ was chosen so that the two would have the same mass. Note that the pre-SN neutrinos are emitted over a much longer timescale (1000 hours vs. 20 seconds, see Figure 3.12), and that the IBD cross section is strongly energy dependent.

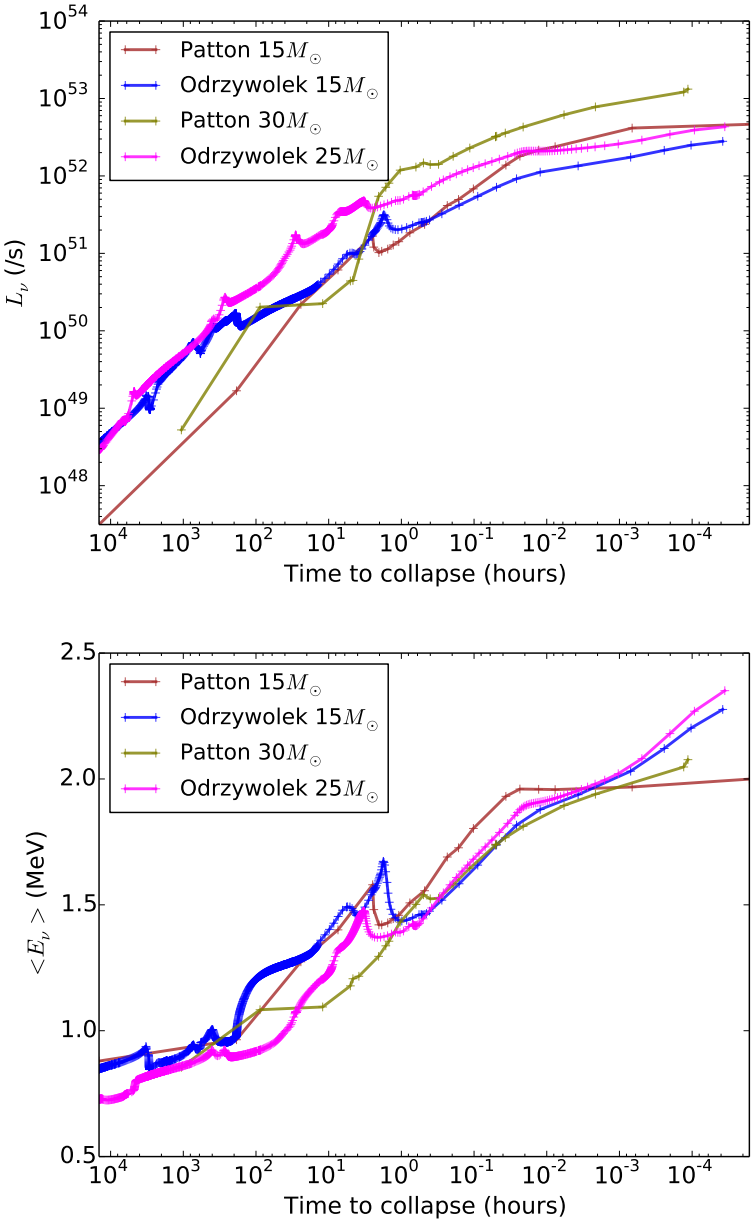


Figure 3.11: Comparison of L_ν number of, and $< E_\nu >$ mean energy of emitted $\overline{\nu}_{\mathrm{e}}$, against time to core collapse, in models by [43] and [37].

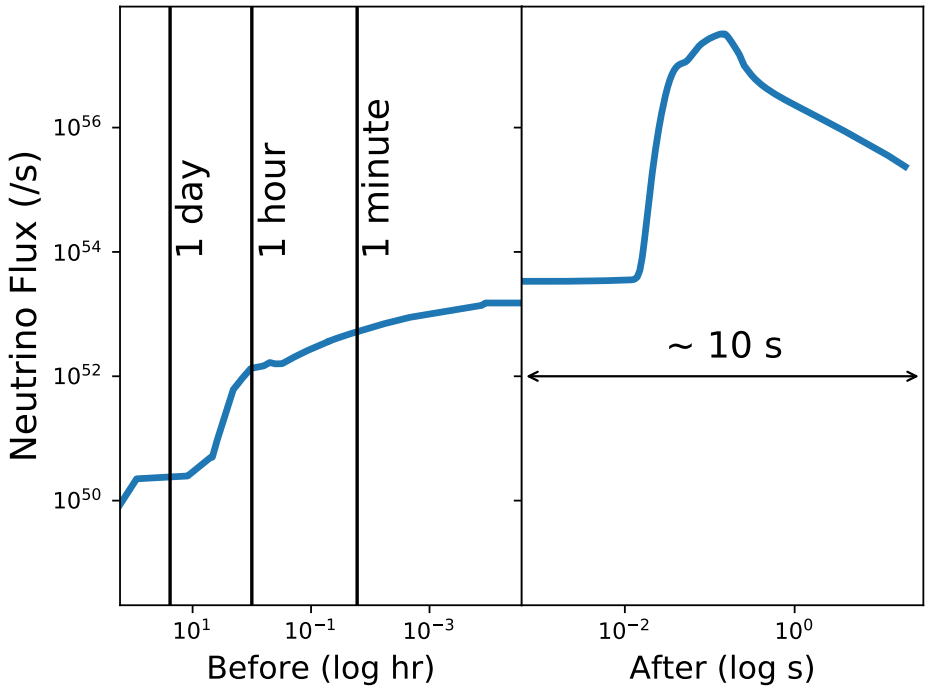


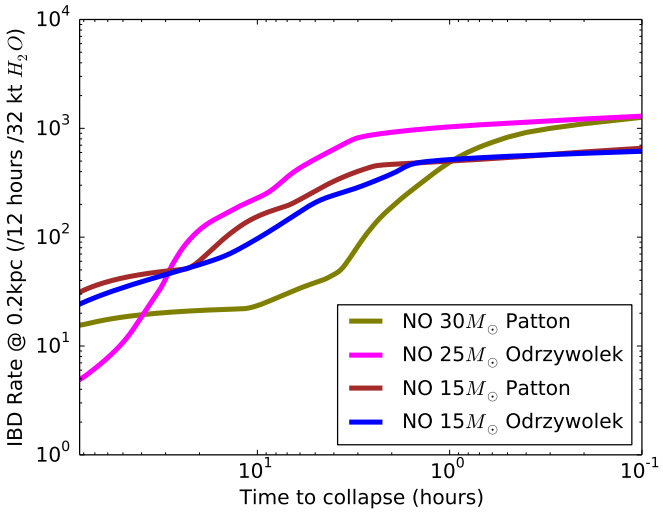
Figure 3.12: Comparison of neutrino emission against time before (left) and after (right) the start of core collapse. Note that the energy of the pre-supernova neutrinos is lower making them less detectable (see Figure 3.10). Models used are 30 $M_\odot$ from Patton et al. [37] and 30 $M_\odot$ 100 ms revival time from [52]

straightforward to post-process an already existing stellar model. Patton et al. [37, 50] use a more modern stellar evolution code, which fully couples the isotopic composition to the stellar evolution and tracks the rates of a larger number of isotopes individually. Isotopic composition especially affects the rate of neutrinos produced by weak nuclear processes.

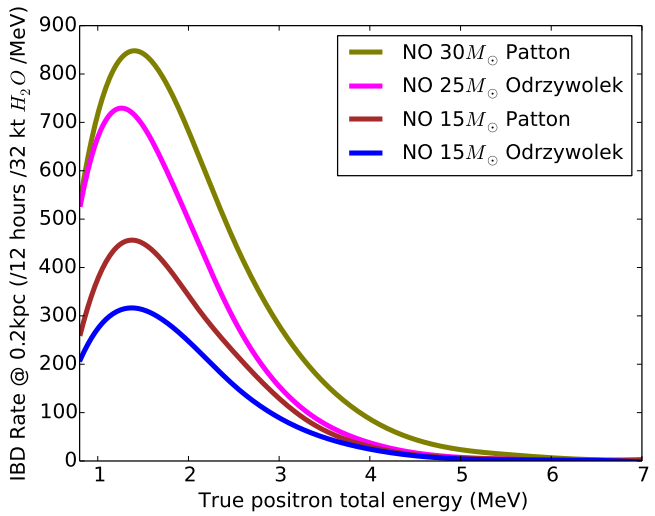
Time $t = 0$ is taken to be the moment at which the simulation is terminated (when the infall velocity exceeds some threshold), which can be taken as the beginning of core collapse. Figure 3.13 contrasts the time dependent predicted IBD rates and the positron energy spectra from the models considered.

Figure 3.14 shows the emission and average energy of $\overline{\nu}_{\mathrm{e}}$ from beta processes (i.e. β^- decay and e^+ capture) and pair production in a pre-SN stellar model produced by Patton et al. [37, 63]. Until the final minutes before collapse, emission by pair production is much higher than that from beta processes, although the average energy is higher for $\overline{\nu}_{\mathrm{e}}$ from beta processes. The majority of the flux above 5 MeV $\overline{\nu}_{\mathrm{e}}$ energy in the most likely period of detection comes from pair production, despite the higher average energy of those from beta processes, as shown in Figure 3.15.

The electron flavour ratio of the neutrinos is affected as it passes through the dense stellar medium. Following [37] and [36], an adiabatic transition is assumed, and the flavour is changed at the high MSW resonance, dependent on the neutrino MO (see section 2.4). The assumed transition probability is $P(\overline{\nu}_e \to \overline{\nu}_e) = 0.675(0.024)$ in the normal (inverted) MO case, and $P(\overline{\nu}_x \to \overline{\nu}_e) = 1 - P(\overline{\nu}_e \to \overline{\nu}_e)$. In the data of [37], the $\overline{\nu}_{\mathrm{x}}$ flux is provided. For the data of [43], the initial $\overline{\nu}_x/\overline{\nu}_e$ ratio assumed to be 0.19 following [44]. This



(a) IBD rate in 32 kton vs. time in a 12 hour integration window



(b) IBD rate in 32 kton in final 24 hours before CCSN vs. positron true total energy, only shown above Cherenkov threshold.

Figure 3.13: Comparison of total number of IBDs in a 12 hour window (a) against time to core collapse, and (b) against energy at the final time step, predicted in models by [43] and [37]. A distance of 200 pc is assumed. Note that a reduced time range is used compared to Figure 3.11. Interpolation has been used to produce equally spaced time and energy points.

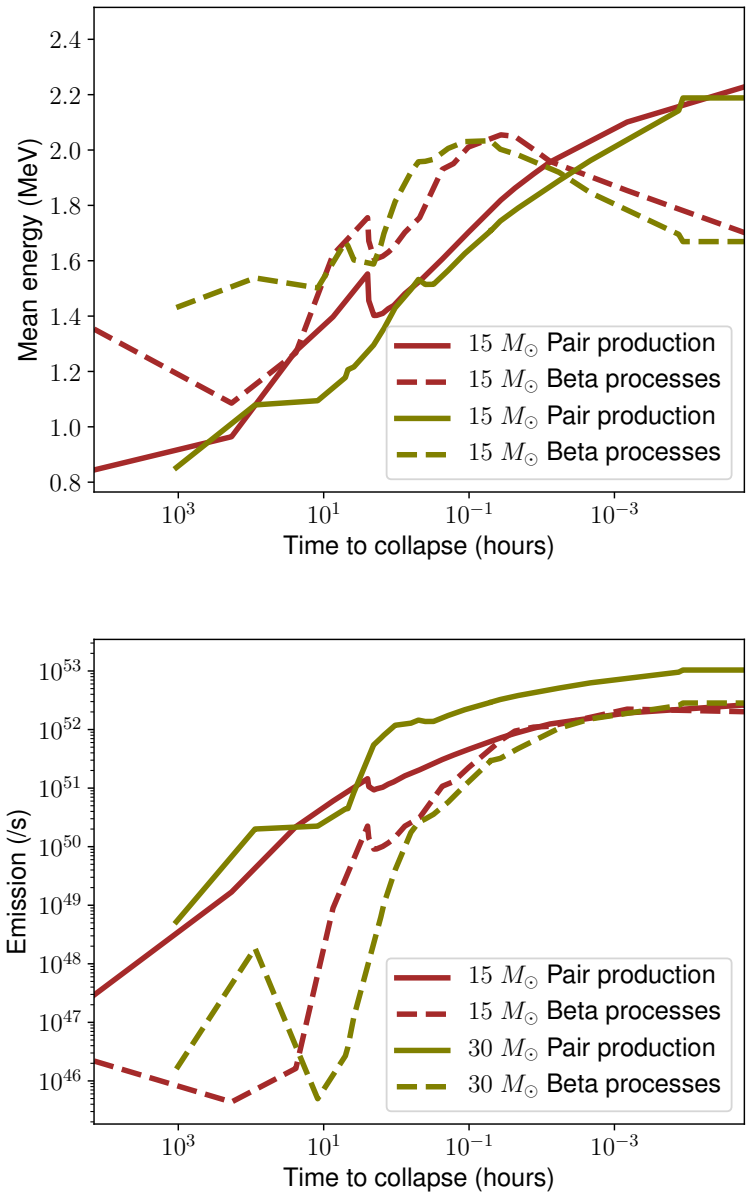


Figure 3.14: $\overline{\nu}_e$ emission and average $\overline{\nu}_e$ energy from pair production (the dominant thermal process) and beta processes (β^- decay, e^+ capture) in the model of Patton et al [37, 63].

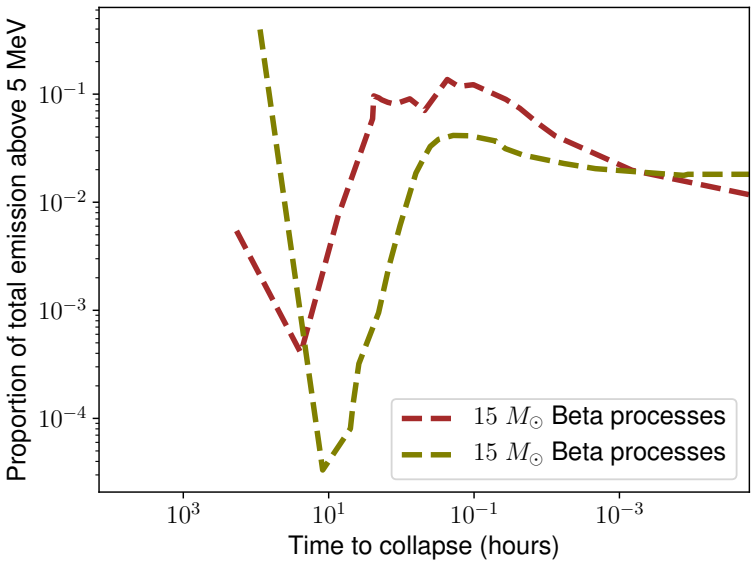


Figure 3.15: Proportion of $\overline{\nu}_e$ emission above 5 MeV $\overline{\nu}_e$ energy originating from beta processes in the model of Patton et al [37, 63].

is assumed to not be energy dependent, and includes the effect of vaccum oscillations. Earth matter effects have not been included. Only the electron flavour fraction will interact through IBD, the rest of the flux is assumed to be invisible in this energy range at SK.

SK-Gd has a chance of detecting a neutrino-cooled star in the core Si burning, shell Si ignition, or direct pre-collapse stage, as the rate of $\overline{\nu}_e$ emission, and crucially the $\overline{\nu}_e$ average energy (Figure 3.11), increase as the star approaches core collapse [43].

The mean $\overline{\nu}_e$ energy is below the IBD threshold, meaning only the tail could possibly be detected through IBD; the increasing average energy will mean that the proportion above threshold will also increase. For a sufficiently nearby star, SK-Gd would see a rapid increase in the rate of low energy IBD

candidate events. This would presage a CCSN by hours.

There are 41 red supergiant (RSG) stars with distance estimates within 1 kpc, 16 within 0.5 kpc, and 5 within 0.2 kpc (see Appendix A for table reproduced from [65]). Famous nearby RSGs include Betelgeuse (α Ori), Antares (α Sco), and ϵ Peg. Wolf-Rayet stars are also possible supernova progenitors, e.g. γ Vel A.

Chapter 4

The Super-Kamiokande Detector

In this chapter, the basic details of the SK detector are described, including its history of data collection in section 4.2, the structure of the detector in section 4.3 and its water systems in section 4.4, a description of its electronics in section 4.5 and triggering systems in section 4.6, and how key calibrations are performed in section 4.8. Details specific to the gadolinium-loaded phase of SK will be discussed separately in chapter 5.

4.1 Cherenkov Emission

The basis of all studies at SK is the detection of the passage of charged particles, by the collection of Cherenkov photons. Cherenkov photons are emitted when a charged particle travels with a speed greater than the phase velocity of light in a medium $\frac{c}{n}$ [66, 67], where n is the refractive index of the

medium and c the speed to light in vacuo. Therefore, the threshold kinetic energy above which an electron or positron will emit Cherenkov radiation in pure water is 0.257 MeV. The kinetic energy Cherenkov threshold for muons is 70.1 MeV due to their higher mass. Gamma rays can be detected indirectly, through Compton scattering and pair production.

Detection thresholds at SK are typically higher than the Cherenkov threshold, as not all photons are detected - with its standard DAQ configuration SK has 100% trigger efficiency for positrons above 4.5 MeV kinetic energy within its nominal fiducial volume (FV). Nominal FV is the volume $> 2\ m$ from the detector wall, totalling 22.5 kton of water. Cherenkov photons are lost due to attenuation in the water: typically 75-82% of Cherenkov photons will travel far enough to reach the inner detector (ID) PMTs depending on water quality [68]. The photocathode coverage of the detector (40% in SK-IV), and the quantum ($\sim$ 21%) and collection ($>$ 70%) efficiencies of the PMTs [67] means that many will not be detected even if they do reach the ID wall. At low energy, representative numbers are 6-8 hits per MeV, with around 11 dark noise hits expected per event.

4.2 Periods of Data Collection

The period during which SK has collected data so far is divided in five periods, each with different hardware configurations. SK-I refers to the period from initial commissioning in April 1996, until July 2001.

In November 2001, before the beginning of SK-II, while the tank was partially filled with water, a large number of PMTs were destroyed acciden-

tally. This is thought to be because a PMT imploded, creating a pressure wave, causing other PMTs to implode in a cascade [67]. The 47% of PMTs that remained were redistributed evenly around the detector, and SK-II ran from October 2002 to October 2005. In order to prevent further implosion cascades, PMTs were fitted with casings designed to dampen pressure waves, made of fibre reinforced plastic (FRP) with an transparent acrylic window in front.

The full number of PMTs was restored for the beginning of SK-III, which ran from July 2006 to September 2008. SK-IV began in September 2008, following an upgrade of the data acquisition (DAQ) system from ATM to QBEE boards (see section 4.5). SK-IV finished in May 2018 , and a long summer shutdown allowed for maintenance and preparation for SK-Gd (see chapter 5).

SK-V began on 29 January 2019, with the first stage of Gd loading to begin in March 2020.

4.3 Detector Structure

SK consists primarily of a tank of ultra-pure water with diameter 39.3 m and height 41.4 m. More accurately the tank is a hole dug into rock, with a lining of stainless steel plates backfilled with concrete. The overall structure of the detector is shown in Figure 4.1. The top of the tank is also covered with stainless steel, which provides a platform for much of the high voltage (HV) and DAQ electronics. The tank is accessible through two large hatches in this platform, and a large number of smaller ports can be used to insert

calibration equipment into, or take water samples from, the tank.

A cylindrical steel frame, called the support structure, holds both inward and outward facing PMTs. The support stucture is 2-2.5 m from the outer wall of the tank, and is 55 cm thick. The volumes inward and outward from the support structure are referred to as the ID and outer detector (OD) respectively.

The ID is the main sensitive volume of the detector. The mass of water inside the ID is 32 kilotons. The OD is used to identify whether or not tracks start or stop inside the ID, which can be used as a veto when identifying events from neutrinos, or for identifying whether muons are stopped in the detector.

Facing into the ID are 11,129 50 cm diameter Hamamatsu Type R3600 PMTs, while facing the OD are 1,885 20 cm diameter Hamamatsu Type R1408 PMTs.

In the ID, PMTs are spaced in a grid with 70.7 cm pitch, and the area between PMTs is covered with opaque black plastic (polyethylene terephthalate) [67]. A photograph of the inner detector is included in Figure 4.2. The inner surface of the tank, and the space beween PMTs in the OD, are covered with a reflective synthetic material called Tyvek, and OD PMTs are backed by 50x50 cm plates of wavelength-shifting doped acrylic; this increases the efficiency of light collection for OD PMTs.

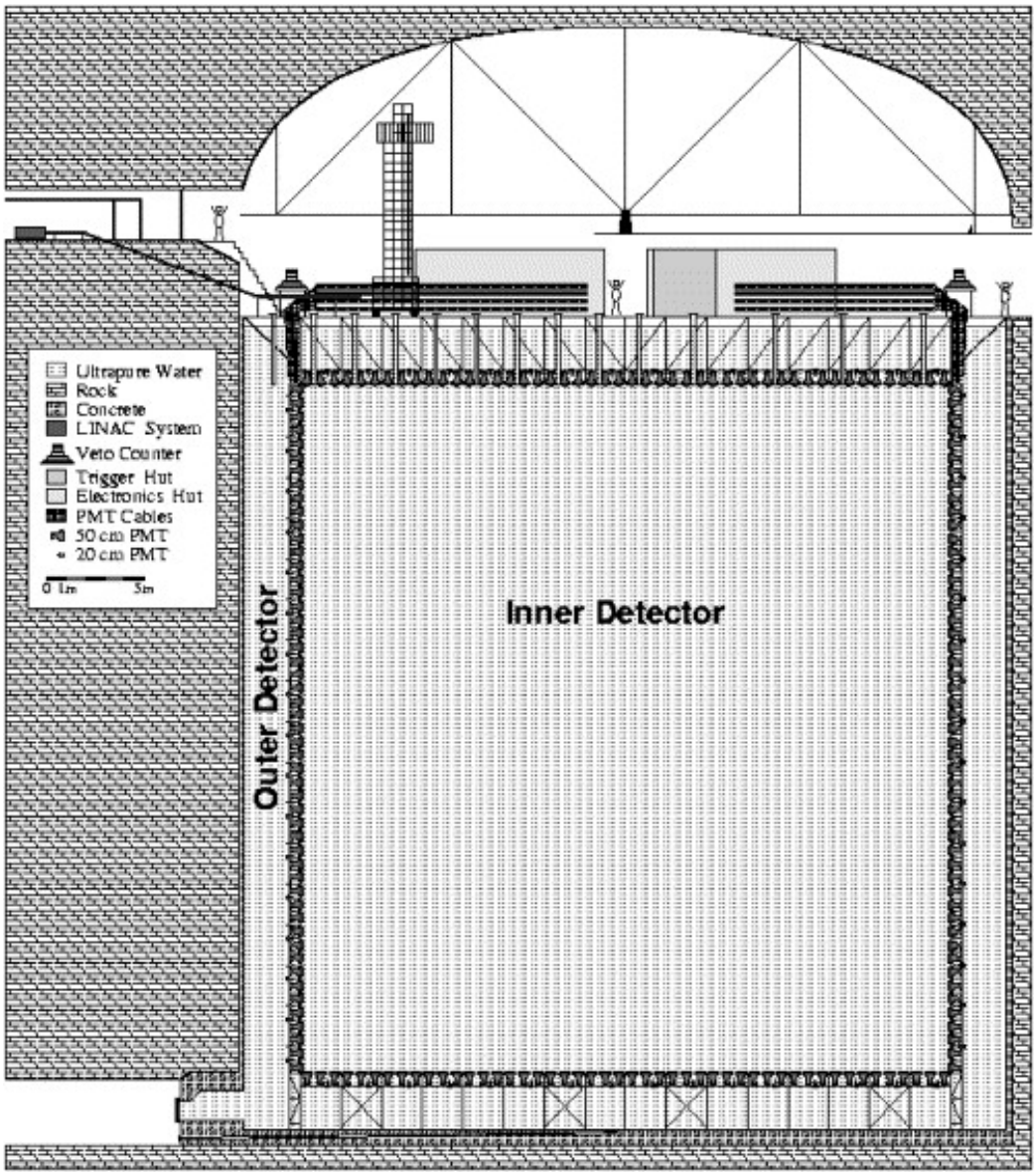


Figure 4.1: Scale diagram of the SK detector, reproduced from [67].

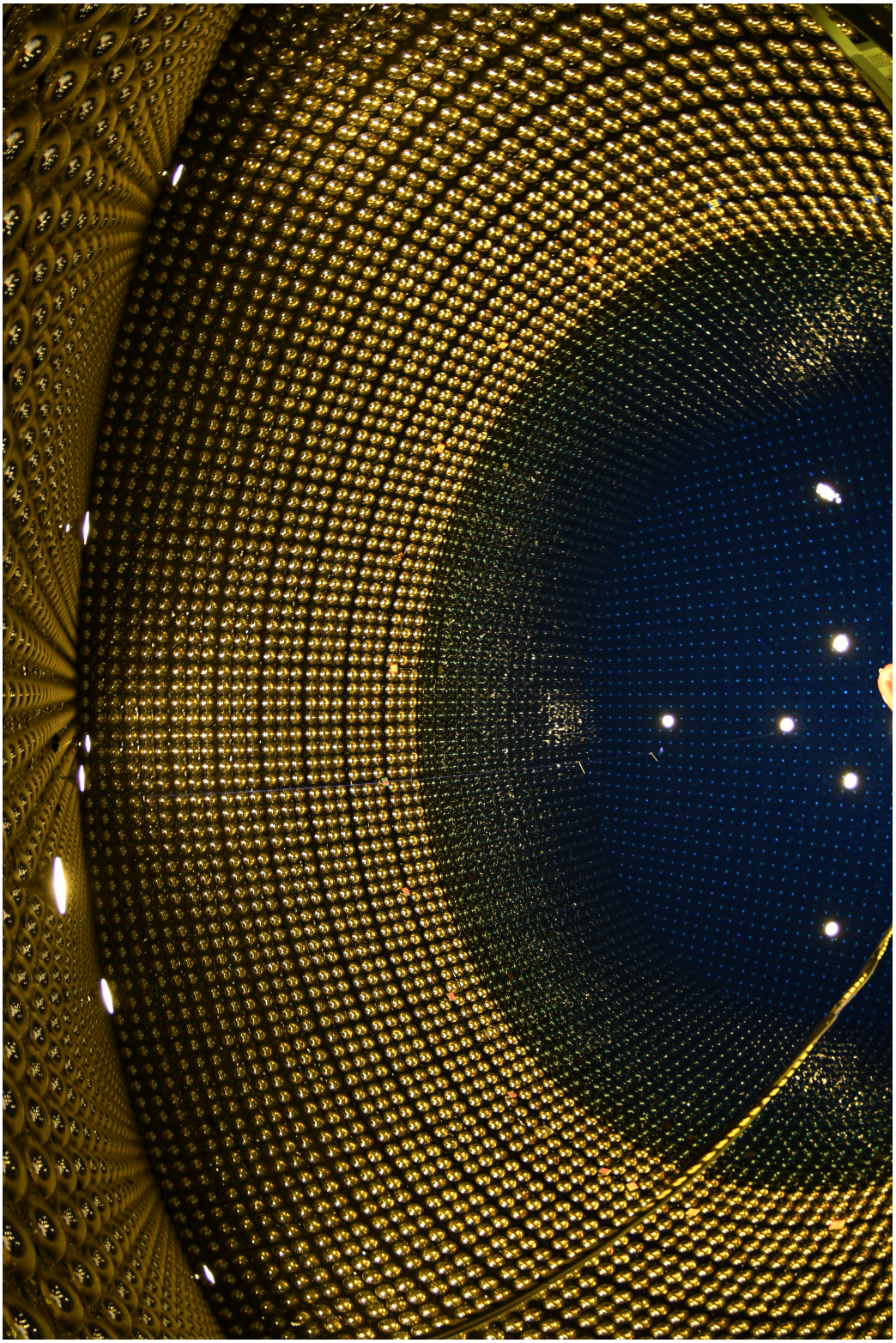


Figure 4.2: Photograph of the SK inner detector taken during 2018 tank open work. Taken from the top looking down, with the tank partially drained. © ICRR, University of Tokyo

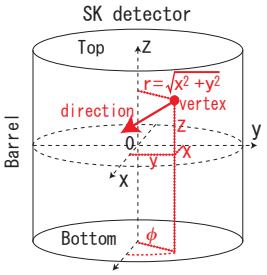


Figure 4.3: SK coordinate system, reproduced from [70].

The ID and OD are optically separated by a layer of Tyvek on the OD side of the support strucure, and a layer of black opaque plastic on the ID side. This optical separation is vital, as the OD is used to identify whether or not tracks start or finish outside the ID.

SK is located in the Kamioka mine (from which the experiment takes its name) in Gifu prefecture Japan. This is a drift mine dug horizontally into a mountain. The location was chosen as the 1 km of rock above the detector serves to reduce the rate of cosmic ray muons passing through the detector. Observed cosmic ray muon rates are roughly 2 Hz, with a flux of $6 \times 10^{-8}\ cm^{-2}s^{-1}sr^{-1}$ [67].

The vertical component of the geomagnetic field, which would have a negative effect on the response of the PMTs, is compensated by sets of coils around the inner surface of the tank [69]. From SK-III onwards, barrel and endcap parts of the OD are separated with a layer of Tyvek.

Detector response in SK is modelled using a Monte Carlo simulation built on the GEANT3 framework, called SKDETSIM. The origin of the coordinate system in the detector is taken to be the centre of the tank, with the z-axis pointing up, as shown in Figure 4.3.

4.4 Water Systems

4.4.1 Pure Water

Impurities affecting water transparency can be particulates, bacteria, dissolved gases, ions, or organic compounds.

The schematic of the SK pure water system is shown in Figure 4.4. In order to maximise the number of detetected photons, the SK water must be maintained to very high transparency. UV lamps kill bacteria, filters remove dust and other particulates, and reverse osmosis is used to remove even smaller particulates. An ion exchange resin, called a cartridge polisher, is used to remove heavy ions. Vacuum and membrane degasifiers are used to reduce radon contamination; also radon free air is dissolved into the water before the degasifiers are used, which effectively flushes out radon, increasing the proportion of radon which is removed [67].

Water is sourced from the natural streams in the mine. Once the tank is filled, water is recirculated to maintain high transparency. Recirculation is necessary as bacteria can grow, and certain materials leech into the water from the materials of the detector itself, gradually reducing water quality. Within the ID, water is injected at the bottom and extracted from the top. Dark noise rates of PMTs are affected by their temperature; making it beneficial to maintain a low water temperature. Injected water is cooled below the ambient temperature of the tank in order to manage convection. With highly precise thermometers it has been established that convection makes water temperature uniform at $z < -11$ m; above this level the temperature rises gradually by 0.2° to the top of the ID [69]. This leads to a difference

in water transparency between the top and bottom of the detector. In order to remove the effects of non-uniform water transparency, it is desirable during some calibrations of the detector to have full convection; this can be achieved with higher water injection temperatures. However, during normal data collection convection is prevented, as this reduces backgrounds due to radioactive contamination in the FV. Low temperatures also suppress the growth of bacteria.

Radon gas is produced by the decay chain isotopes present in the rock, so radon free air is pumped into the cavern, partly for health reasons, and partly to reduce contamination of the detector. Radon levels in the air in the mine range are typically 200 $Bq\ m^{-3}$ to 2000 $Bq\ m^{-3}$ in the winter and summer respectively. Air pumped into the cavern is 40 $Bq\ m^{-3}$, while even lower activity air (O($mBq\ m^{-3}$)) is pumped into the space above the water in the tank. However, there is a large amount of radon emanation from materials inside the detector directly into the water, as well as that entering through the air [71, 72].

4.4.2 $Gd_2(SO_4)_3$ Loaded Water

Maintaining high water transparency is vital to the operation of SK in order to maximise the number of detected Cherenkov photons, and therefore the ability to reconstruct events [69]. Gadolinium sulfate was identified as the most appropriate water soluble compound of Gd, as it does not absorb much light in the range of Cherenkov photons, and is not very reactive so does not affect other detector components [68].

However, the systems used to maintain water quality in SK-IV cannot be used for SK-Gd, as gadolinium sulfate would be removed along with other impurities. This would require the constant replacement of gadolinium sulfate, making the experiment prohibitively expensive. The EGADS detector was able to run for over two years at 0.2% gadolinium sulfate loading, and was able to maintain high water quality during this time, as shown by Figure 4.5. High water quality is defined in this case as the range of transparency values achieved in pure water in SK-III/IV.

In the gadolinium sulfate compatible water system used in the Evaluating Gadolinium's Action on Detector Systems (EGADS) apparatus (schematic in Figure 4.6), water removed from the top of the detector tank is subjected to UV lamps and microfilters, which kill bacteria and remove particulates, and which are compatible with $Gd_2(SO_4)_3$ loaded water. Chillers and heat exchangers are used because $Gd_2(SO_4)_3$ solubility decreases with increasing temperature. A nanofilter is then used to create separate streams of $Gd_2(SO_4)_3$ enriched water and ultra-pure water: water molecules pass the nanofilter while Gd^{3+} and SO_4^{2-} ions do not. The ultra-pure water stream can then be subjected to a de-ionisation procedure that would remove the gadolinium sulfate. The two streams can then be recombined for the remaining purification steps. A fast-recirculation loop applies the purification procedures that are compatible with $Gd_2(SO_4)_3$ loaded water to a larger volume of water; this has been shown to improve water quality, but is insufficient on its own. The anion exchange resins that are used are not the same as those used in the pure-water SK system, and are designed specifically for $Gd_2(SO_4)_3$ compatibility. Total organic compound (TOC) lamps use far-UV

to create free radicals, which oxidise organic compounds into CO_2 and H_2O.

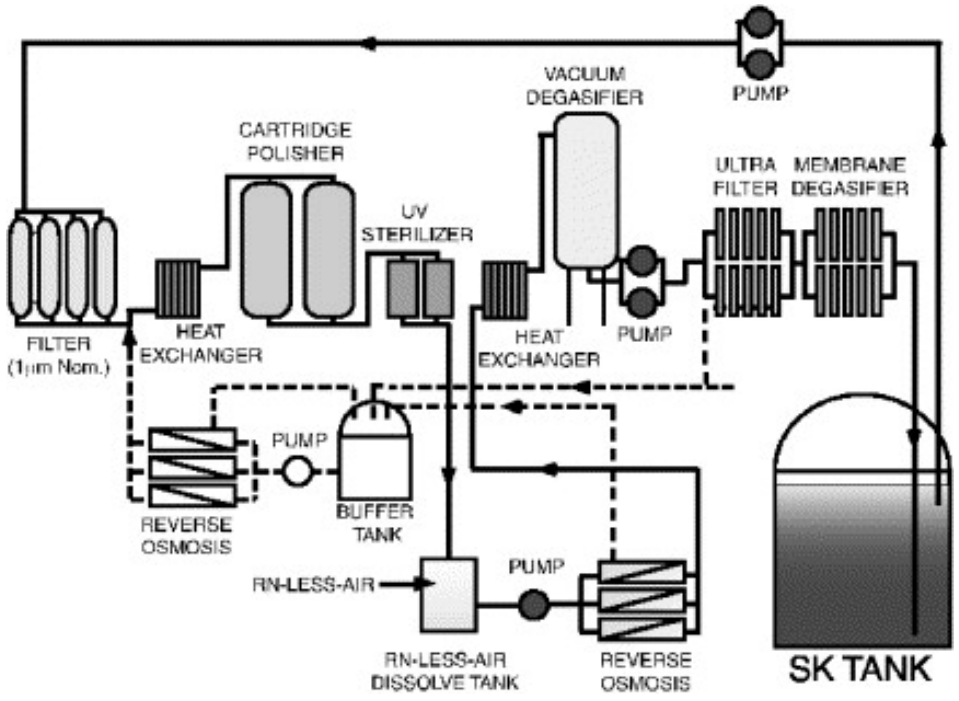


Figure 4.4: Schematic of the SK water system. Reproduced from [67].

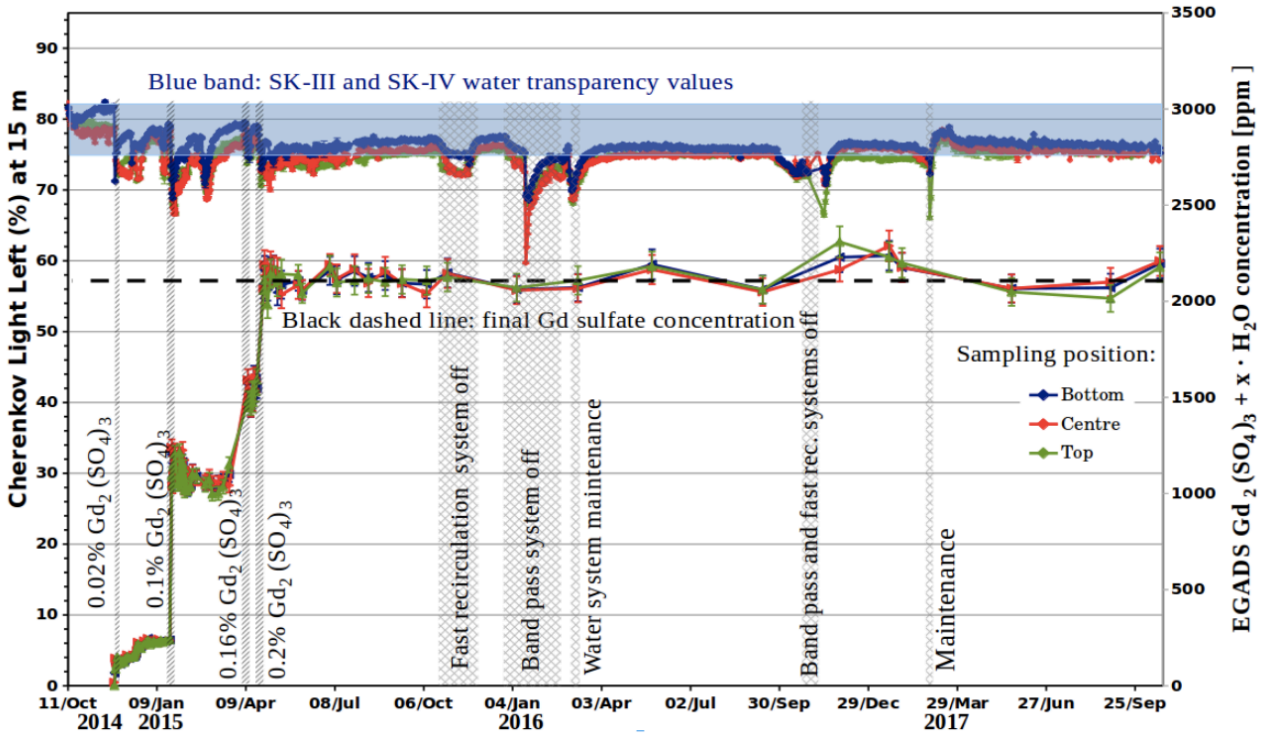


Figure 4.5: The upper plot/left Y axis shows water transparency, measured as Cherenkov light left at 15 m by UDEAL. The blue band shows the range of SK-III/IV water transparency measurements. The lower plot/right Y axis shows gadolinium sulfate concentration. The X axis shows the date. Reproduced from [68].

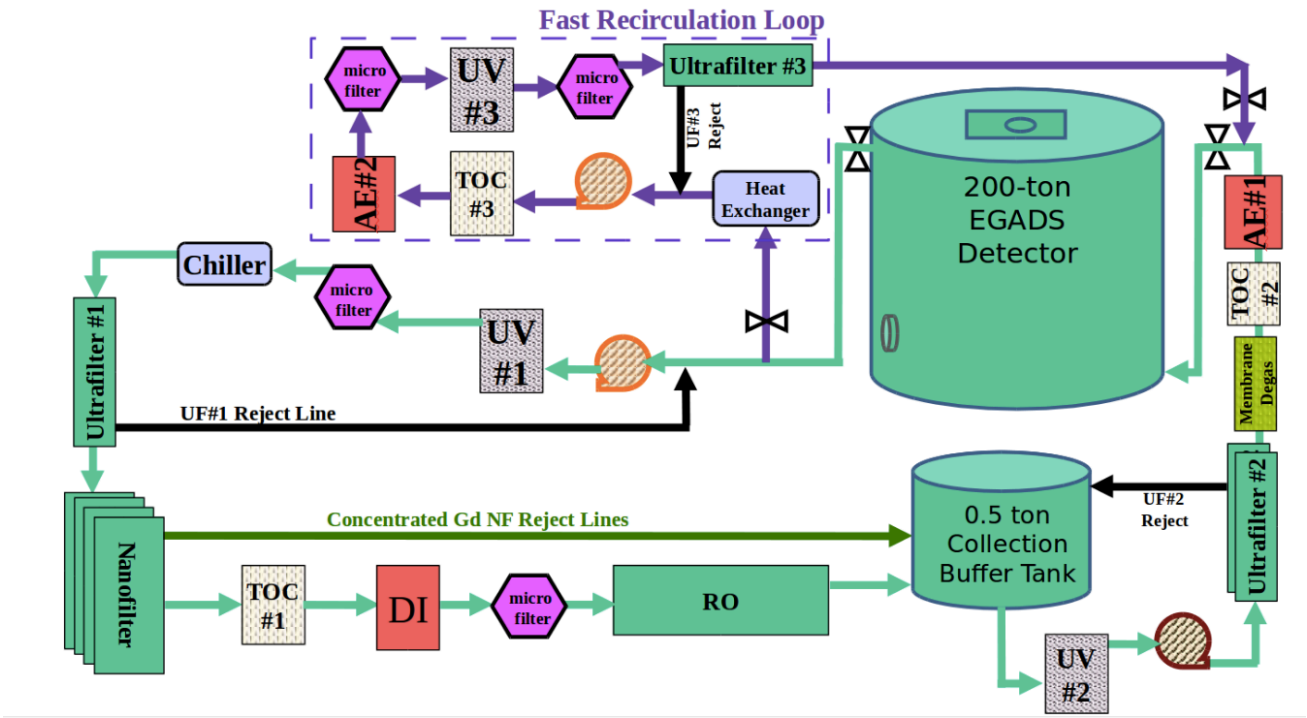


Figure 4.6: Schematic of the EGADS water system, on which the SK-Gd water system is based. AE = anion exchange resin, DI = dionisation, TOC = total organic compound lamp, RO = reverse osmosis. Reproduced from [68].

4.5 DAQ and Electronics

The ID PMTs have a peak quantum efficiency of 21% at wavelengths of 360-400 nm. The range most interesting for detection of Cherenkov photons in water is 300-600 nm: at higher wavelengths PMTs cannot be used to efficiently detect photons, at lower wavelengths the photons do not propagate in water. Photoelectron (PE) collection efficiency, the proportion of PEs which interact with the dynodes and produce a signal, is above 70%. The PE transit time spread (standard deviation) is 2.2 ns [67]. Timing resolution is especially important in the ID because it affects the vertex reconstruction resolution.

SK operates on a triggered readout system. From each pulse created by each PMT, the recorded information is the pulse arrival time and the pulse area (total charge). When a threshold number of PMTs collect above a threshold amount of charge in a set time window, the data of the hit times and recorded charges are saved to disk. This effectively sets an energy threshold: the number of Cherenkov photons produced, and therefore the total charge collected, is highly correlated with the energy of the charged particle producing the light. The width of the time window is set at 200 ns, as this is (approximately) the time it would take light to travel the maximum diagonal distance within the ID [73].

The DAQ electronics in SK-I to III are referred to as Analogue Timing Modules (ATM). In the ATMs, time-to-analogue converters (TAC) and charge-to-analogue (QAC) converters were used [74].

In SK-IV, ATMs were replaced with QTC-based Electronics with Ether-

net (QBEE), which have greater dynamic range, and better charge and time resolution than the ATMs [69, 75]. In the QBEEs, specialised high speed charge-to-time converters (QTC) and time-to-digital converters (TDC) are used. Each QBEE board has 8 QTC chips, each of which accepts 3 inputs. A QTC takes the pulse produced by each PMT, and an analogue signal with width corresponding to the pulse height. The QTC has three gain ranges, and will use the lowest unsaturated range, thereby giving improved dynamic range and resolution. The TDC identifies the leading and trailing edges of the QTC output signal, and delivers the start time and width of the signal as digital data to the data sort mapping (DSM) FPGA. The DSM codes the data received from the TDC into a 6 byte representation containing the source channel, charge, and start time. Another FPGA stores this hit data in first-in-first-out (FIFO) memory. An ethernet interface card provides the data from the FIFO memory to the front-end computers as TCP packets.

Parallel front-end computers sort the hit data into time order in 20 ms blocks. Each 20 ms block overlaps by 1 ms each with the previous and the next block, so that events on the edge of a block are not lost. Parallel merger computers receive blocks of data from the front-end computers via ethernet, sort the received data blocks into time order, and build the hit data into events, applying the trigger conditions. A single organiser computer sorts the data blocks produced by the parallel mergers, with the end result being a single data stream of events sorted in time, which are saved to disk [76].

In the ATM era, the number of hit PMTs, and therefore whether data were read out, was calculated by summing analogue signals. In the QBEE era, every hit is read out, and triggering is handled by software. This has

enabled greater flexibility in trigger conditions, leading to delayed coincidence triggering (AFT), a full data dump in the case of a SN trigger, and the development of the wideband intelligent trigger (WIT) system (covered in section 4.6).

QTC thresholds are set such that a PMT is considered hit if it collects > 0.25 times the peak charge for a single PE. When O(1 PE) is collected by a PMT's photocathode, the timing resolution of a QBEE is 0.3 ns and the charge resolution is 0.1 PE, both of which are better than the resolutions of the PMTs themselves [69].

4.6 Trigger Conditions

The choice of trigger thresholds in SK are determined by the quality of event reconstruction, and background event rate.

An event producing fewer hits is less likely to be well reconstructed, as the recorded hits will be more subject to statistical fluctuations, and as a higher proportion of hits in the 200 ns window will be due to dark noise. Total dark noise rates, the rate at which PMTs produce a pulse consistent with a single PE while in total darkness, at Super-K are around 12 per 200 ns [77]. Dark noise is caused by thermionic emission of electrons from the photocathode, and radioactive decays in the PMT material. For a 10 MeV electron, there will be around 60 PMT hits from Cherenkov photons, whereas for a 5 MeV electron it will be 25-30.

Rates for events with very low numbers of recorded PMT hits are dominated by background, coming from dark noise and radioactive decays within

the detector. These fall rapidly with the number of hits, and so applying a threshold is a simple way to reduce background rates. Trigger thresholds in SK-IV and the associated data rates are listed in Table 4.1. In the ATM era, total data rates were somewhat limited by the dead-time created by read-out. In the QBEE era, all hits are read out, so data rates are not limited, and triggering is handled by online computers running trigger software in parallel. Once a 200 ns time window with a number of hits exceeding the threshold is identified, a longer time window around this is saved: 1.3 μs for the SLE trigger, 40 μs for the LE, HE, SHE triggers (defined in Table 4.1). The wider window means that activity before or after the trigger can be identified.

Following an SHE trigger, if there is no OD trigger, the AFT trigger is activated. All hits in the following 500 μs will be saved by the AFT trigger. This is especially useful for the detection of delayed coincidences from neutron capture. In pure water, neutrons mostly capture on hydrogen within about 200 μs, emitting a 2.2 MeV gamma ray. A 2.2 MeV gamma ray will not typically lead to enough PMT hits to meet the SLE trigger threshold.

The SHE trigger corresponds roughly to $\sim$7.5 MeV electron kinetic energy ($\sim$9.5 MeV before 2011). The SLE trigger is 100% efficient above 4.5 MeV electron kinetic energy.

An online SN monitor writes data directly from the front-end computers into a memory buffer, independent of the rest of the online system. In the case that a burst of events consistent with a galactic SN is detected, the entire buffer is to written disk and an alert is issued [78].

Trigger		Condition	Rate
Wide-band Intelligent	*WIT*	-	$\sim kHz$
Super Low Energy	*SLE*	>34/31 hits	$\sim kHz$
Low Energy	*LE*	>47 hits	$\sim 40\ Hz$
High Energy	*HE*	>50 hits	$\sim 10\ Hz$
Super High Energy	*SHE*	>70/58 hits	
After	*AFT*	(SHE).$\overline{\text{(OD)}}$	
Outer Detector	*OD*	>22 hits in OD	

Table 4.1: SK-IV Trigger Scheme. The SHE threshold was decreased in 2011, and the SLE threshold was decreased in 2015. The AFT trigger saves all hits for 500 $\mu\ s$ following an SHE trigger that is not in coincidence with an OD trigger.

4.7 WIT

The Wide-band Intelligent Trigger (WIT) attempts to reconstruct events from all recorded PMT hits, without initially applying a threshold to the minimum number of hits. This is achieved with increased amounts of parallel computing, making use of a number of additional computing cores located within the Kamioka mine [77]. As the majority of low energy background events are produced by radioisotope decays in the PMT glass and FRP cases, many background events have reconstructed vertices close to the PMTs, and reconstructed directions which point towards the wall nearest to the reconstructed vertex. Events which do not reconstruct well, or reconstruct close to the PMTs, are rejected and not saved to disk.

Firstly, a data block containing time and charge information for a 23 ms block of PMT hits is searched for a coincidence in 220 ns of a number of hits above the calculated dark noise rate plus 11. As there are $\sim 6-7$ hits per MeV from an $e^{\pm}$ in this energy range, this corresponds to ∼2 MeV kinetic energy. The dark noise is calculated live. Hits passing this criterion are

grouped into a 'pre-triggered event'. Vertex reconstruction is then applied in various stages, described in section 4.9, with events kept if they are within the FV.

4.8 Calibration

This section briefly summarises the calibration of SK; more complete information can be found in [69, 79, 80] and references therein.

The first stage of calibration was performed before the PMTs were installed. A subset of 420 PMTs had their HV calibrated ex-situ, so as to have the same charge response, and these are distributed around the detector in a cross shape. The HV settings of other PMTs are tuned to standard PMTs in geometrically similar locations, using uniform light sources at the centre of the tank (scintillator ball driven by a xenon lamp via optical fibre). This allows for the effects of geometry and light propagation to be taken into account without having to separately tune the HV settings of all PMTs ex-situ. The Xe lamp flashes at 1 Hz during normal data collection, allowing variations in water quality, gain, and timing to be taken into account.

Gain is the ratio of total charge of the pulse produced to the charge of PEs emitted by PMT photocathodes. The total charge collected is used to reconstruct the energy of higher energy events, and so gain calibration is important. In lower energy events (up to $\sim$100 MeV [77]), most hit PMTs will collect only a single PE, so energy reconstruction is based upon the number of hit PMTs. In this case it is the product of quantum efficiency and collection efficiency which is more important. Quantum efficiency $\times$

collection efficiency is referred to as QE.

Absolute gain is calibrated using a ball of NiO bonded with polyethylene with a sealed ^{252}Cf neutron source at the centre, which is lowered into the tank on a wire. The combined source emits 9 MeV gamma ray cascades isotropically from the reaction $^{58}\mathrm{Ni}(\mathrm{n},\gamma)^{59}\mathrm{Ni}$, which leads to PMTs mostly collecting a single PE. This allows the distribution of collected charge caused by a single PE, and therefore the gain to be measured. The detector simulation samples from this distribution when determining the response of each PMT to a PE. Simulation is used to calculate the expected number of photons reaching each PMT, allowing QE to be calculated from the hit rate.

The relative gain difference of each PMT is calculated using high and low intensity flashes from a nitrogen driven dye laser via optical fibre and diffuser ball at the centre of the detector. Low intensity flashes mean that only a subset of PMTs are hit, and those that are usually receive a single PEs. From the low intensity flashes, the relative probabilities of a photon being collected by each PMT are calculated. A high intensity flash leads to each PMT collecting some charge > 1 PEs. The charge collected by an individual PMT from the high intensity flash, divided by the probability of that PMT collecting a PE in a low intensity flash, then gives the relative gain of each individual PMT. The measurements of relative gain and QE are anti-correlated. Charge linearity is tested with varying intensity laser bursts.

Timing response can vary between channels due to variations in cable length, PE transit time, or in the readout electronics, and the time-walk effect. The time-walk effect is that the time at which a pulse exceeds a threshold will be faster for a large pulse than a small pulse. Fast pulses from

a nitrogen driven dye laser are injected via optical fibre and diffuser, with intensity controlled by filters. A PMT external to the detector, at the point of laser injection, is used to set the start time of the burst. Differences in timing response with pulse height are measured directly, producing a relation between time response and collected charge. The same measurement leads to a calculation of timing resolution. Timing resolution and the T-Q relationship is monitored in real time, with the laser flashing at 0.03 Hz. HV, timing, and charge calibrations are also performed for the OD.

SKDETSIM uses empirical approximations for wavelength dependent photon scattering. A collimated laser beam is injected into the SK tank via optical fibre [67]. The scattering parameters are tuned using a χ^2 minimisation between the temporal and spatial distributions of the detected photons.

The water transparency difference between the top and bottom of the tank are measured using regularly collected nickel+californium calibration data. It is also visible in other data samples such as those from the Xe lamp, and Michel electrons from stopped cosmic ray muons. This is taken into account by SKDETSIM as a z-dependent modification of the absorption parameter. The wavelength dependent refractive indices of the water, PMT glass and photocathode, and the reflection/absorption coefficient of the black sheet are tuned similarly.

A linear accelerator (linac) is used to inject electrons of known energy into the ID, and has been modified to have very low intensity, injecting electrons one at a time. The linac is situated near the top platform above the tank, with the beam carried in an evacuated pipe, and guided by bending and focussing magnets along the platform to the desired calibration point, and

then aimed downwards. Electrons of different momentum can be selected, between 5-16 MeV/c. The linac provides calibration of the absolute energy scale, energy resolution, and directional reconstruction resolution. By adding and removing sections of pipe, the injection point can be moved vertically and radially, allowing the spatial variations in the response to be taken into account [79].

A deuterium-tritium neutron generator (DTG) provides a cross check on the absolute energy scale. Lowered into the detector on wires from any calibration port and to any depth, the DTG produces a large burst of neutrons and is then raised. ^{16}N is produced in the reaction (n,p), which has a half-life of 7 s, and decays producing a 6.1 MeV gamma-ray and a beta-ray with 4.3 MeV endpoint. In both the DTG and linac calibrations, there is some limitation from the presence of an opaque object in the detector which can cause shadowing. Raising the DTG after the pulse is produced reduces the amount of shadowing [80].

The linac calibrates the energy scale to 1% accuracy within its momentum range. The DTG calibration agrees closely with the linac calibration.

Water transparency also needs to be calculated, as it is an input to the energy calibration. This is done using decay electrons from stopping cosmic ray muons. As the Cherenkov cone is azimuthally symmetric, the light attenuation as a function of distance can be fitted [70].

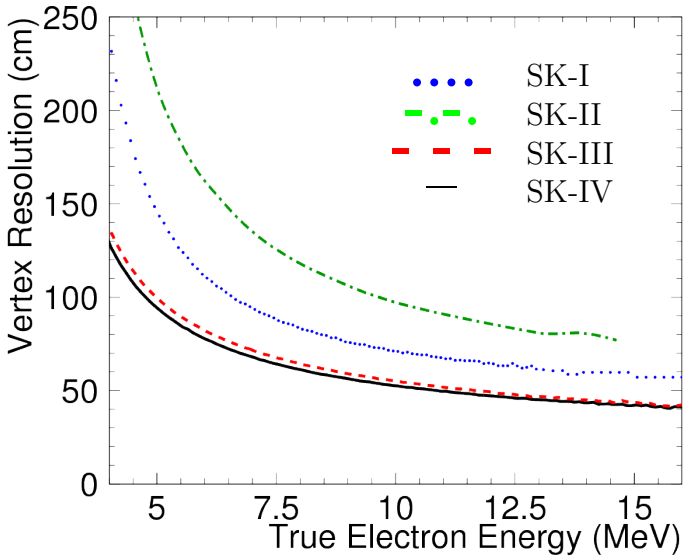


Figure 4.7: Vertex reconstruction resolution in SK against electron true total energy. Evaluated with SKDETSIM.

4.9 Event Reconstruction

4.9.1 Vertex Reconstruction

Electrons and positrons below 10 MeV will not travel far in water, only a few cm. Therefore, it is reasonable to approximate them as point sources for the purposes of reconstruction in SK. The travel distance ends up being small compared to the vertex resolution. Reconstruction in higher energy ranges use different tools not described here. Figure 4.7 shows the relationship between electron true total energy and vertex reconstruction resolution, evaluated with SKDETSIM.

Within the WIT, *Software Trigger Online Reconstruction of Events* (STORE) is the first filter applied to pre-triggered events. The temporal-spatial separation of each hit from each other hit is calculated. The largest set of hits

which are mutually consistent with being from a point source is selected, that is, for which the spatial separation is less than the temporal separation divided by the group velocity of light in water. Four-hit combinations are drawn from this list. For each four-hit combination, a vertex is found for which a timing residual

$$T_{residual} = T_{hit} - T_{flight} - T_{vertex} \tag{4.1}$$

is equal to 0, where T_{flight} is the distance from the hit PMT to the vertex divided by the group velocity of light in water. Vertices which are inside the FV are kept.

Following STORE, a fast vertex fit called *ClusFit* is used. From the list of hits produced by STORE, hits which are further than 1250 cm or 35 ns from any other hit are removed. This is to remove isolated hits assumed to be from reflected light or dark noise. A grid search is then performed to maximise vertex goodness of fit [73]. Again, vertices which are inside the FV are kept.

The vertex goodness of fit (*bgoodness*) is defined by the sum over hits

$$g(T_i) = \sum_{i}^{N-1} w_i e^{-0.5(T_{resid}/\sigma)^2}, \tag{4.2}$$

where σ is an effective timing resolution for Cherenkov events (5ns), and w_i are hit weights intended to reduce dark noise contamination of the signal, also based on a timing residual but with a much larger timing resolution of 60 ns [81].

Branch Optimization Navigating Successive Annealing Iterations (BONSAI) is a more accurate, but slower vertex fitter described in [81]. Beginning from vertices described by four hit combinations for which the timing residual is zero, a maximum likelihood fit is performed on the timing residuals, and the vertex with the highest likelihood is chosen. By beginning from the selected four hit combinations, fitting is much faster and less likely to become stuck at a local maximum. The use of STORE and ClusFit prior to BONSAI in the WIT online system is motivated by speed considerations, as the data rate is large.

4.9.2 Direction Reconstruction

Direction reconstruction is described in [2]. An energy dependent likelihood was constructed using MC, for angles between the momentum direction of an electron and the PMT hits its Cherenkov photons produce. The total likelihood for all hits in an event is maximised to get the most likely direction. A circular Kolmogorov-Smirnov test on the azimuthal symmetry of the Cherenkov cone around the reconstructed direction is applied [81]; the result is referred to as *dirks*. Figure 4.8 shows the relationship between angular resolution and electron true total energy.

As much of the low energy background in SK comes from radioactive decays in the PMT glass, requiring events not to reconstruct on or near PMTs reduces the background. However, many events close to the PMTs are not well fit, and so reconstruct closer to the centre of the detector. Many of these events can be rejected due to their low vertex goodness or dirks

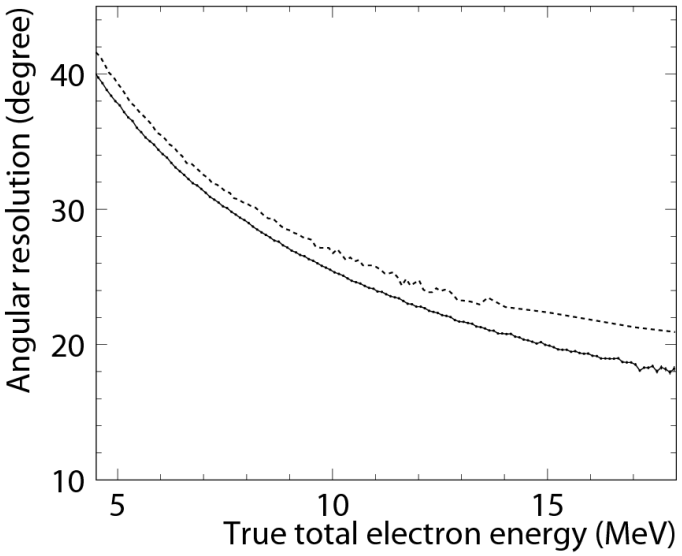


Figure 4.8: Angular resolution of SK against electron true total energy, evaluated with SKDETSIM. The solid line shows SK-III, the dashed line SK-I. Reproduced from [70].

score.

4.9.3 Energy Reconstruction

Energy reconstruction is described in [2, 70]. As the energy of a charged particle is proportional to the number of Cherenkov photons emitted, reconstructed energy is calculated from the number of PMT hits within a 50 ns $T_{residual}$ window, called N_{50}. Corrections are applied, using hits outside this time window to account for light that arrives late because of scattering and reflection, further corrections account for variations in water transparency and dark noise. This corrected number of hits is called N_{eff}. N_{eff} is converted to an energy in MeV using a polynomial function fit to MC simulations of mono-energetic electrons. Figure 4.9 shows the energy resolution as a function of true total electron energy, calculated by SKDETSIM for the SK-III

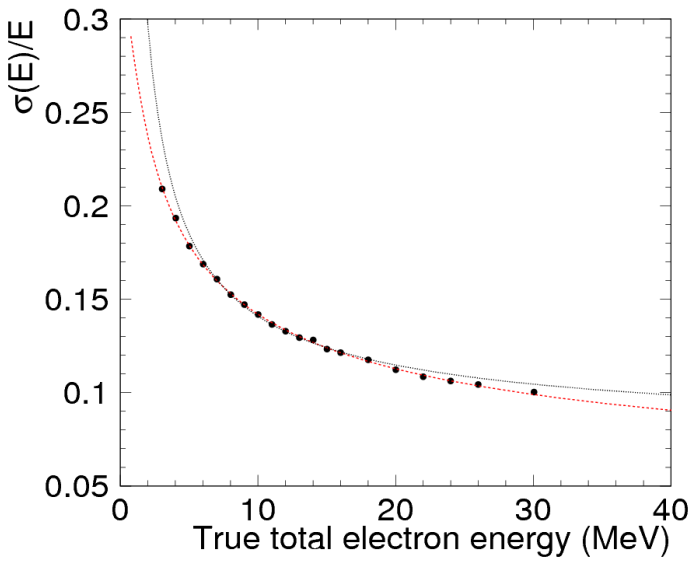


Figure 4.9: Energy resolution used in SK-III solar neutrino study. Black points show one standard deviation for electron MC. **Red** shows a polynomial fit to those points. Black line shows the equivalent used for SK-I. Reproduced from [2].

solar neutrino analysis.

The number of on-time hits called *n18* is the number of hits with $-6\ ns < T_{resid} < 18\ ns$ at the reconstructed vertex. The variable *fromwall* refers to the distance from the reconstructed vertex to the wall of the detector by the shortest vector. The same distance but along a vector defined by the reconstructed direction is called *effwall*, and is useful as events from the detector wall which mis-reconstruct further into the detector will often have a reconstructed direction pointing towards the nearest wall.

4.9.4 Isotropy Parameters

As in most cases, thermal neutron capture (TNC) on Gd will result in multiple γ-rays with what are assumed to be random directions relative to each

other, the pattern of PMT hits in SK should be quite isotropic. Multiple Cherenkov rings from Compton scattered electrons may or may not overlap, and due to the low energies involved, the rings may not be distinguishable at all.

Therefore, an effective way to select TNC on Gd against backgrounds, say from single γ or β rays, would be based on this hit pattern. The direction KS test, described in section 4.9 could be included in this category. The following variables were considered which are not widely used in SK at the time of writing.

Following the approach taken in [82], the parameters β_l are defined in equation 4.3. A vector is traced from the event vertex to each PMT which is hit in an event. The angle between each pair of vectors i and j is θ_{ij}. The parameter β_l is simply the average of the Legendre polynomial of $\cos(\theta_{ij})$, where l is the order of the Legendre polynomial. A higher value of β_l indicates a less isotropic event.

$$\beta_l = \frac{2}{N(N-1)} \sum_{i=1}^{N-1} \sum_{j=i+1}^{N} P_l(\cos\theta_{ij}) \tag{4.3}$$

β_1 and *pclose* are not widely used in SK at the moment, and the implementation had to be written from scratch. As shown by Figure 4.10, many background events occupy can be discriminated from TNC on Gd using reconstructed energy and β_1.

Another use of hit pair angles is to count those with small angles. From inspecting the distribution of some events, a threshold of $cos(\theta_{ij}) > 0.969$ was chosen. Background events appear to be more likely to have hits in the

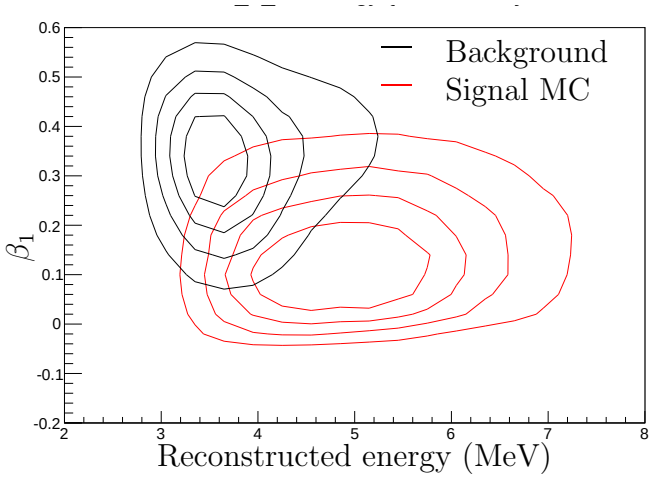


Figure 4.10: Equal quantile contour plots of distributions of β_1 and reconstructed energy, for MC TNC on Gd using the GLG4SIM model. These variables can be used to discriminate much of the background. Events from TNC on Gd have a β_1 close to 0, as they produce a more isotropic hit pattern than background. Much of the background is at low energy.

very forward region. The total number of pairs with small angles will be referred to as *nclose*, and the proportion of hit pairs with small angles as *pclose*.

The reconstructed event vertex and the locations of any three PMTs describes a unique cone, assuming that the hits fall on the surface of the cone, and that the event vertex is the apex of the cone. If the three hits orginate from Cherenkov emission by the same lepton, then the opening angle of this cone should match the Cherenkov angle. Given the vectors connecting the locations of three PMTs that were hit with the reconstructed vertex $\vec{p_{1,2,3}}$, then the angle

$$acos((\vec{p_2} - \vec{p_1}).(\vec{p_3} - \vec{p_1})) \tag{4.4}$$

is the opening angle of the cone. This approach is used in the SK DSNB analysis to separate out the leptons from IBD events from those produced

by backgrounds, especially charged pions from neutral current interactions of atmospheric neutrinos, which have a smaller Cherenkov angle [58].

The extent to which the set of cones are consistent with being from the same multiple scattered electron/positron is the basis of the multiple scattering goodness (MSG) statistic. First, 42° cones are projected from the reconstructed vertex, centred on each on-time hit PMT. For pairs of these cones which intersect twice, the line of intersection is considered as a direction candidate. Direction candidates are then added to clusters if their direction is within 50° of the central event direction of the cluster, found by summing the direction candidate vectors. Clustering goes through several iterations, with direction candidates being reassigned between clusters, to maxmimise the length of the total vector of the largest magnitude vector. The ratio of the largest vector magnitude to the total number of direction candidates is the MSG statistic [70]. A high value means that the direction candidates are consistent with being from Cherenkov emission with small angle scatters. A low value suggests a more isotropic event.

Chapter 5

Gadolinium Loading

In this chapter, discussion of the purpose, effects, and practical requirements of gadolinium loading is made. Firstly, the motivation for Gd loading is given in section 5.1. Radiopurity requirements for gadlinium sulfate powder are explained in section 5.2. Section 5.4 concerns the monitoring of gadolinium concentration, and describes an original study conducted by the author into the use of liquid state atomic absorption spectroscopy for that purpose.

A brief description of EGADS will be given in section 5.3, as EGADS data collected using neutron sources is used as an input to the SK-Gd response model described in chapter 6. A more detailed description of EGADS, including its aims, physical structure, and results, can be found elsewhere [83, 68].

In section 5.5, models of the γ-ray cascade emitted following TNC on Gd are described. The available models are introduced and compared, and the signal made by γ-ray cascades in SK is explored.

5.1 Motivation

The primary motivation of Gd loading at Super-K, as descibed in the original *GADZOOKS!* proposal [61], is the detection of the DSNB (see section 3.5).

The DSNB is the continuous flux of neutrinos produced in all previous SNe in the universe. SK sets the best limits on the DSNB, but is background limited [58, 57]. Although the DSNB contains all neutrino flavours, detection is only possible at SK for $\overline{\nu}_e$ through the IBD on H, as cross sections for other interactions are much lower (see Figure 2.1). In published analyses, some sources of background are reduced by requiring delayed coincidence events between a the IBD positron and the 2.2 MeV γ-ray from TNC on H [57, 84].

However, detection of 2.2 MeV γ-rays at SK has low efficiency, as a Compton scattered electron from a 2.2 MeV γ-ray is often close to or below the Cherenkov threshold, and so produces only a small number of photons, if any. Detection is enabled by the AFT trigger, and careful selection of single γ-ray-like events [60].

Gd has a very high neutron capture cross section (see Table 5.2), so only a relatively small amount needs to be added to SK for the majority of TNC to be on Gd (see Figure 5.1). Loading pure water to 0.01% Gd by mass will cause approximately 50% of TNC to be on Gd; at 0.1% Gd loading this increases to 90%. This translates to approximately 0.02% and 0.2% gadolinium sulfate by mass respectively. SK will first be loaded to 0.02%, going to 0.2% at a later stage.

TNC on Gd produces a γ-ray cascade with higher energy, and therefore a much larger number of Cherenkov photons than TNC on H; it can be detected

more efficiently and with lower background. By adding Gd to Super-K, the DSNB could be positively detected within a few years [61].

A similar approach was taken in SNO: sodium chloride was used to increase the visibility of neutrons through TNC on chlorine nuclei [85]. However, this would not be feasible for SK. SNO was composed of heavy water (D_2O). The neutron capture cross section for deuterium is 5×10^{-4} barns, compared with 0.33 barns for hydrogen. The neutron capture cross sections for chlorine is 30 barns, and Gd 5×10^5 barns. Hydrogen competes much more strongly for a share of neutron captures than deuterium, so chlorine would capture a much smaller proportion of neutrons in a light water detector. Furthermore, a sodium chloride solution of sufficient concentration would accelerate rusting and degradation of detector materials; SNO had an acrylic vessel separating the PMT support structure from the salted water, whereas SK does not.

Other analyses can also benefit from efficient detection of neutrons. If SN neutrinos were detected at SK, 88% of detected events would be IBD on H, but all the useful directional information is carried by events from elastic scattering on electrons, comprising just 3% of events (see Figure 2.1) [33, 39]. By removing the IBD events, the solid angle region to be searched for the SN would be reduced by a factor of four for a galactic supernova, assuming 0.2% gadolinium sulfate loading [68]. Other proposed benefits include better $\nu/\overline{\nu}$ separation in atmospheric neutrino studies, and reduced background rates for proton decay studies [68].

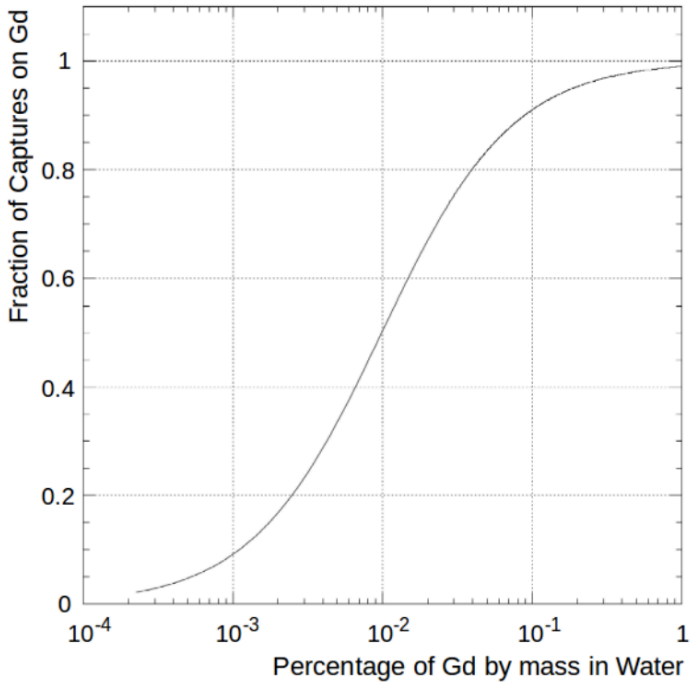


Figure 5.1: Proportion of TNC which are on gadolinium against the proportion of gadolinium by mass dissolved in water. Reproduced from [68].

5.2 Radiopurity

The majority of low energy background at SK is from radioactive decays, either in the materials of the detector structure, surface contamination deposited during construction, PMT glass, and FRP PMT covers, or material dissolved in the detector water. Therefore, the sources of these backgrounds are concentrated at the edges and bottom of the detector volume. Vertices at the edge of the detector are often poorly reconstructed and so bleed into the FV. Background rates at low energy coming from radon and internal radioisotope contamination are partially mitigated by preventing convection through temperature control, and disregarding events close to the detector wall [69, 73]. Contamination of uranium (U), thorium (Th), and actinium (Ac) chain isotopes which produce γ-rays or β-rays, introduced by the addition of gadolinium sulfate, will be distributed uniformly through the detector, and so increase the low energy background rate even inside the reduced FV. Figure 5.2, Figure 5.3, and Figure 5.4 show the decay chains for which activity targets were set.

Estimates were produced, using MC, of the amount of background that would be produced by the introduction of U/Th/Ac chain isotopes [88]. Acceptable levels of contamination for existing low energy analyses were quantified. Using hyper-pure germanium (HPGe) detectors, the U/Th/Ac chain contamination of samples of gadolinium sulfate were measured. Initially, 'off-the-shelf' supplies of gadolinium sulfate were found to have unacceptably high contamination. Feedback on the radiopurity of samples was given to chemical supply companies, who were able to improve their processess,

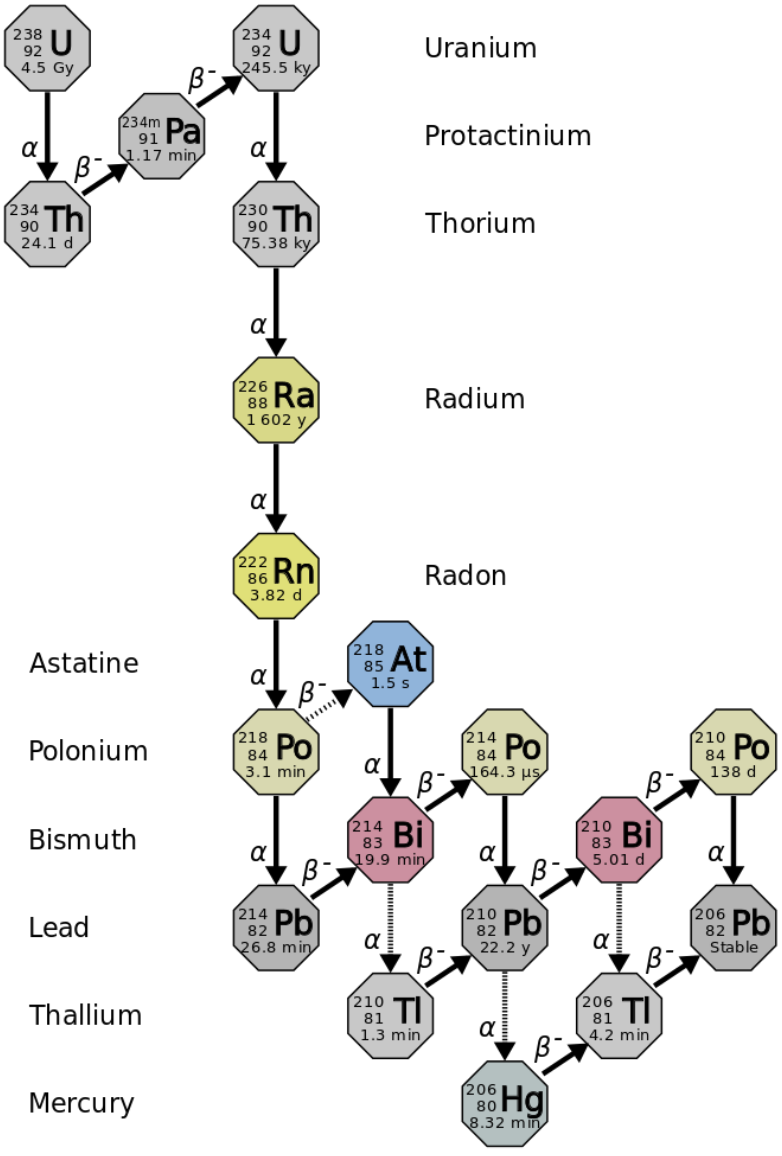


Figure 5.2: Decay chain of Uranium-238. Used under license [86].

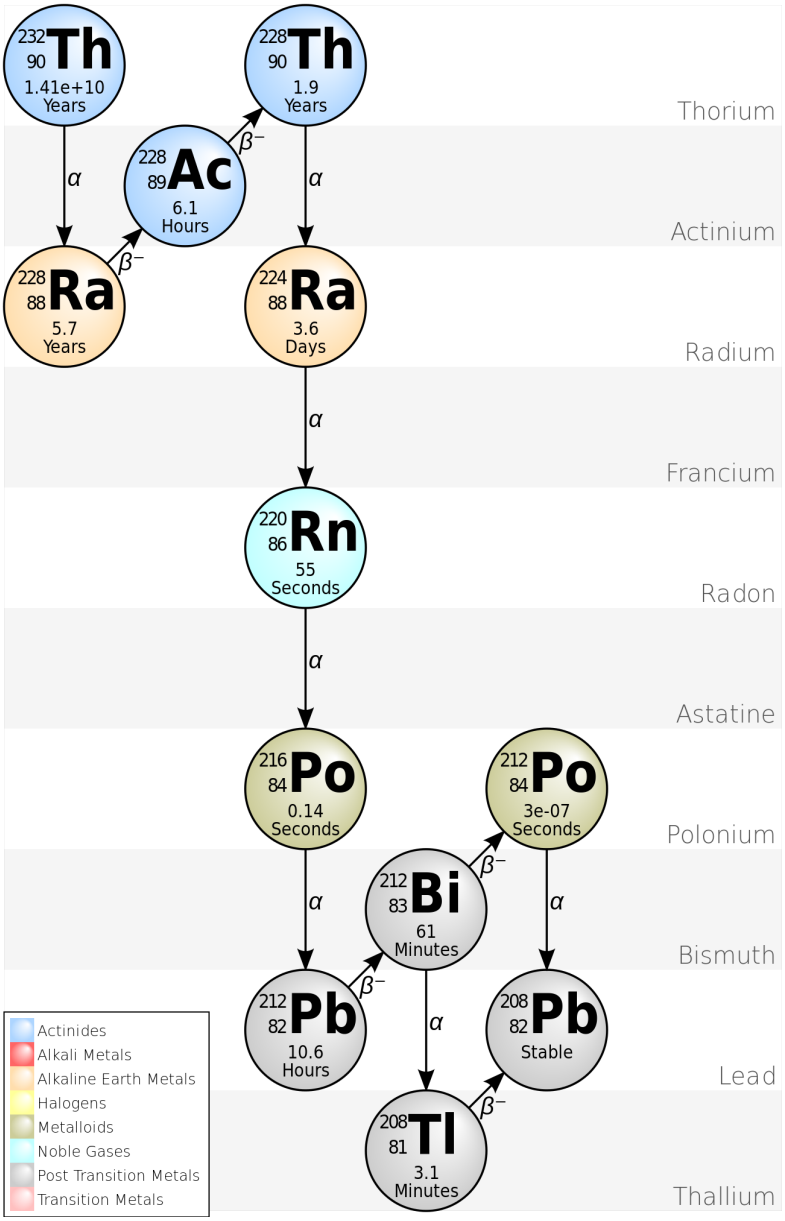


Figure 5.3: Decay chain of Thorium-232. Used under license [87].

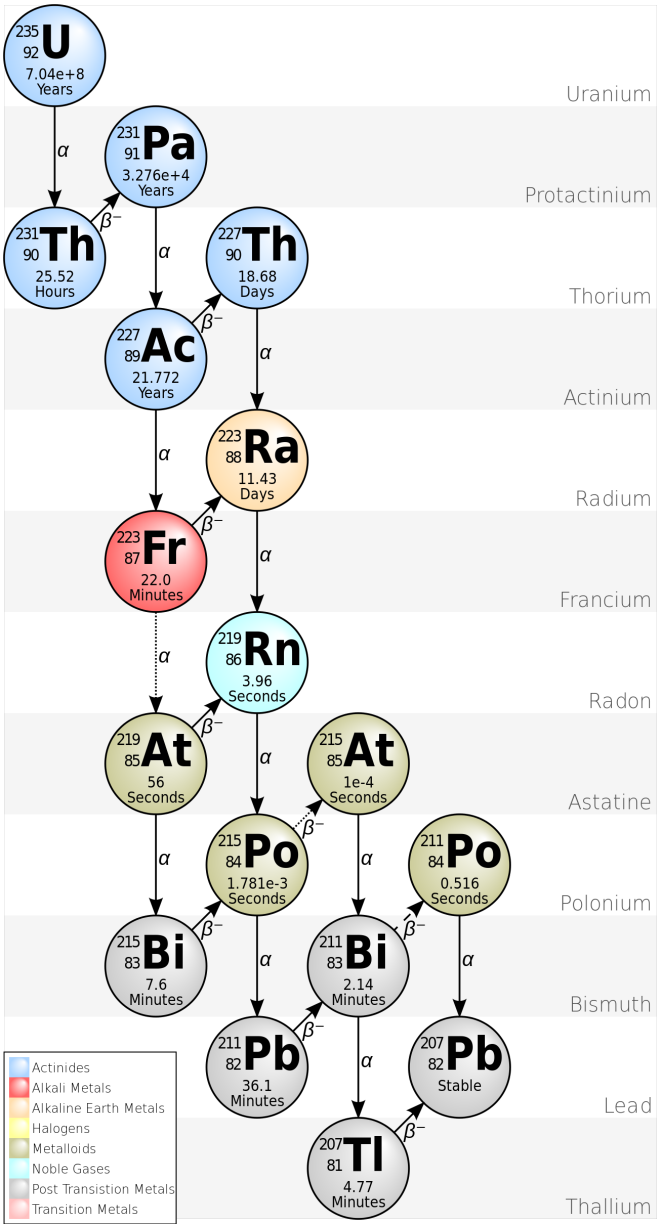


Figure 5.4: Decay chain of Actinium-227/Uranium-235. Used under license [87].

Chain	Measured isotope	Typical	Specification
^{238}U	^{238}U	50	<5
	^{226}Ra	5	<0.5
^{232}Th	^{232}Th	10	< 0.05
	^{228}Th	100	<0.05
^{235}U	^{235}U	32	<3
	^{227}Ac/^{227}Th	300	< 3

Table 5.1: Target activity levels in mBq per kg of gadolinium sulfate from various isotopes. Typical values are given for gadolinium sulfate purchased 'off the shelf'. Table published in [68].

and so radiopurity was brought to acceptable levels [68]. Table 5.1 shows the target levels of contamination.

The specified activity levels in Table 5.1 were mainly determined by the requirements of the solar neutrino analysis. Those isotopes in the chain decaying by β decay could increase background rates for the solar neutrino analysis by producing events in the energy range of interest. The energy spectra of the different isotopes were considered with the response of the detector in order to determine how much background would be added. Of most interest due to their relatively high β decay energies were the β decays of ^{208}Tl peaking at 5.0 MeV from the Th chain, ^{214}Bi at 3.27 MeV from the U chain, and ^{212}Bi at 2.25 MeV from the Th chain [68, 88]. The existing intrinsic background probably originates from these decays, although it cannot be shown conclusively due to insufficient resolution at these energies. Specifications were set such that the added background rate would be no larger than the existing background. The only exception was the ^{238}U specification, which was set by the DSNB analysis, as spontaneous fission (SF) can create a background featuring delayed coincidences. Further discussion

of delayed coincidence backgrounds from these isotopes appears in chapter 6. Potassium-40 is likely also present in SK, and may contribute to dark noise rates; but the decay Q-value is not high enough for single decays to create background events over threshold.

5.3 EGADS

In order to have gadolinium sulfate dissolved in the water of SK, it was necessary to develop new water systems. SK-IV water systems remove ions from the water, including the Gd^{3+} and SO_4^{2-} ions from the gadolinium sulfate (see section 4.4).

Development began at the University of California, Irvine, of a small water system that could selectively keep these ions in solution, and devices to actively and precisely monitor water transparency to Cherenkov light. In SK, water transparency is monitored using Michel electrons [69], which is not possible in a water system not connected to a large water Cherenkov detector. Materials present in SK were soaked in the Gd loaded water to test if there would be interactions leading to a major degradation in water quality.

A degradation in water quality would lead to fewer Cherenkov photons being detected, which could negatively impact other SK analyses. Furthermore, it had to be demonstrated that the addition of gadolinium sulfate would not negatively impact other analyses through the introduction of additional backgrounds, by increased levels of decay chain isotopes or from neutron captures directly. Water quality at EGADS is automatically monitored

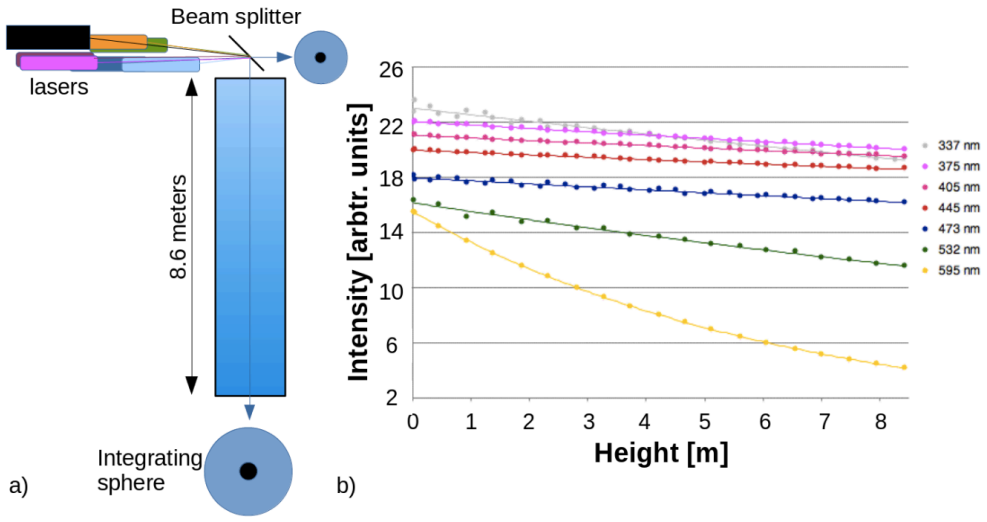


Figure 5.5: Schematic of the UDEAL system for automatic water transparency measurements. Reproduced from [68].

by the UDEAL system, a schematic of which is shown in Figure 5.5. IDEAL (Irvine Device Evaluating Attenuation Length) is a prototype of UDEAL in the water system at Irvine; it is slightly smaller and less automated. UDEAL and IDEAL measure the absorption of a water sample at 7 wavelengths in a vertical tube. The measurements are taken with varying water depth to control for laser and photodiode response. The results can be weighted by the detected spectrum of Cherenkov photons in SK in order to estimate the proportion of Cherenkov photons that would travel 15 m. This distance was determined, using MC, to be the average distance a Cherenkov photon travels before detection in the SK ID.

This water system was tested on a larger scale by the EGADS experiment at Kamioka. This was intended as a small prototype of SK-Gd, so included a functioning 200 ton water Cherenkov detector, built from the same material and components as SK as much as possible. More than being a large, long term soak-test of materials and components, EGADS demonstrated that high water quality could be maintained without loss of Gd, as can be seen in Figure 4.5.

It was decided that Gd loaded water could not be discharged directly to the drain, so consideration had to be made for how to remove it from solution. This was acheived with specialised ion exchange resins, and was demonstrated when EGADS was drained.

EGADS is, like SK, a water-Cherenkov (WC) detector: 20-inch PMTs face a volume of water to detect Cherenkov light. However, EGADS is only 200 tons, compared to the 50 kt of SK, and does not have any outer detector. PMTs are mounted on a stainless steel support structure inside a stainless steel tank, as shown in Figure 5.6 and Figure 5.7.

In EGADS, 227 PMTs are installed, 76 of which are covered by the FRP cases used in SK. Most PMTs are the same as those used in SK, but a few are newer technologies being tested for Hyper-K. The same black sheet as SK fills the spaces between the PMTs. The PMT photocathode coverage is 40%, the same as SK, as the same sized PMTs are mounted with the same pitch. A magnetic field compensation coil is included as in SK.

The small volume of EGADS means that it would mostly be useful for neutrino detection in the case of a galactic SN, as the rate of events from all other sources is small. Because the size of each PMT is quite large compared

to the whole detector, the vertex reconstruction resolution for TNC on Gd is also large, so effectively any event within the inner volume can be in spatial coincidence.

The reconstruction tools used in EGADS are the same as those used in SK, described in chapter 4, with changes made to the geometry.

The DAQ is the same as that used in SK. Initially ATMs were used, with a later upgrade to QBEE. These electronics are described in section 4.5. More information about EGADS can be found in [83, 68]. Water systems are covered in section 4.4.

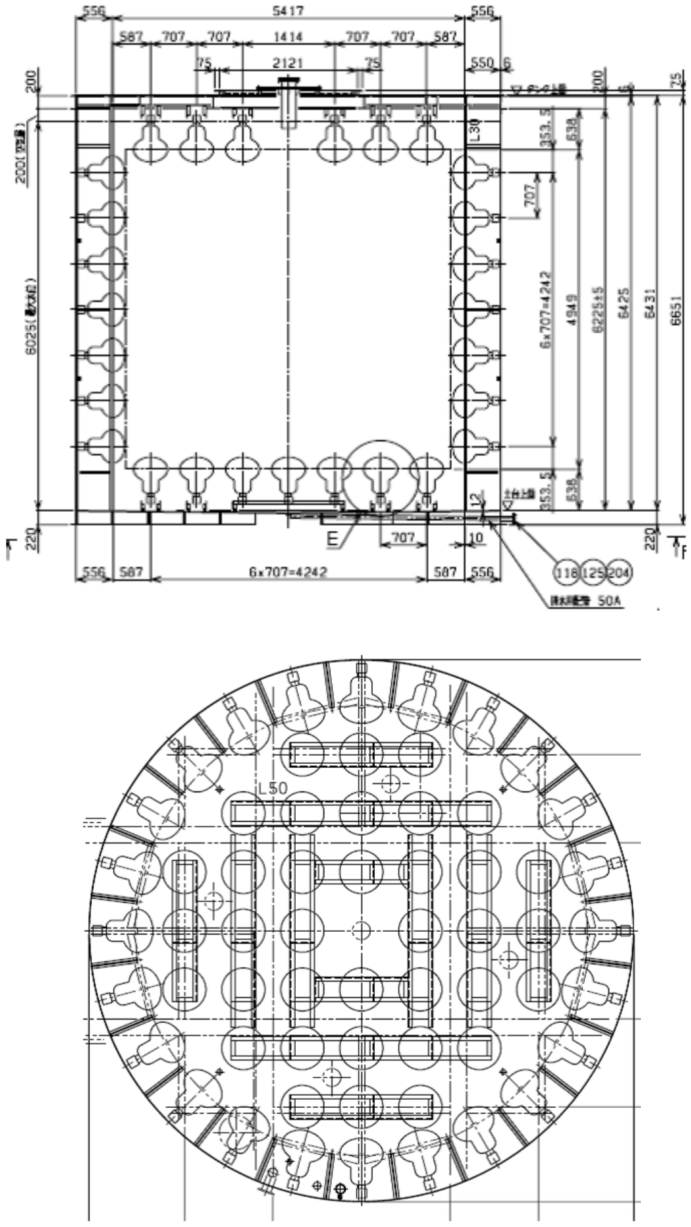


Figure 5.6: Extract from technical drawings of EGADS. Reproduced from [83].

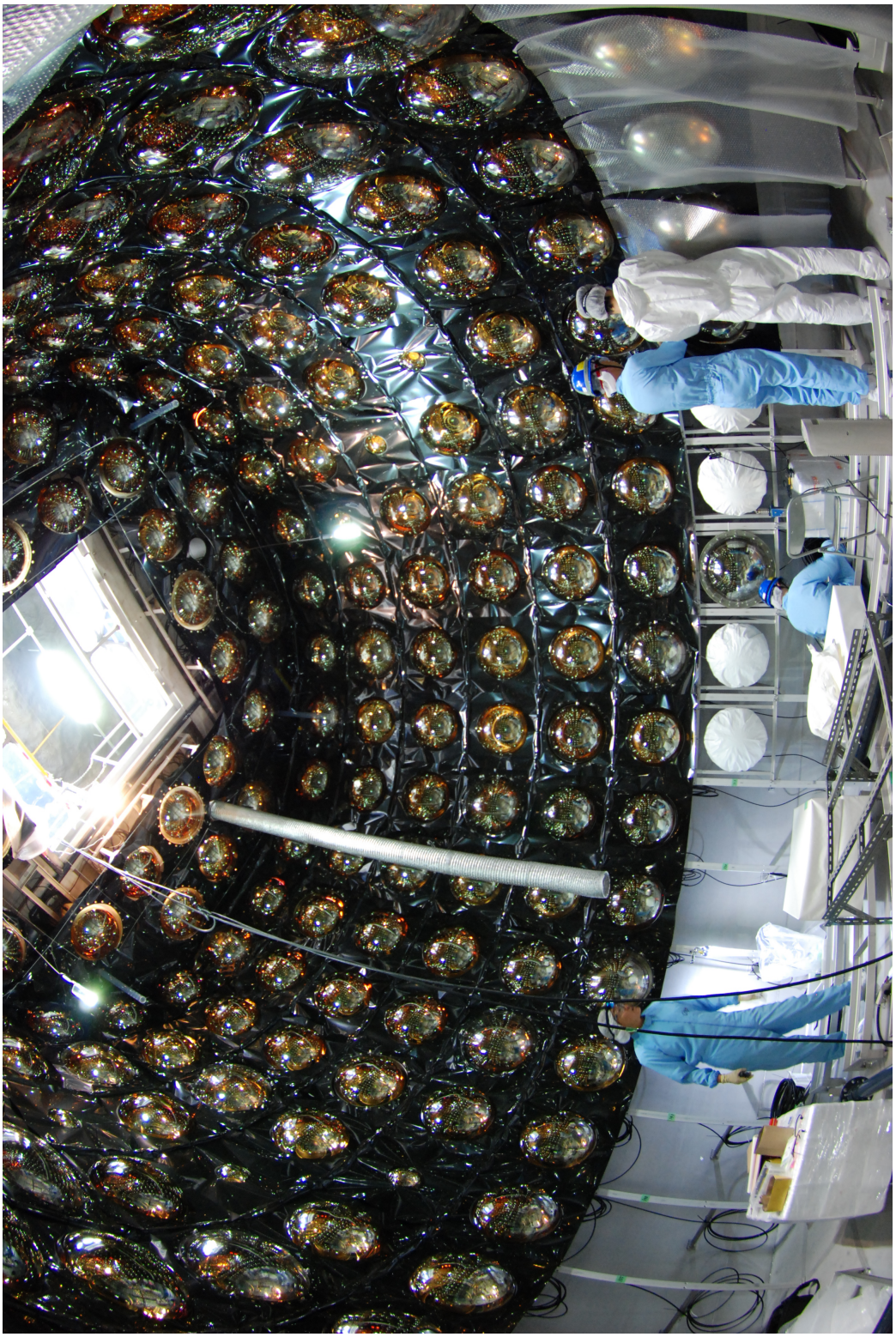


Figure 5.7: Photograph of PMTs being mounted in EGADS. Photo courtesy of Mark Vagins.

5.4 Monitoring Gd Concentration

Several methods have been used to monitor Gd concentration in EGADS. This is necessary in order to ensure that Gd concentration is stable, that is, Gd is not being lost through leaks or flaws in the water treatment process. As SK is so large, and water flow in the detector slow and laminar, it is necessary to test that Gd concentration is uniform throughout the detector; this will be measured by testing the neutron capture efficiency with moveable neutron calibration sources (^{252}Cf or americium-beryllium (AmBe) neutron sources) and by sampling water using long capillary tubes.

In order to measure the Gd concentration, the optical absorption of a sample is tested at specific wavelengths[1]. This can be done with the sample remaining in a liquid state (liquid absorption spectroscopy), or first being atomised (atomic absorption spectroscopy (AAS)). EGADS has mostly used AAS, but spectroscopy in the liquid state would allow for continuous and automated monitoring by passing samples through a flow cell, in which UV absorption is continuously monitored. The feasibility of this method was demonstrated. Later work has demonstrated that this method can be faster and more accurate than AAS.

Using a 1 cm cuvette in a standard laboratory spectrophotometer (see Figure 5.8), UV absorption was measured at ∼305 nm and ∼311 nm wavelength. A sample of gadolinium sulfate loaded water was taken from EGADS, its absorption measured, and was progressively diluted and re-tested. The spectra are shown in Figure 5.9. The UV source was a deuterium lamp, the

[1]Note that the absorption lines used for monitoring Gd concentration are in the far UV, so will not affect SK's ability to detect Cherenkov light.

response of which varied somewhat over the period of data collection. This could be corrected for by subtracting some baseline value from the spectrum, or using the difference of the two peaks rather than the absolute. Absorption is described by the Beer-Lambert law:

$$A := log_{10}\frac{I_0}{I} = \epsilon c l, \tag{5.1}$$

where A is the absorption, defined by the logarithm of the factor of reduction in intensity I against a reference I_0, ϵ is absorptivity of the attenuating species, l the length of the absorption cell, and c the concentration. The difference between A for two peaks caused by the same attenuating species

$$A_1 - A_2 = lc(\epsilon_1 - \epsilon_2), \tag{5.2}$$

is proportional to c; l, ϵ_1, and ϵ_2 are fixed. The measurement errors on A_1 and A_2 are correlated, as a large part comes from the drift of the response of the spectrophotometer, and the peaks are measured in quick succession: therefore much of the measurement error cancels when the difference is taken. Rather than measuring l and ϵ directly, measurements are taken with known reference concentrations to produce a calibration curve, leading to

$$\frac{A_1' - A_2'}{A_1 - A_2} \times c = c'. \tag{5.3}$$

The relationship between absorption and concentration was clear (shown in Figure 5.10), and it was estimated that such a piece of equipment would be able to measure the concentration of Gd in nominally 0.2% gadolinium

sulfate loaded water at better than 5% accuracy. This has been further developed by another student into a working prototype for automatic continuous monitoring.

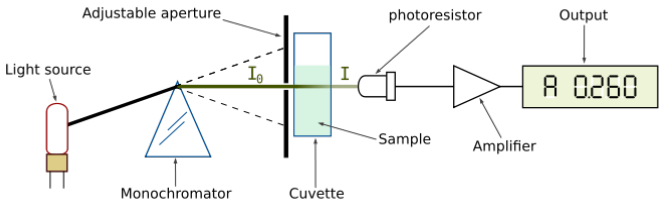


Figure 5.8: Schematic diagram of a single beam spectrophotometer. Used under license [89].

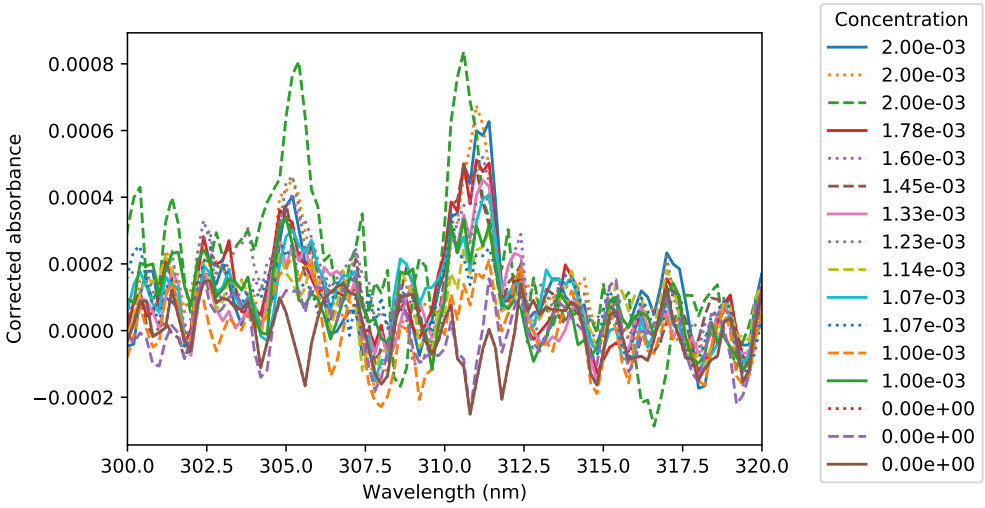
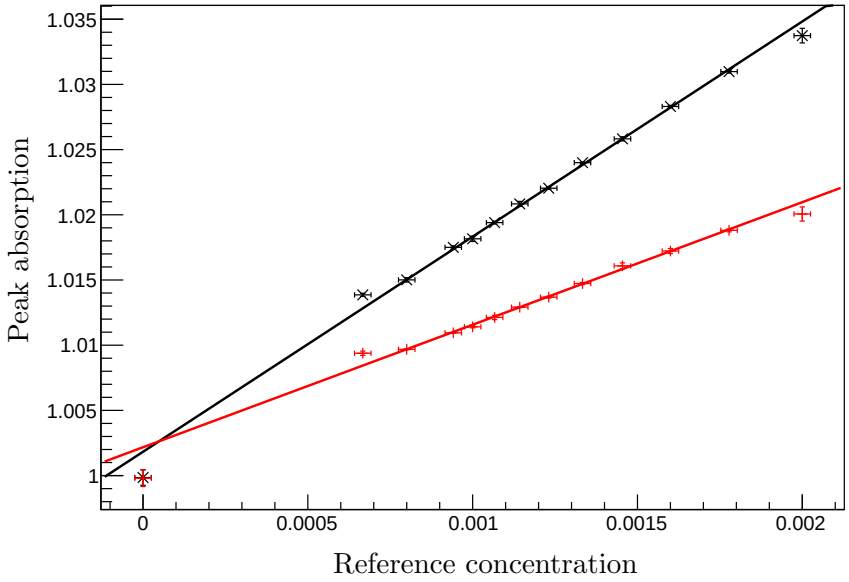
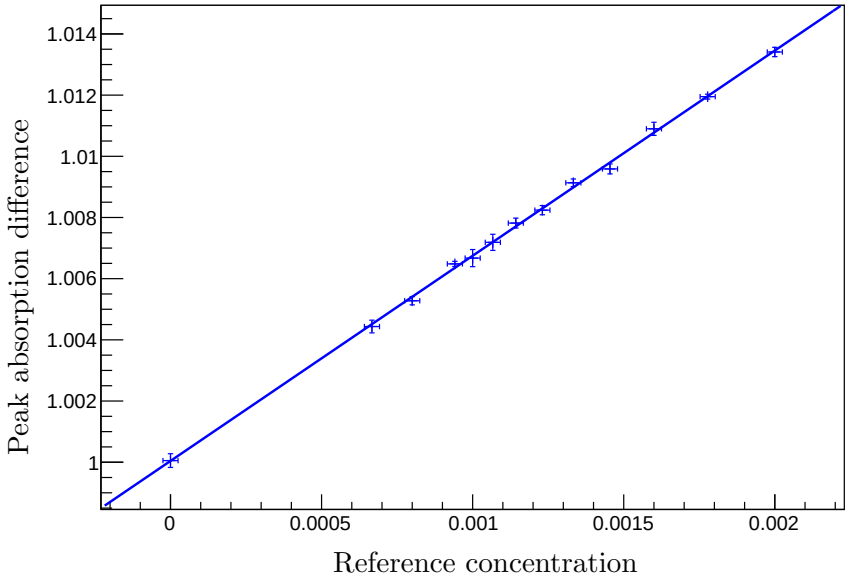


Figure 5.9: Drift-corrected UV-absorption spectra of gadolinium sulfate solution at varied dilution. The strength of the absorption increases with concentration.



(a)



(b)

Figure 5.10: UV absorption of gadolinium sulfate against dilution. In (a) the absolute absorption is plotted for the two lines, using a linear correction for drift. In (b) the difference of the two is plotted. Using the difference has the advantage of cancelling some uncertainties, and so leads to a better fit.

5.5 Simulation Studies on the Characteristics of Emitted γ-rays

Thermal neutron capture on Gd is followed by a γ-ray cascade with a total energy around 8 MeV (7.9 MeV or 8.5 MeV depending on the isotope). The isotopes contributing most to Gd capture are ^{157}Gd and ^{155}Gd, with properties listed in Table 5.2.

Isotope	Abundance	TNC cross section	Q (MeV)	Type
^{157}Gd	15.65%	255 kbarn	7.9	γ-ray cascade
^{155}Gd	14.80%	61 kbarn	8.5	γ-ray cascade
^{1}H		0.3 barn	2.2	single γ-ray

Table 5.2: Abundance, decay energy and TNC cross sections of Gd isotopes and H [68].

As γ-rays produce a signal in SK mainly by Compton scattering electrons, which then produce the Cherenkov photons which are detected, the total visible energy recorded for each γ-ray cascade will depend on how many γ-rays are produced, and how the energy is divided between them.

Using a very simple Monte Carlo, 8 MeV was divided equally between 1 to 4 γ-rays. Each γ-ray was scattered (according to the Klein-Nishina formula) until it had an energy below 0.3 MeV. The energy, less the Cherenkov threshold, was summed over all scattered electrons, and this was assumed to be the visible energy deposition.

Under these simplifying assumptions, the visible energy is controlled by the multiplicity, with a clear relationship. In reality, energy is not equally divided between the γ-rays in the cascade. Because of threshold effects, making the distribution of the energy between the γ-rays unequal will tend

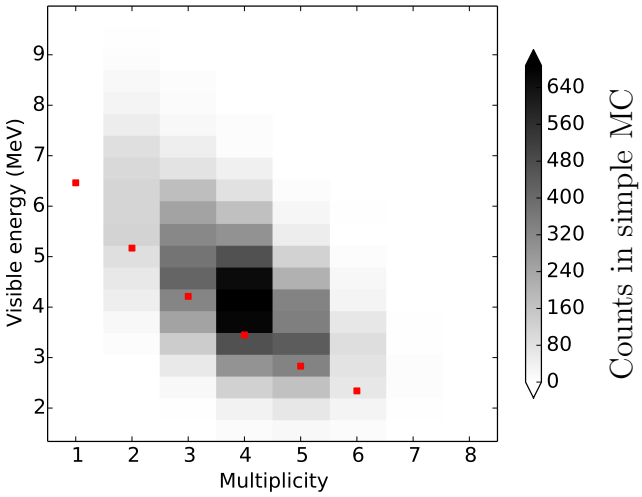


Figure 5.11: The results of simple MC assuming accounting only for Compton scattering and assuming equipartition of energy between γ-rays (red points), compared with a full MC treatment in SKDETSIM with the GLG4SIM γ-ray emission model (color map).

to increase the visible energy in this case, explaining the systematic offset. There will be further broadening of the reconstructed spectrum due to the statistical fluctuations of Cherenkov photon detection. The results of this simple MC are shown in Figure 5.11, compared to a full MC treatment in SKDETSIM with the GLG4SIM γ-ray emission model. In the simple MC, 10^5 events were generated for each multiplicity, for the full treatment 10^5 were generated in total. The comparison of the simple MC and the full MC shows that the division of energy between the γ-rays, followed by Compton scattering, accounts for the general behaviour of the relationship between γ-ray multiplicity and visible energy.

Watanabe et al. [90] deployed an acrylic vessel containing Gd-loaded water and a neutron source in SK. The sample size of this study was small,

and the data were taken with the old SK DAQ. The observed reconstructed energy spectrum is shown in Figure 5.12. The energy spectrum was observed to peak at $4.3 \pm 0.1\ MeV$. In the Watanabe et al. study, the TNC model used was that of GEANT4.7.1.p01, which reproduced the data well within the uncertainties, despite any criticisms that might be made about the detailed accuracy of the model. The acrylic vessel is large and creates a shadow and other optical effects, which were accounted for in MC.

The overall spectrum of γ-rays from thermal neutron capture on Gd is fairly well measured in spectrometer experiments. What is less well determined is which γ-rays come together in fine detail, as this requires the measurement of multiple γ-rays in coincidence, which is experimentally challenging. Also unclear is the angular distribution of the γ-rays relative to each other: even if the reconstructed energy distribution closely matches between simulation and reality, it is desirable that the spatial distribution of hits in the detector is accurate as this will also be used for selection. The models considered do not contain angular correlations; each emission is assumed to be isotropically random and independent.

The spectrum of γ-rays from thermal neutron capture on Gd consists of a few known energy γ-rays close to the Q-value, and a continuum at lower energies where the levels are so densely populated that they are indistinguishable. In fact, an approximate, parametric model is the only option to represent the densely populated continuum. These models are based upon the assumption that the γ-ray emission occurs as electric dipole transitions in the low energy tail of the well measured giant dipole resonance. This can be used to produce a probability distribution, differential in both the energy

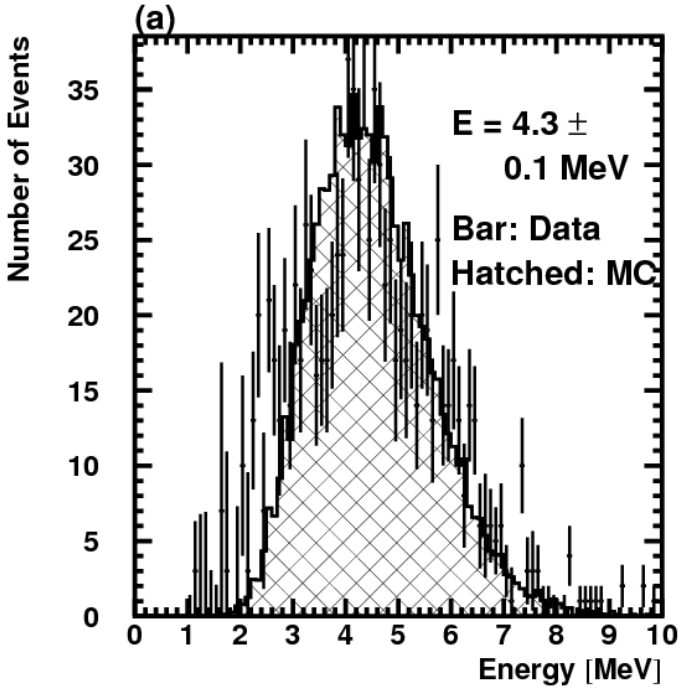
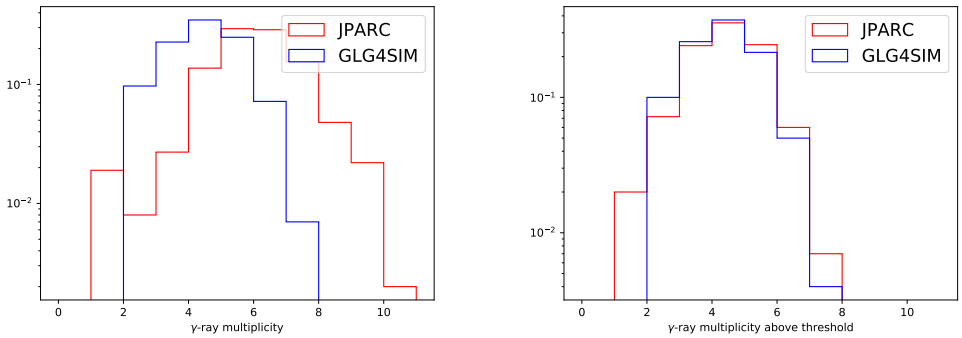


Figure 5.12: TNC on Gd energy spectrum observed in SK with Gd loaded neutron source vessel by Watanabe et al. [90].

of the γ-ray and the remaining energy of the excited nucleus; the γ-rays can then be generated sequentially using the MC method until no excitation energy remains.

An accurate model of the underlying nuclear physics is not available; both theoretical and experimental treatment is challenging (see e.g. [91]). Furthermore, due to the γ-rays having energies relatively low for SK, and therefore a small number of detected photons and poor reconstruction resolution, these differences in underlying physics will be smeared out. Individual γ-rays within a cascade will not be resolved.

The SK detector simulation is based on GEANT3, which does not simulate TNC on Gd by default. GEANT4 [92, 93] contains a number of generic models, but they do not contain those known high energy γ-rays. Generation of γ-rays in the older versions of GEANT4 did not conserve energy; this is fixed in later versions, but correlations in energy between γ-rays in a cascade are not accounted for even in the latest version (at the time of writing GEANT v4.10.6). For the GLG4SIM generic liquid scintillator simulator, another model was developed ([94]), which combined a parametric model of the continuum with the known high energy γ-rays. Recent efforts at J-PARC [95, 96, 97, 98] have used new measurements to account for what combinations of γ-rays come together, and have provided another model including this and a different continuum distribution. The known high energy γ-rays are rare, and the majority of events are in the continuum. It is assumed by all known models that the angles of γ-ray emission are isotropically distributed; it is possible this is not the case, but if any angular correlations are strong enough to have a large effect on selection, then they will be seen using in-situ



(a) All (b) $E_\gamma > threshold$

Figure 5.13: Multiplicity of γ-rays in emission models. The model provided by J-PARC produces more low energy γ-rays which cannot scatter electrons with enough energy to put them above Cherenkov threshold.

neutron source calibration data.

The measurements at J-PARC used a neutron source and an array of germanium detectors to measure the γ-ray spectrum from TNC on Gd, which were compared with a GEANT4 simulation using an updated model of the contiuum emission spectrum. Although better than the GEANT4 (v4.9.6) default, differences between simulation and spectrometer data were $^{+50\%}_{-30\%}$ [95].

It is worth examining the differences between these models and determining the extent to which SK is sensitive to them.

The multiplicity and energy distribution of emitted γ-rays in the J-PARC and GLG4SIM models are shown in Figure 5.13 and Figure 5.14. The J-PARC model appears to have a higher multiplicity, but considering only those γ-rays with enough energy to Compton scatter an electron to above its Cherenkov threshold ($E_\gamma > 0.54\ MeV$), the two models appear more similar, although differences are still visible.

The GLG4SIM and J-PARC γ-ray emission models are compared in re-

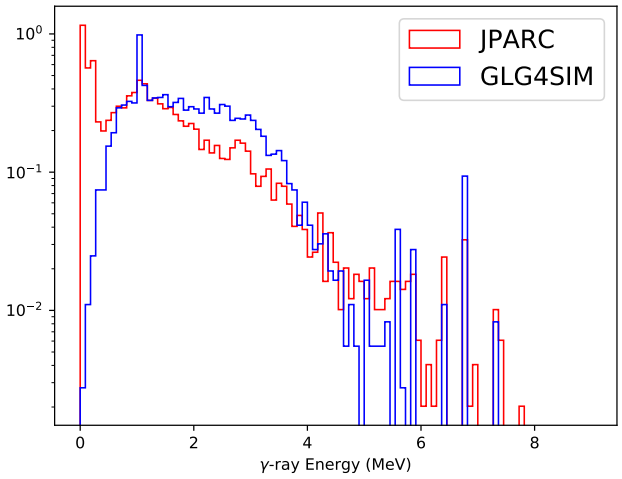
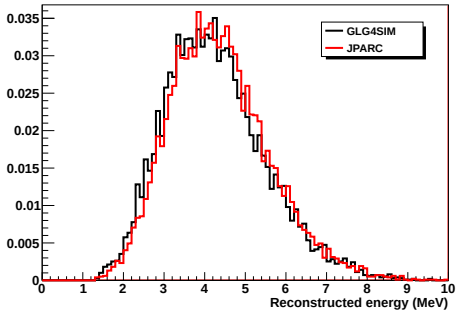


Figure 5.14: Emission energies in γ-ray emission models.

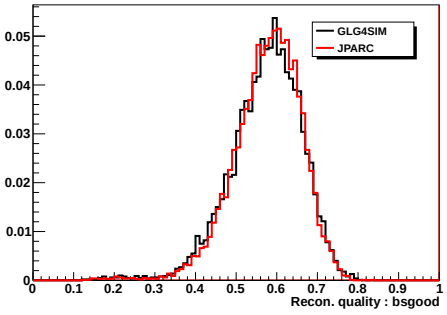
constructed variables in Table 5.3 and Figure 5.15. Separation parameter values (defined later in Equation 7.4) between the models are very low, showing that the distributions are very similar. Differences in the reconstructed variables could likely be resolved in-situ because very high statistics would be available for data collected with a neutron source; models could then be calibrated or remade to maximise agreement. In order to quantify the extent to which the differences between the models matter, both models are included in the pre-SN neutrino study in order to provide a systematic uncertainty on the efficiency of detection of TNC on Gd. In-situ neutron source measurements will resolve these issues once SK is Gd loaded.

Variable	Model	Mean	RMS	Separability
bsenergy	GLG4SIM	4.2603	1.2402	
	JPARC	4.3698	1.2193	0.0062
bsgood	GLG4SIM	0.5727	0.0884	
	JPARC	0.5765	0.0831	0.0053
Beta 1	GLG4SIM	0.1759	0.1354	
	JPARC	0.1571	0.1288	0.0112

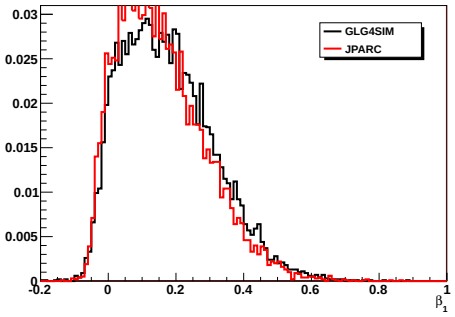
Table 5.3: Comparison in some reconstruction and isotropy variables between TNC on Gd γ-ray emission models. Separability is defined in Equation 7.4, other variables are defined in section 4.9 and subsection 4.9.4. Differences are at a similar scale across other variables that have been omitted.



(a) Recon. energy



(b) Recon. goodness



(c) β_1 isotropy

Figure 5.15: Comparison in some reconstruction and isotropy variables between TNC on Gd γ-ray emission models. Variables are defined in section 4.9 and subsection 4.9.4.

5.6 Measurements in EGADS

That TNC on Gd can be detected in a WC detector has been demonstrated by EGADS using neutron sources.

In an AmBe source, Am-241 decays by α emission. Be-9 then captures the α and decays

$$^{9}Be +^{4}_{2} \alpha \rightarrow^{12} C +^{1} n + \gamma(4.44\ MeV).$$

The 4.44 MeV γ-ray can be used to produce a prompt trigger, analogous to the prompt positron in IBD. The neutron will thermalise and capture as normal. The γ-ray would have a visible energy very similar to that of a γ-ray cascade from TNC on Gd; in order to reduce overlap, a small scintillator crystal can be included with the source when deployed. The 4.44 MeV γ-ray is likely to interact with the scintillator crystal producing many more detectable photons than would be produced by Cherenkov radiation from Compton scattered electrons.

An AmBe source with scintillator crystal was used in SK-IV to validate the efficiency of detecting 2.2 MeV γ-rays from TNC on H, see [60]. γ-rays from TNC on Gd can also enter the scintillator, which forms a background which is accounted for in MC in the study that can found in [83]. AmBe data have been collected many times in EGADS.

The distribution of delayed coincidence (DC) times was assumed to have the form

$$e^{-\frac{t}{\tau_c}}(1 - e^{-\frac{t}{\tau_t}}), \tag{5.4}$$

where τ_t is the time taken for the neutron to thermalise, and τ_c the time for it to capture. This function was fit (plus background) to an americium-beryllium neutron source calibration run in fully (0.2%) Gd-loaded EGADS, with the results $\tau_c = 28 \pm 2$ μs and $\tau_t = 9 \pm 1$ μs (Figure 5.16).

The detected delayed events in the AmBe data samples taken in Gd-loaded EGADS have the expected time and visible energy distributions for TNC on Gd. The difference between the data taken in Gd-loaded and pure-water EGADS periods shows that these events are not simply due to backgrounds from the neutron source. The distributions of reconstructed variables such as reconstructed energy, reconstructed vertex resolution, and isotropy in SK cannot be directly inferred from EGADS due to the differences between the detectors. In-situ measurements in SK should be used once SK is loaded with Gd.

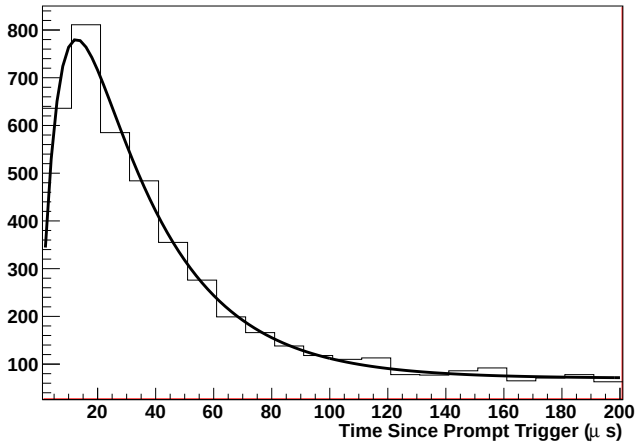


Figure 5.16: Delayed event time distribution for an AmBe run in Gd-loaded EGADS.

5.7 Summary

SK is planned to be loaded with 0.02%, then 0.2%, gadolinium sulfate. This will lead to increased efficiency for the identification of neutrons, decreasing the background to IBD on H. This is because of Gd's TNC capture cross section, and relatively large amount of visible energy produced. The main motivation is the DSNB measurement, but there will be other benefits, including those explored in later chapters of this thesis.

Gadolinium sulfate powder can be contaminated with decay chain isotopes, which could introduce additional backgrounds into SK. This can be controlled at the point of manufacture. The feasibility of gadolinium loading in SK has been demonstrated by EGADS and other studies.

The exact γ-ray spectrum produced following TNC on Gd is difficult to measure. Equally, the differences between available models have only a small effect on reconstructed variables, so will not have a large effect on selection efficiency. These differences could be resolved by in-situ measurements. To account for this, both γ-ray emission models are included in the pre-SN study.

Chapter 6

Detecting Low Energy IBD at SK-Gd

The main channel for detection of $\overline{\nu}_{\mathrm{e}}$ at low energy in SK is IBD on hydrogen ($H(\overline{\nu}_e, e^+)n$), as its cross section is relatively high. The neutron takes a short time to thermalise and capture, and travels only a short distance, meaning that the positron and TNC form a DC, in which two events are reconstructed within a short time and a few metres of each other. The probability of uncorrelated events producing this signature is low, so neutron tagging allows anti-neutrino events to be distinguished from background events, including neutrino events. The high TNC cross section of Gd makes the time between the prompt and delayed parts of the event shorter than with H ($\sim$30 μs vs. $\sim$200 μs), and the higher visible energy improves the vertex reconstruction resolution and detection efficiency. As a result, tagging efficiency for signal will be higher, and accidental backgrounds lower.

In the case of pre-SN neutrinos the energy range of the IBD positron is

below the usual thresholds of SK, in a region that would be overwhelmed by background were it not for neutron tagging. Original studies were performed to understand the performance of SK-Gd in these low energy ranges, which are outside the design parameters of SK, and which had not been thoroughly investigated before.

6.1 Thresholds and Triggering

The most fundamental energy thresholds for SK-Gd are E_ν >1.8 MeV for IBD, and $E_e > 0.8$ MeV total energy for Cherenkov emission by positrons. Positrons above the Cherenkov threshold may not be reconstructed if there are not enough photons detected. Cherenkov photons are lost due to attenuation in the water, the photocathode coverage of the detector, and the quantum and collection efficiencies of the PMTs [67].

In SK, a PMT is considered *hit* if the charge collected by that PMT exceeds a threshold. In order to reduce the data rate from dark noise and radioactivity, a threshold is usually applied to the number of hits in a time window [70]. WIT is an independent trigger system at SK that uses parallel computing to reconstruct very low energy events which do not meet the usual thresholds. It is close to 100% efficient for electrons around 4 MeV total energy within the FV [99] (equivalent to approximately 34 hits). Below this the efficiency drops, as shown by Figure 6.1.

For this study, it was assumed that the prompt and delayed parts of the event had to be independently reconstructed by WIT. This is because at the time of writing, WIT did not contain a coincidence trigger, and the hit

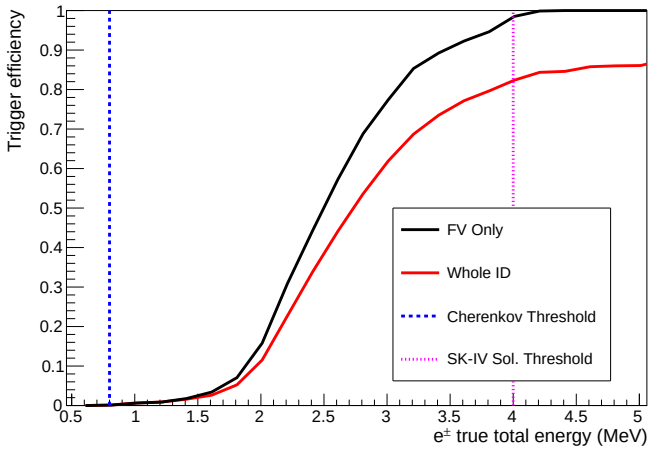


Figure 6.1: WIT efficiency against electron true total energy, evaluated with simulation. Note that true energy is shown, not reconstructed energy. 5000 MC events were generated for each 0.2 MeV true energy bin. The efficiency for events generated in the whole ID is compared to those generated only inside the FV.

data before triggering is applied is not in general kept, making it difficult to ascertain precise accidental background rates. The limitation preventing the total relaxation of trigger conditions (i.e. the saving of all reconstructed event candidates) in WIT is the rate at which data can be organised and written to disk. When putting a pre-SN alarm into practice, a relaxed trigger condition should be applied to coincidences, which would increase signal efficiency and only increase the overall data rate slightly. Simply put, this would work by keeping events which pass a relaxed trigger condition in a memory buffer, and if a later event is found to be in coincidence both would be saved. Therefore, in future the trigger efficiency for low energy IBD events will be higher than that assumed in this study.

6.2 Sources of Background

The background to the single neutron channel is comprised of events from dark noise or radioactive decays with similar characteristics to neutron captures ("fake neutrons"), as well as events which are real neutron captures not from pre-SN neutrinos.

Backgrounds to DC type events include accidental DC between unrelated background events, real DC for certain radioactive decays, and real DC from reactor neutrinos and geoneutrinos.

It is anticipated that rates for intrinsic backgrounds will be known quite precisely once in-situ measurements become possible, but estimates have been made during the planning and development of SK-Gd. In this section, the various sources of background to low energy IBD are discussed, and explanations are given for how the rate of each was estimated.

6.2.1 Intrinsic Background

A large part of the intrinsic background of the SK detector comes from radon emanation from materials inside the detector and radioactive decays within the detector materials; however, this is mainly concentrated at the edges and bottom of the detector [71, 100], and is removed by FV and energy threshold cuts.

Commercially available gadolinium sulfate contains radioactive impurities which will be distributed throughout the detector volume by loading. Much of the work preparing for SK-Gd has been in quantifying these, including with low background counting with HPGe detectors, and working

with manufacturers to reduce the level of contamination such that it does not detrimentally impact other SK analyses [68]. These contaminants are already present at some level in the SK pure water; a basic assumption was that the level must not more than double.

In order to estimate the rate of fake neutrons, events recorded by the WIT system during 6000 hours of normal pure water SK-IV were used. An initial event selection for neutrons was designed to reduce the rate of fake neutrons to a reasonable level, while retaining as much efficiency for simulated neutron capture events as possible.

These data were also used to estimate the accidental DC rate by searching for pairs of events in DC.

6.2.2 Additional Radioactive Decay Backgrounds

The process $^{18}\mathrm{O}(\alpha, \mathrm{n})^{21}\mathrm{Ne}^{*}$, and its equivalent with $^{17}\mathrm{O}$, produce neutrons. There was some concern that this could produce a high rate of neutrons, especially if there were a high contamination of Ac/^{235}U series isotopes that are α emitters. Efforts to reduce radioisotope contamination of gadolinium sulfate have brought this down to an acceptable predicted level. As $^{21}\mathrm{Ne}^{*}$ decays by neutron emission, each reaction of this kind produces two neutrons, so it would be possible for one of the TNCs to be mistaken for a positron, creating a DC background. Rates were calculated using the SOURCES code [101]. At expected levels of contamination from the ^{238}U ($< 5\ mBq/kg$), ^{235}U ($< 3\ mBq/kg$), and ^{232}Th ($< 0.05\ mBq/kg$) chains [68], and standard abundances of oxygen isotopes (0.038%, 0.20% for N=17, 18 respectively),

it is estimated these processes will contribute 6-12 pairs of neutrons per day before detection efficiency. The majority of neutrons in this case come from ^{18}O, with the greatest α sources being ^{211}Po (19%) and ^{215}Po (18%) - both from the Ac/^{235}U decay chain. This can be an important background for the DC channel if reactor activity is low.

SF of ^{238}U also produces on average more than one neutron per fission [102], and γ-rays that could be mistaken for positrons, producing a DC background. Assuming a contamination of the gadolinium sulfate of 5 mBq/kg ^{238}U (Table 5.1), the SF rate is calculated to be 0.6 per hour in the ID before efficiencies.The γ-rays are assumed to have falling energy distribution [103]. The contribution to the background of SF turns out to be subdominant in this analysis, for both single neutron and DC channels. Beta delayed neutrons from SF will be negligible, as the beta delayed neutron branching fraction is on the order of 1/100.

6.2.3 Spallation

In SK, cosmic ray muons impinge on nuclei in the detector, causing spallation. This produces large numbers of fast neutrons, and unstable nuclei, the decay of which form the majority of background for certain energy regions of the solar neutrino and DSNB analyses.

Cosmic ray muons passing through the detector are detected very efficiently; products of spallation are already rejected at SK by vetoing events associated in time and space with a muon track [104]. The distance distribution of the products is estimated using MC. The half-lives of the unstable

nuclei give the time distribution of the events.

A fraction of muons create unstable daughter nuclei through spallation, and those that do can be efficiently identified through their light emission profiles [105, 106]. Strictly speaking, many of these products are not made directly by the fragmentation of an oxygen nucleus, but by bombardment with fast neutrons. Predictions of the yield of different products of spallation were published by Li and Beacom [105, 106, 107]. A measurement of the yield of certain isotopes which form backgrounds to the DSNB were measured by SK [104].

Although fast neutrons are visible when they capture on H or Gd, they are easy to reject and do not form a background. A neutron yield in water of $Y_{neutron} = 2 \times 10^{-4}\ muon^{-1}g^{-1}cm^2$ is predicted by Li and Beacom [107], which corresponds to an average neutron rate of

$$\mathrm{R_{neutron}} = Y_{neutron} \times L_\mu \times R_\mu \times D_{water} \times \mathrm{day/kt} = 5 \times 10^4\ \mathrm{kt^{-1}\ day^{-1}}, \quad (6.1)$$

where the mean muon path length ($L_\mu = 3.22 \times 10^4$ cm), and rate ($R_\mu = 2$ Hz) at SK are adopted from SK's spallation yield measurement [104], and the density of water (D_{water}) is assumed to be 1 g cm^{-3}. The thermalisation and capture time for the neutrons ($\sim 30\mu$s for Gd, $\sim 200\mu$s for H) is short compared to the muon rate at SK (2 Hz), so even vetoing the entire detector for 1 ms after every muon is very effective and does not introduce much dead-time.

Neutrons produced by muons not passing through the detector should be few in number; even fast neutrons will mostly not penetrate to the FV before

capturing as they would need to pass through >4.5 m of water to do so.

Some isotopes produced by spallation have half-lives >0.1 s, long enough that one cannot simply veto the entire detector. Among these, ^{17}N, ^{16}C, ^{11}Be, ^{11}Li, ^{9}Li, and ^{8}He all produce $\beta-$delayed neutrons, which could mimic the IBD signal. Yields of these isotopes are much smaller than that of neutrons; e.g. ^{9}Li is produced at a rate O(1 per kt day) [106, 104]. Often a neutron will be produced in association with these daughters, so potentially they could be more efficiently removed by tagging the preceding neutron capture [107].

The distribution of the time of TNC for fast neutrons and β-delayed neutrons from spallation daughters is shown in Figure 6.2. The thermalisation time is assumed to be 5 μs for all neutrons, though in reality it has an energy dependence. A capture time of 30 μs is assumed. Yields and half-lives were taken from [107]. This shows that a veto based only on time is highly effective for fast neutrons, but not for β-delayed neutrons.

The energy spectra of the β rays produced by βn decays of the spallation products listed by Li and Beacom [107] were calculated using the *Betashape* tool [108] for the NNDC ENSDF database [109]. While ^{11}Be and ^{9}Li are of interest for the DSNB analysis, ^{17}N especially is present in the energy region of interest for the pre-SN analysis, as shown by Figure 6.3.

These isotopes are included as a background to the DC channel, assuming the Li and Beacom yields [107], with rates calculated by the method shown in Equation 6.1. In the pre-SN analysis, it is assumed that spallation reduction techniques will eliminate 95% of these backgrounds [106] while introducing 20% dead-time. Spallation reduction in SK is currently performed off-line, and will need to be moved on-line.

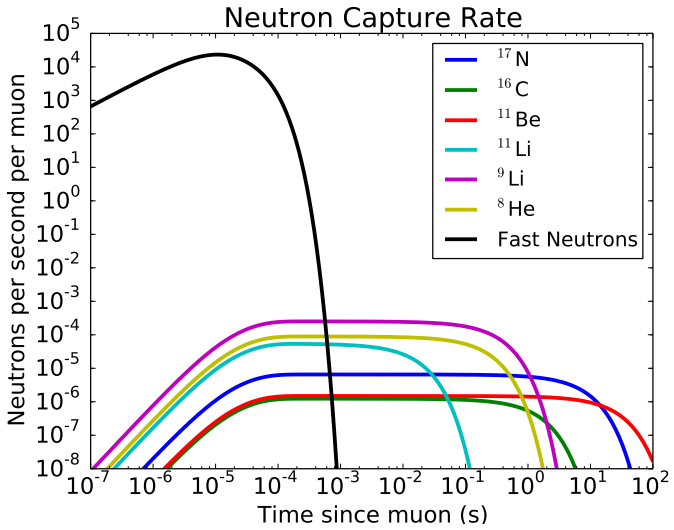


Figure 6.2: Distribution of neutron capture times from products of spallation. Fast neutrons will thermalise and capture quickly, while β-delayed neutrons will continue to be produced for much longer.

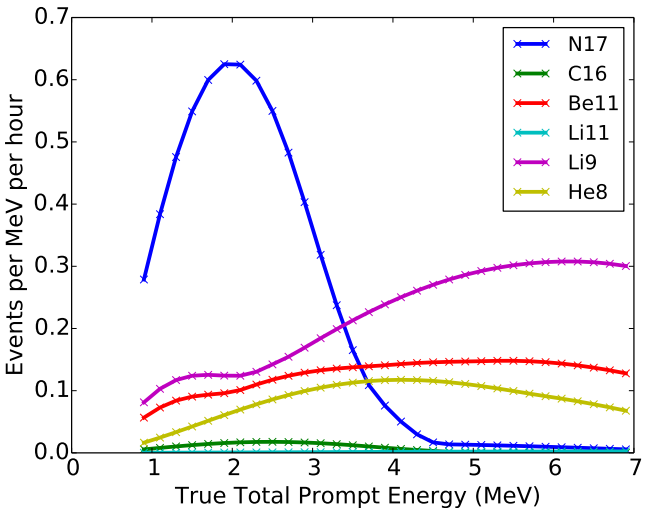


Figure 6.3: Distribution of true β energies (above Cherenkov threshold) of spallation daughters that decay by βn. ^{17}N is especially high in the energy region relevant to the pre-SN analysis (below 5 MeV).

Other unstable isotopes are produced by spallation, but only those that produce β-delayed neutrons are included in this way. Events from other decays not producing a neutron may already be present in the accidental background data sample, as detection does not rely on the presence of Gd. Spallation of Gd and S nuclei were not included, as the overall abundance of the nuclei is small compared to O.

6.3 Reactor Neutrinos

Reactor and geo anti-neutrinos are an irreducible background, being the same particles in the same energy range as the signal. The reactor background depends strongly on the number of Japanese nuclear reactors that are running. To account for this, the reactor and geoneutrino flux was calculated using the `geoneutrinos.org` web app [110], which combines reference models for reactor neutrinos [111] and geoneutrinos [112]. Reactor activity is assumed as the mean values given by IAEA's PRIS database for the years 2010 and 2017 [113]. During 2010 most Japanese nuclear reactors were running as normal, however all were switched off in 2011 and 2012. Some reactors began to be returned to operation since, so 2017 is taken to represent the lowest flux which is likely in the future, and 2010 the highest. If Japanese nuclear reactor activity returns to 2010 levels, then reactor neutrinos will be an important background to the DC channel of this analysis.

The assumed flux of reactor and geo $\overline{\nu}_{\mathrm{e}}$ is shown in Figure 6.4. The Y-axis unit TNU = IBD events/10^{32} free protons/ year, where 1 kt water contains 0.668559×10^{32} protons. 1 TNU is therefore $\sim$0.002 event per day per kt wa-

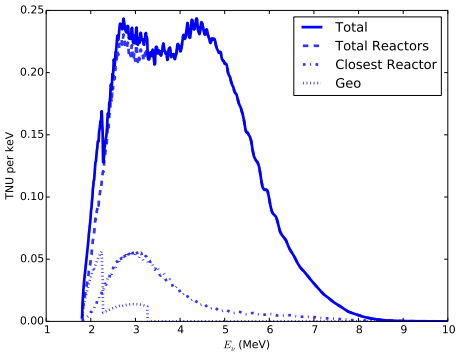
ter. The majority of detectable events will come from reactor neutrinos. The flux is an order of magnitude higher in the 2010 case compared to the 2017 case.

There is also some opportunity to regard reactor neutrinos as a source of signal. It may be possible to identify when certain reactors are switched on during SK-Gd, from an increase in the reactor neutrino signal. The number of events expected from reactor neutrinos is low enough that a reactor switching on is not expected to create a false pre-SN alarm. Conversely, it would not be possible to identify with high confidence over a single day that neutrinos were being seen as the result of a nuclear reactor switch-on. Preliminary studies suggest it could take months to accumulate sufficient statistics to identify that a reactor at the (nearby and high capacity) Kashiwazaki nuclear power plant had returned to operation.

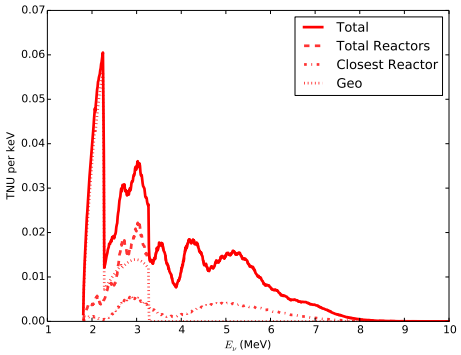
6.4 Single Neutron Event Selection

Over the 6.7×10^3 hours of WIT data used to estimate background, there were 9×10^{10} recorded events: 1.3×10^7 events per hour. Simulated neutron captures on gadolinium in the ID (referred to as *signal* from now on: captures on H are neglected for now) pass the WIT trigger requirements 80% of the time.

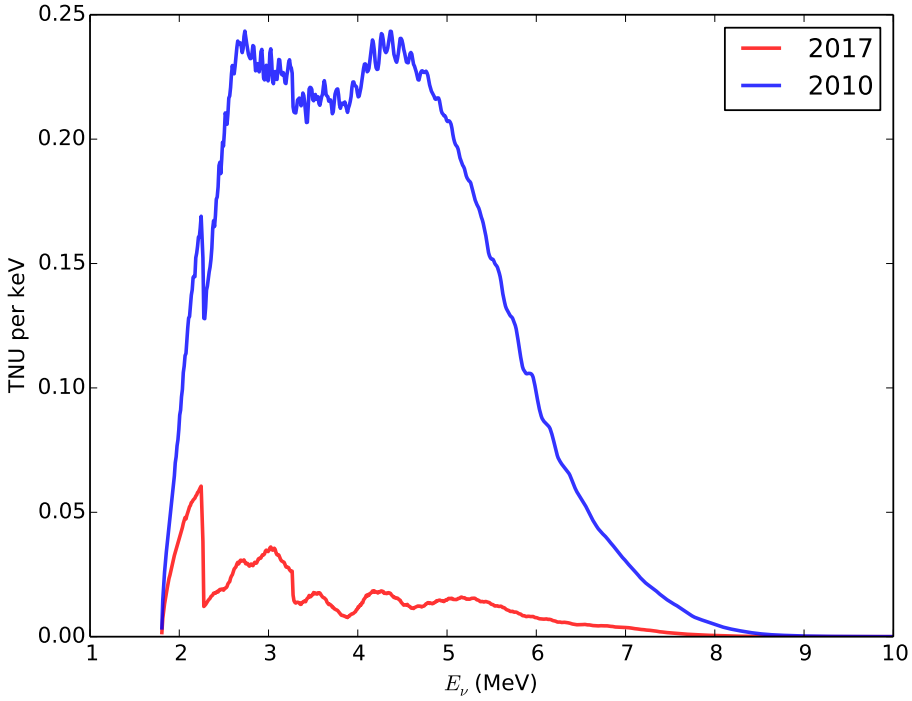
The pre-selection applied to single neutron candidates is not the same as that applied to the delayed neutron candidates. Events are initially selected if they are reconstructed within the SK FV - i.e. more than 2 m from the detector walls and bottom. A threshold of 20 is applied to the number of on-



(a) 2010



(b) 2017



(c) Comparison

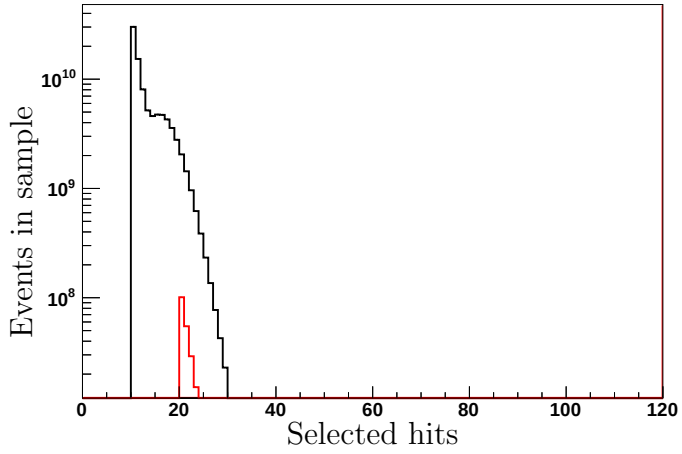
Figure 6.4: Reactor and geo $\overline{\nu}_e$ flux under 2010 and 2017 reactor activity assumptions. Differences in shape are created by different oscillation baselines contributed by different reactors.

line selected hits (*n18* defined in section 4.9). Also, events with $n18 > 60$ are rejected as they are unlikely to be of interest. Figures 6.5, 6.6, and 6.7 show the distributions in n18, squared radial position and vertical position before and after these cuts for WIT data (as background) and simulated TNC on Gd in the GLG4SIM γ-ray model (as background).

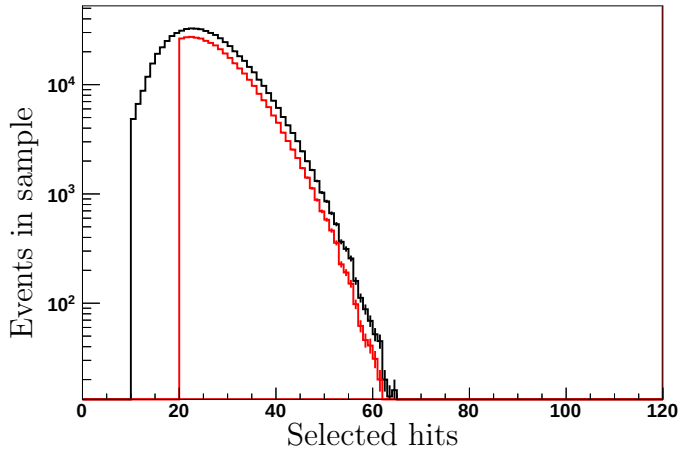
The overall background reduction in this step is a factor ~ 400. For TNC on Gd in the ID, using the GLG4SIM γ-ray emission model, the efficiency of these cuts is 58%. The cut on n18 all but eliminates TNC on hydrogen.

Events are vetoed if they were at the same time that an automatic calibration source was activated. A small volume is also cut out around the position of calibration sources. This only has a small effect on the overall background rate and signal efficiency at this level, but prevents the events from calibration sources being present further downstream.

Some initial tests of BDT training to select γ-ray cascades from TNC on Gd (BDT training is covered further in chapter 7) showed that events with $n18 < 26$ and $effwall < 800$ were almost never selected by the BDT, for signal or for background, so this region was cut out in pre-selection. The effect of this is shown in Figure 6.8 and Figure 6.9. This is applied to both DC and single neutron channels.

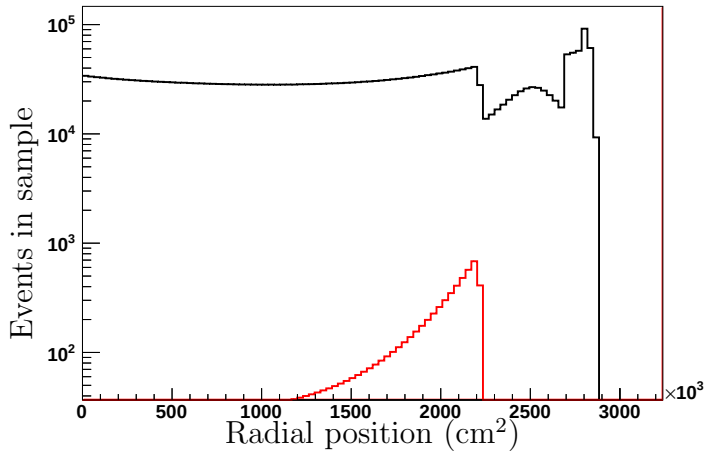


(a) Background data

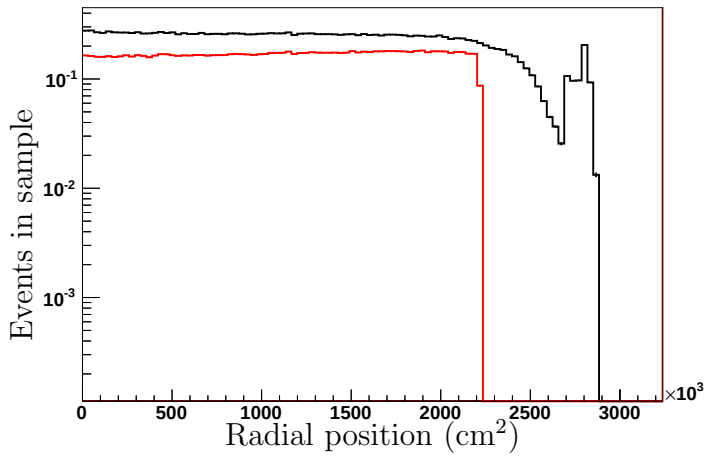


(b) Gd MC

Figure 6.5: Distribution of online selected hits *n18* for events passing the WIT (**black**) and volume and n18 cuts (**red**). The MC is normalised so that area equals 1 before the cuts.

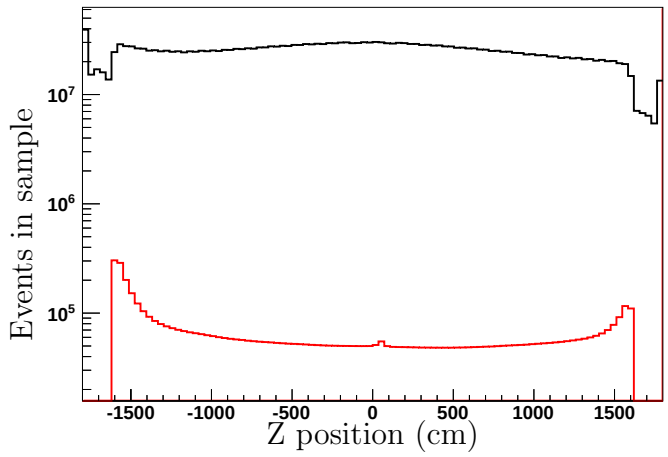


(a) Background data

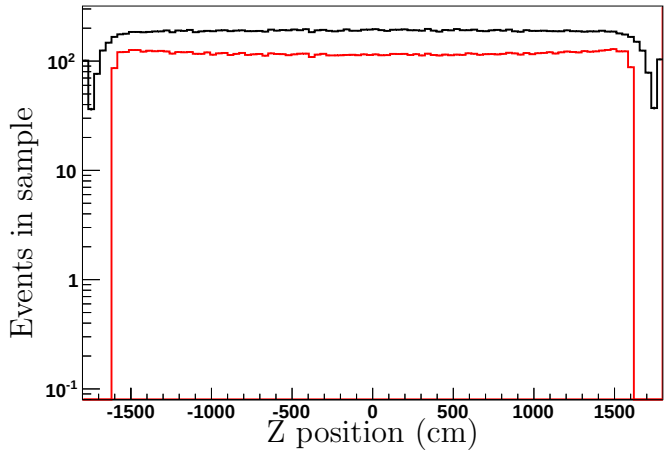


(b) Gd MC

Figure 6.6: Distribution of reconstructed squared radial position for events passing the WIT (**black**) and volume and n18 cuts (**red**). The MC is normalised so that area equals 1 before the cuts. Squared radial position is shown so that uniform distribution would be a flat line.

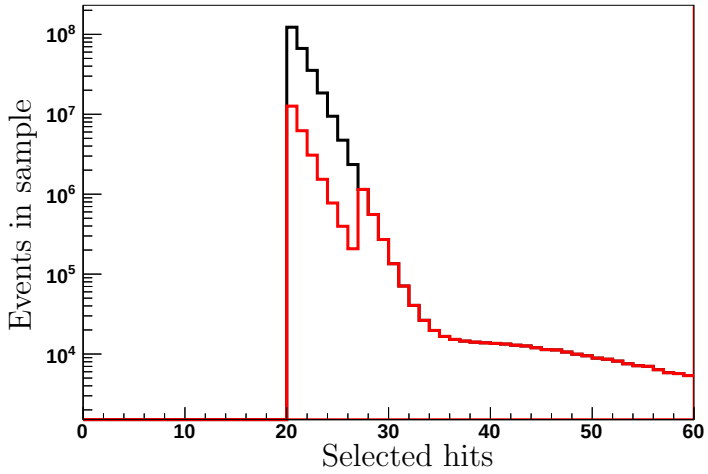


(a) Background data

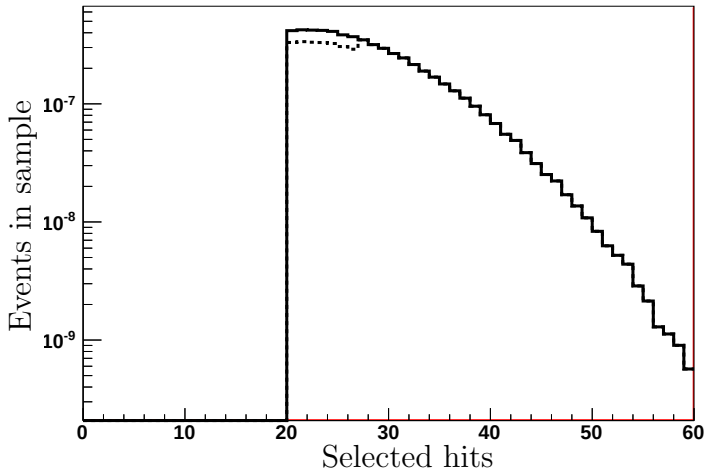


(b) Gd MC

Figure 6.7: Distribution of reconstructed vertical position for events passing the WIT (**black**) and volume and n18 cuts (**red** in top/dotted in bottom). The MC is normalised so that area equals 1 before the cuts.

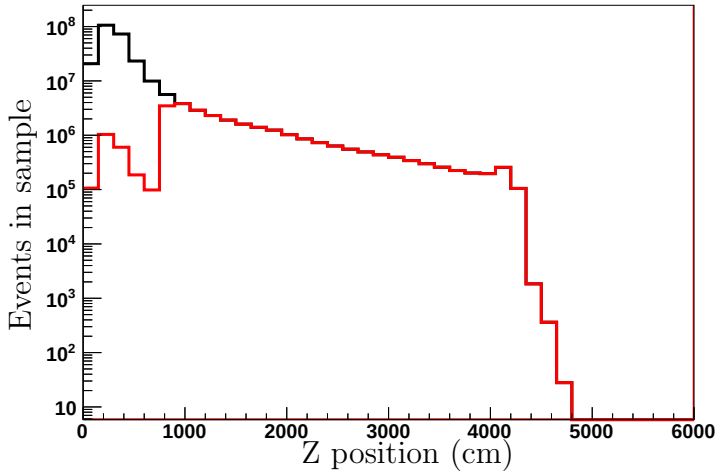


(a) Background data

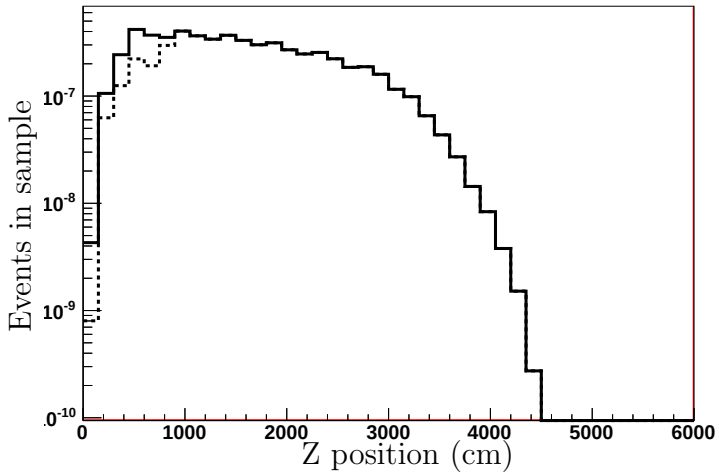


(b) Gd MC

Figure 6.8: Effect of n18 and effwall preselection on n18 distributions of Gd MC and background data. **Black** shows the distribution before selection, **red** (above) or dotted (below) after selection



(a) Background data



(b) Gd MC

Figure 6.9: Effect of n18 and effwall preselection on effwall distributions of Gd MC and background data. **Black** shows the distribution before selection, **red** (above) or dotted (below) after selection

6.5 Delayed Coincidence Event Selection

6.5.1 Spatial Distribution

A key discriminating variable for the selection of delayed coincidences is the difference in reconstructed position between the prompt and delayed parts of the event (dR). For accidental coincidences, the dR distribution is mainly determined by the spatial distribution of background triggers. For signal, it mainly comes from the position reconstruction resolution of the two parts of the event. Therefore, it is correlated with the visible energy of both parts of the event, as higher energy events have better spatial resolution. Figure 6.10 shows the relationship between dR and the energy of the prompt event in the detector simulation.

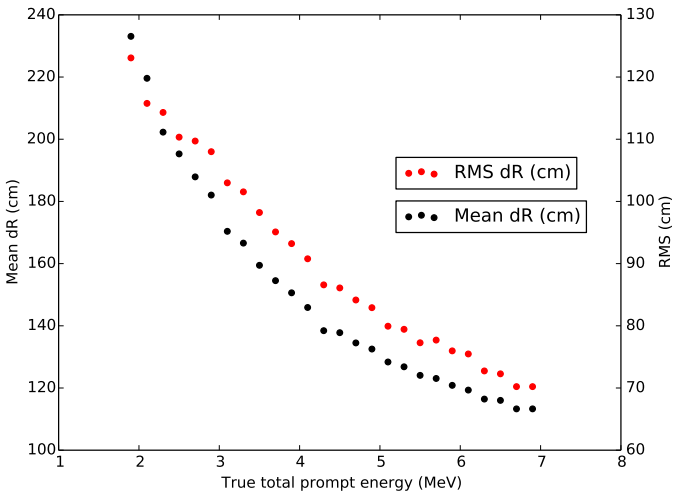


Figure 6.10: The mean and RMS of dR of simulated DC events decrease with increasing prompt event energy, due to improving vertex resolution, calculated by the detector simulation.

Positrons and γ-ray cascades from TNC on Gd were simulated at 64 positions in the inner detector. The positrons were simulated in 31 energy steps between 0.8 MeV and 7 MeV. This passed through the normal SK detector simulation, then the WIT trigger simulation including noise injection. Sets of events simulated at the same position were then paired up, and the distance taken between them. Overall trigger efficiency was taken to be the product of the individual trigger efficiencies at a given location and positron energy.

6.5.2 Timing Distribution

Another key discriminating variable is the time difference between the two parts of the event. For accidental background, the distribution is approximately flat. For signal, this comes from the time taken for the neutron to thermalise and capture. The value used for this came from a fit to americium-beryllium neutron source data collected in EGADS with 0.2% gadolinium sulfate loading (see chapter 5).

6.5.3 Initial Search

In order to search efficiently for coincidences between independently reconstructed events, the reconstructed time, reconstructed position, reconstruction quality and number of selected hits *n18* are read into memory. If either of the event candidates outside the 22.5 kt FV are rejected. These events are then sorted into order of trigger clock.

The coincidence search loops over all events, initially any event can be considered as a prompt or delayed event candidate. For a given prompt

event candidate with trigger clock C, other events which have a trigger clock between $C-1$ and $C+12$ are considered as delayed event candidates. Roughly speaking this selects events from -17 to 290 μs relative to the prompt event. This is deliberately wide as the off-time events are useful as a side-band.

For pairs of events passing the first criterion, the time difference between the two events is calculated more precisely by adding the difference of the trigger clocks times the trigger clock increment (1.707×10^4 ns) and the reconstructed event time. The distance between the reconstructed vertices of the two events is calculated.

Pairs of events with distance separation <5 m and time difference 0.05-200 μs are saved, provided there is exactly one delayed event candidate. If an event is selected as a delayed event candidate, then it is no longer considered as a prompt event candidate.

The spatial separation of pairs of events in the accidental background depends mainly on the distribution of low energy events in the detector, as the coincidences come from pure chance. On the other hand, the spatial separation of real coincidence events depends on any true separation of the two event vertices (e.g. from neutron transport), as well as the vertex reconstruction resolution. Note, however, that neutron transport was not modelled in this study, i.e. the neutrons were assumed to capture at the same point at which they were produced. This is a reasonable assumption as, at these low energies, the distance travelled by neutrons before capturing (of order 10 cm) is much smaller than the position reconstruction resolution (of order 1 m).

Pairs of events selected in this way from SK-IV WIT data are included as the accidental background in the pre-SN analysis. From the spatial and

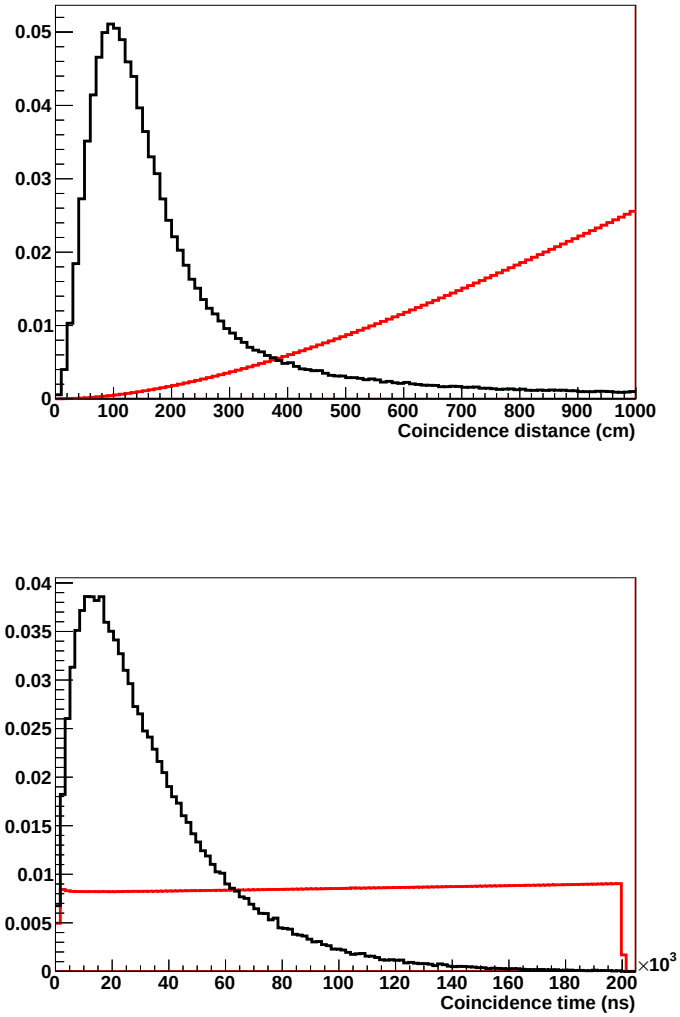


Figure 6.11: Distribution of (a) coincidence distance and (b) coincidence time for simulated low energy DC IBD events (**black**) and accidental background (**red**). The histograms are normalised to equal area.

temporal distributions, selected events are consistent with being random coincidences.

6.6 Results

The output of this part of the study is a detector response model and background model that can be used for low energy IBD events at SK-Gd, at lower energies than had previously been considered. This model is limited as it is based upon an un-tuned simulation of the γ-ray emission from TNC on Gd, rough assumptions about the background, and SK-IV pure water data; it will obviously be superceded when real SK-Gd data become available.

The pre-selection described in section 6.4 does not reduce background sufficiently for the single neutron channel to be useful for pre-SN detection, and DC event selection would also benefit from the reduction of the number of neutron candidates. Further reduction is applied using a boosted decision tree (BDT), which combines feature variables in a multivariate analysis, which is described in chapter 7. This is then used to estimate the sensitivity of SK-Gd to pre-SN $\overline{\nu}_{\mathrm{e}}$ in chapter 8.

Chapter 7

Multivariate Selection

Firstly, some introductory material is given in section 7.1. Then the specific application of boosted decision trees (BDTs) to the identification of TNC on Gd in SK is discussed which is original work.

7.1 Introduction

A straightforward approach would be to find the optimal rectangular cuts that provide the best signal selection. We will see that much better performance can be achieved with a more sophisticated approach. The pre-selection (see section 6.4) is necessary as too much memory and CPU time is required to train the BDTs on unreduced data with a sufficient sample of detector live-time - it is better to apply carefully chosen cuts thereby allowing an increase the sampled live-time.

Attempts were made to produce a multivariate method of pre-selection, based only on the variables already available on-line. The result of this

could be considered an energy and reconstruction quality dependent FV cut. However, improvements to the signal efficiency were found to be small, so rectangular cuts were kept for the sake of interpretability.

In published DSNB analyses at SK, an artificial neural network was used in order to select 2.2 MeV γ-rays [57]. In this study, for the selection of TNC on Gd, several multivariate methods were tested, including Fisher's linear discriminant (LD) and artificial neural networks (ANN). Ultimately BDTs were preferred due to their robustness to overtraining, and straightforward hyperparameter optimisation; this will be explored further in this section.

In general, a well optimised ANN will perform better than a BDT. However, this requires the number of nodes, number of hidden layers, and choice of variables to be optimised, which is often a highly involved process and which can take very large CPU times. By comparison, BDTs are quick to train, and quick to optimise: they will outperform an ANN which is not well optimised, or for which the training data sample was not sufficiently large [114]. LDs are a long established technique which works well provided that discriminating variables are close to having a Gaussian (normal) distribution, and do not contain non-linear correlations. Furthermore, LDs are likely to out-perform more complicated multivariate methods when training data is scarce.

For this part of the analysis, only the reconstructed variables of neutron captures on gadolinium were considered. That is, coincidence properties were not considered, and captures on hydrogen were not included.

BDTs work by producing decision tree classifiers one at a time; decision trees are built out of decision nodes. At each decision node, the samples are

cut into two *leaves*, with the optimal cut being that which maximises the difference between the Gini coefficient of the parent leaf and the sum of the Gini coefficient weighted by the proportion of events of the daughter leaves. The Gini coefficient is defined as

$$G = p(1-p), \tag{7.1}$$

where p is the classification accuracy. Each leaf can then be split further, until a limit is reached. Tree growth can be halted when the depth reaches a limit, when further splits would lead to leaves containing too few events, or above a certain limit in purity. If no limits are placed on tree growth, an overtrained tree would be produced that very finely splits the training data sample, but which has a highly variable response on independent data samples [115] (imagine, for example, a tree with each training sample datum alone in its own leaf node). In this study, tree depth was limited to 3, and the number of events per leaf was limited to >1000.

For each decision tree, data that were misclassified by previous decision trees are given increased weight, a process called adaptive boost (AdaBoost). Trees are accumulated and ultimately evaluated as an ensemble. After the creation of each decision tree, the weight of each event that has been misclassified by that tree is multiplied by a boost weight given by

$$\alpha_{boost} = (\frac{1-\epsilon}{\epsilon})^{\beta_{boost}}, \tag{7.2}$$

where ϵ is the misclassification rate of the tree. The sum weight of all events

is then renormalised so that it remains constant. This leads to events which are misclassified by a tree with a low misclassification rate having increased weight for the construction of subsequent trees. The boost rate β_{boost} controls the learning rate of the classifier through the weight increase given to misclassified events [115].

This leads to an ensemble of weak trees which together classify the sample well, but individually do not. The overall classification of the BDT (or any ensemble of N classifiers combined using AdaBoost), for an event with feature variables $\underline{x}$, is then the sum over trees

$$y_{boost}(\underline{x}) = \frac{1}{N}\sum_{i}^{N} \ln(\alpha_i).h_i(\underline{x}), \tag{7.3}$$

where α_i is the boost weight of the i^{th} tree in the ensemble, and $h_i(x)$ the classification result of tree i for input vector x.

The importance of a variable in a decision tree, or a collection of decision trees such as in a BDT, can be calculated as the sum, over all nodes using that variable, of the squared change in the Gini coefficient times the proportion of events in the node [115].

Training and testing used the TMVA software [115]. The γ-ray distribution for neutron capture on Gd used for training was that created for GLG4SIM (see section 5.5), but the distribution provided by J-PARC is included for comparison, and for the consideration of overtraining. Data were split into training and testing samples at random.

7.2 Training Considerations

In preparing any multivariate discriminator, consideration must be made of the resources available. In the batch computing system used for this study, memory was limited to 4096 MB. The TMVA software loads the entire event tree into memory during training and testing, effectively limiting the number of feature variables and training/testing events that can be used. Around 10^7 total events can be handled with around 10-20 variables. Because of the memory limit, it is worth experimenting with reducing the number of feature variables in order to increase the amount of training data, as described later in this chapter. Time limits for this batch computing system were 24 hours, which meant that BDTs with $>10^4$ trees would sometimes not be completed. There is no capacity in TMVA to pause and resume training. Interactive servers with higher memory limits, and no time limits, were available, but it is unreasonable to use these heavily to train many different discriminator permutations, as is required when testing many classifiers.

As the background data sample used for training and testing is taken from real SK-IV pure water data, it is important to ensure that the sample is representative. For this reason, the data were a random sub-sample of data from all available runs. Initial attempts used samples of arbitrarily selected recent runs, and it was found that performance was poorer than expected when the discriminator was tested on a broader sample.

7.3 Method

The background sample used is larger than the signal MC sample because the targeted background reduction is on the order of 10^5, while the target signal efficiency is >10%.

A classic method of comparison of the effectiveness of classifiers in machine learning is to use the area under the response operator characteristic (ROC) curve (examples shown in Figure 7.1). An ROC curve plots the background rejection against signal efficiency. A perfect classifier would reject all background and be fully efficient for signal, so would have an integral of 1.

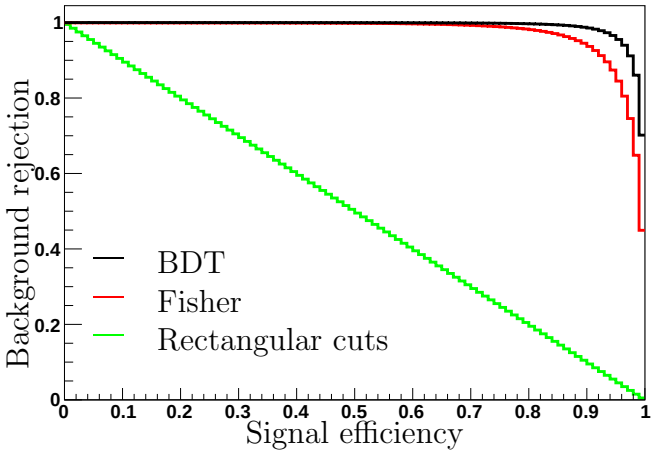


Figure 7.1: ROC curves of some example classifiers. The integral of the curve is one way to quantify performance.

Comparison can also be made using the separation parameter, which describes how effectively two samples can be separated using a given variable, defined as

$$1 - A \otimes B = 1 - \sum_{i=1}^{N} \frac{A_i B_i}{aA_i + bB_i}, \tag{7.4}$$

where A and B are two distributions, a and b are the fraction of events in

bin i that belong to distibutions A and B respectively, and A_i and B_i are the probabilities of an event in the respective distributions being in bin i. It is not dependent on the normalisation of the samples. A value of 1 means the samples could be perfectly separated, a value of 0 means the samples have exactly the same distribution. This parameter can be mathematically related to the error on a likelihood analysis, and is generally useful for estimating how useful a variable will be in a multivariate analysis. It can also be straightforwardly calculated for individual feature variables as well as a classifier that combines them.

Perhaps more intuitive for particle physicists is the maximum expected 'significance' $\frac{S}{\sqrt{B}}$, assuming what the background normalisation is known. This is based on the assumption that sample error is approximated by $\sigma = \sqrt{N}$ for a sample of size N, so $\frac{S}{\sqrt{B}}$ is a number of standard deviations from the background only expectation. In fact, all three of these methods are closely correlated, as shown by Figure 7.2.

Increasing the number of trees will in general improve the performance and reduce the variability of the the classifier. However, at some point adding additional trees will lead to negligible further improvement, and will require additional computing resources. Reducing the boost rate will mean that more trees are required to reach saturation, but can lead to a better performing and less variable classifier if the data are very complex.

The hyperparameters *NTrees* and boost rate β_{boost} were varied. Initially the number of training events was limited to 10^5 each of signal MC and background, while 4×10^6 background and 4×10^5 signal MC testing events were used. The numbers of training events were also varied in order to see

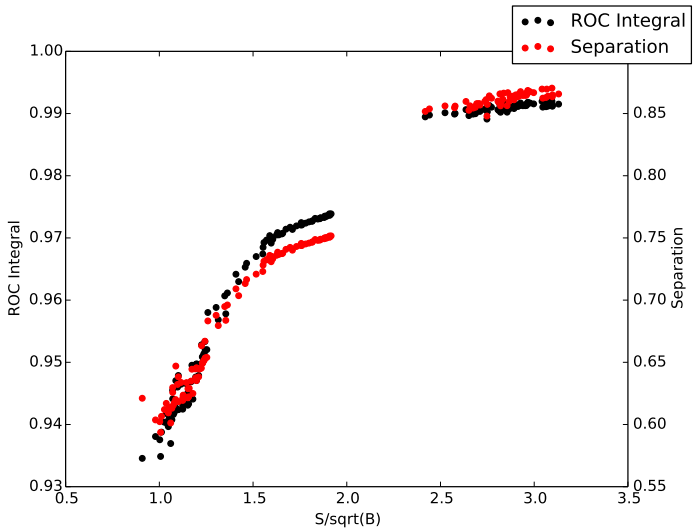


Figure 7.2: Different methods of calculating the effectiveness of classifiers are closely related. A large gap is visible because examples of rectangular cuts, LDs and BDTs are all shown, with a big gap in effectiveness between the cuts and the other methods.

their effect on overall performance, up to $\sim 4 \times 10^5$ for signal MC (i.e. half of those that passed preselection out of 10^6 generated), and up to 4×10^6 for background (a 1% sample of events in available unreduced WIT data that passed preselection). The maximum sample sizes here are set by the memory limit mentioned in section 7.2.

The variables used for training were varied. Initially only the variables which are calculated on-line by the WIT system were used. Then additional variables expected to contribute to successful discrimination were included. Variables were then removed according to their variable importance ranking. Variable definitions and distributions will be given for those deemed most important in the final selection.

7.4 Results

7.4.1 Hyperparameters

In Figure 7.3, the effect on performance of changing the number of training events is shown. Boost rate is set at 1.0 and NTrees at 1000. Above a certain number of events, the nominal performance does not seem to increase (to within the sample error of the test sample).

Figure 7.4 shows the difference in the integral of the ROC curve calculated from the training and test samples. A large difference means that the classifier is showing high variability, whereas a low difference means it is robust. The difference decreases with the addition of training events. When $>10^6$ training events are used, the difference is very small. This suggests that for this combination of hyperparameters, and this dataset, 10^6 background events is a sufficiently large training sample. The boost rate was set at 0.7 and 1.0, and the number of trees 1000 and 2000. The difference in area was generally less when the boost rate and number of trees was lower. In Figure 7.3, the classifiers with more trees had a better overall performance, although the differences in performance were only small.

7.4.2 Variable Inclusion

Figure 7.5 shows the performance of BDT classifiers trained with different sets of variables included, and with a varied number of trees. Issues of variable inclusion are discussed further below. It was found that the difference made by altering the boost rate parameter was comparatively small. Also

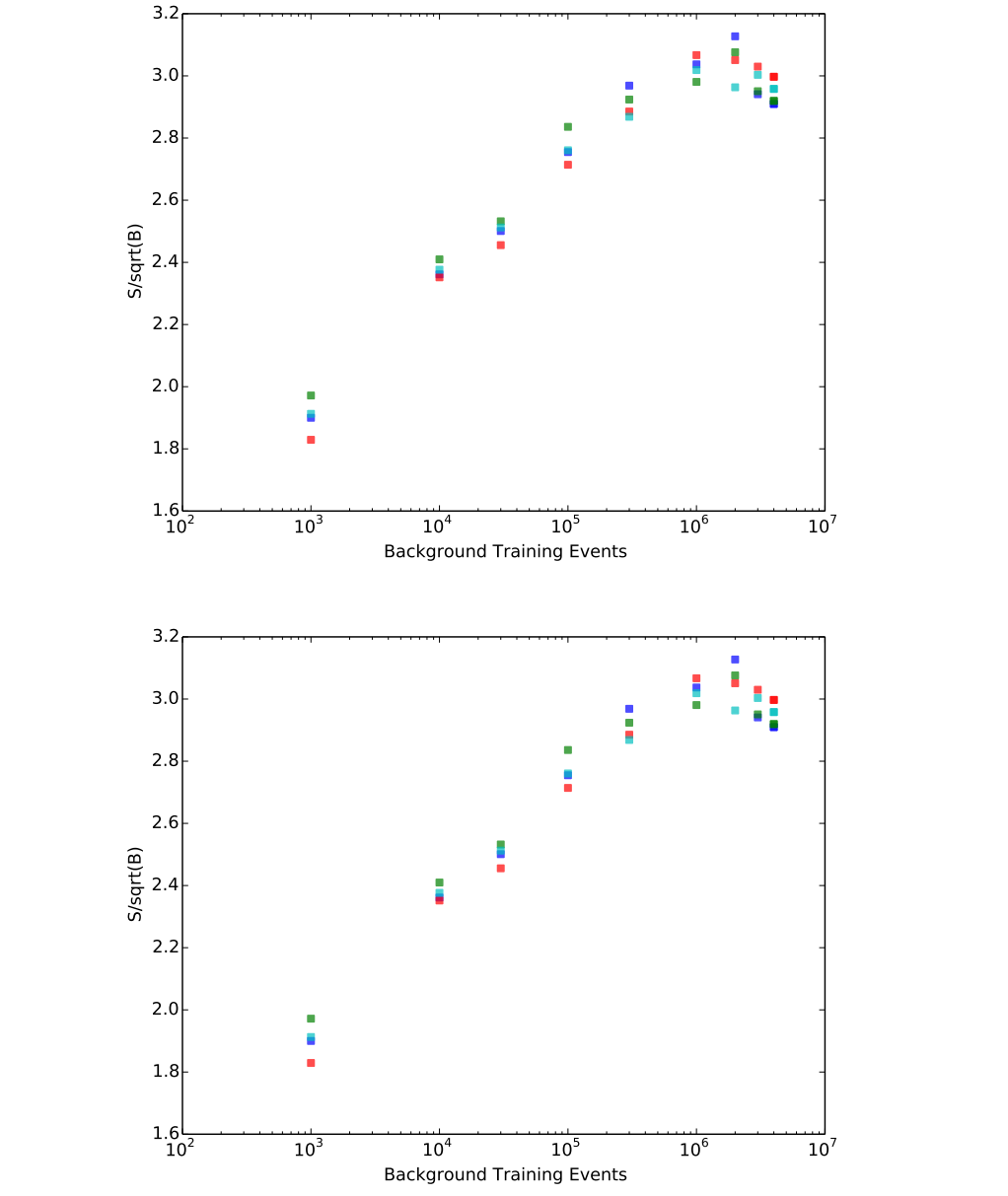


Figure 7.3: Performance comparison of BDTs with fixed hyperparameters as number of training events is increased. The number of test events is kept constant. The number of trees and AdaBoostBeta are the controlling hyperparameters for a BDT. AdaBoostBeta is defined in Equation 7.2.

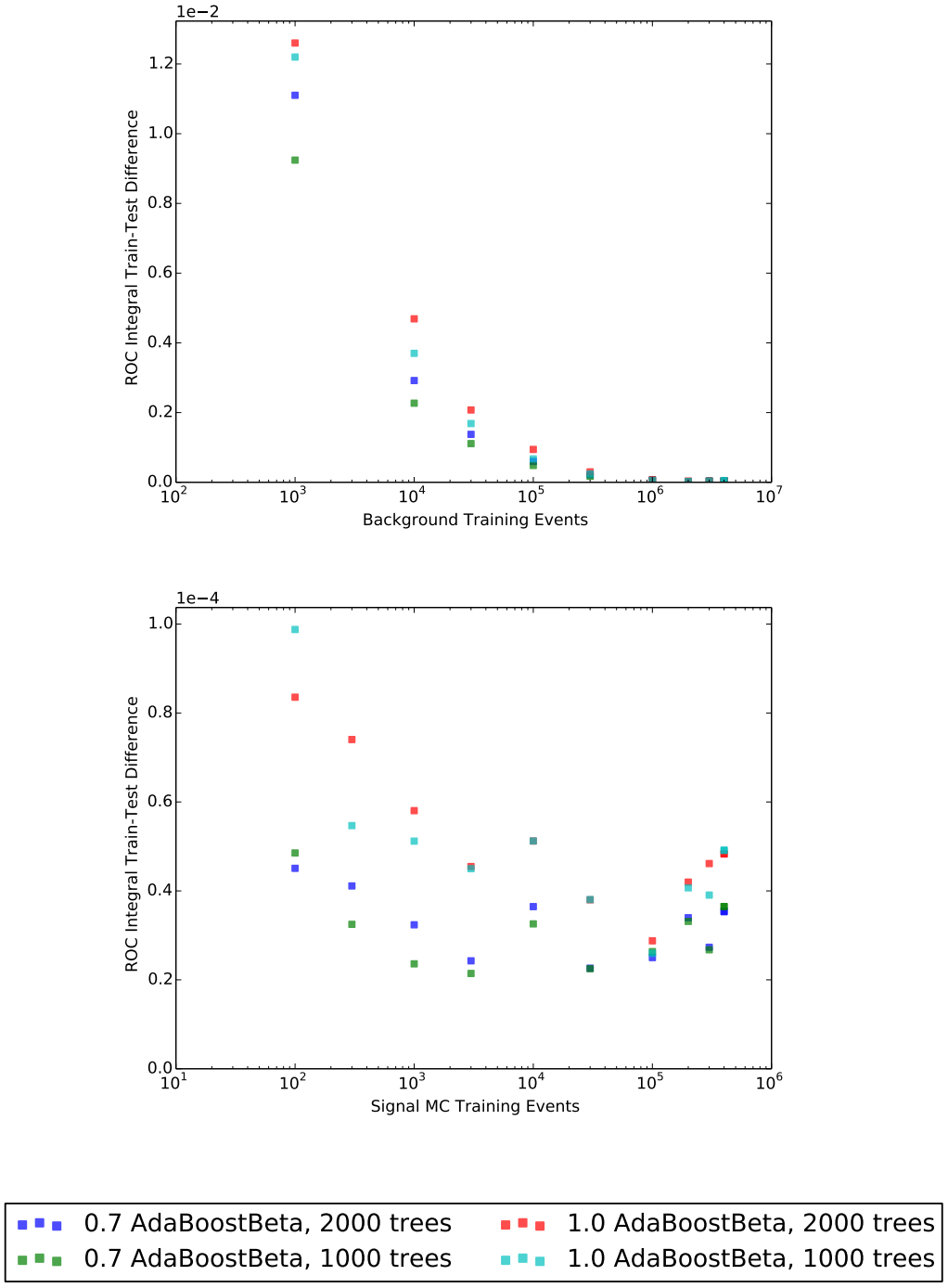


Figure 7.4: ROC integral difference between training and test samples, against number of (a) background, and (b) signal MC, training events. The number of test events are constant.

shown are rectangular cut and LD classifiers. To estimate the effectiveness of the classifier in use with $\frac{S\times\epsilon_S}{\sqrt{B\times\epsilon_B}}$ (efficiency ϵ), $B = 10^6$, $S = 10^2$ were assumed. The training sample size was 10^5 each for signal MC and background. With a boost rate of 1.0 and 100 trees, the BDT using only the WIT online variables out-performs the rectangular cut and LD classifiers by a clear margin, regardless of which variables are included. Furthermore, the inclusion of all available variables gives a clear benefit in performance compared to the on-line variables alone.

While the separation described in Equation 7.4 is consistent as the training samples are made larger, the importance of the variables in the BDT does not appear very stable. With 2000 trees and a boost rate of 1.0, almost all of the variables appear in the top 10 most important variables of one of the classifiers shown in Figure 7.4, and there is no variable that appears in the top 10 for all of the classifiers. This could be because several of the variables are highly correlated, and therefore interchangeable - even if the separation of a parameter is high, it may not be adding extra information if it is highly correlated with another variable. For example, both the number of hits counted on-line ($n18$) and the off-line reconstructed energy were included ($bsenergy$) - these are 91% correlated for signal and 71% correlated for background.

The ten variables which received the highest importance score, in a classifier trained with 2000 trees and a boost rate of 1.0, and the largest training data sample, were included and training run again with a variety of hyper-parameters. The variables chosen for this are listed in Table 7.1. The choice to use the top ten was arbitrary. There is a clear degradation in performance

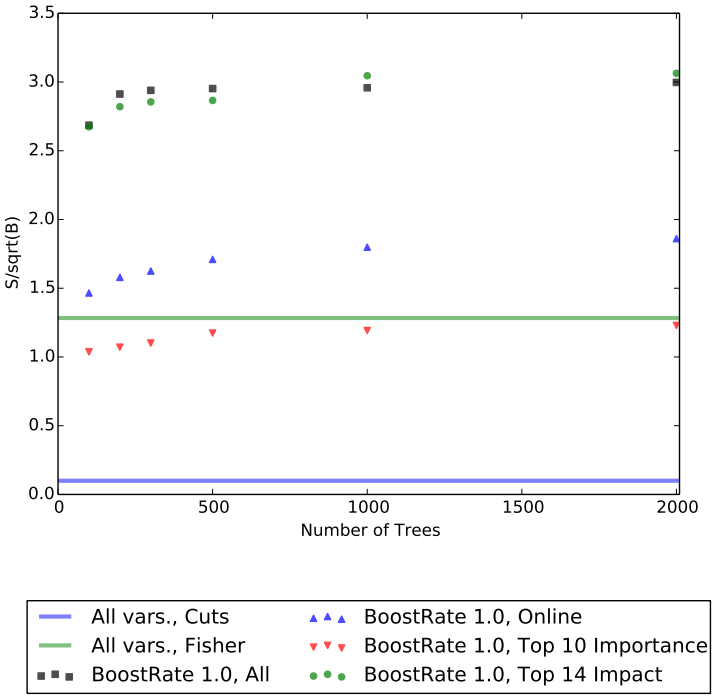


Figure 7.5: Performance comparison of BDTs, with varied feature variable inclusion and hyperparameters. Linear discriminators and rectangular cuts are shown for comparison. Top10Importance refers to the 10 variables (listed in Table 7.1) with the highest BDT importance statistic, whereas Top14Impact refer to those (listed in Table 7.2) which have the most impact on the performance when included in the classifier. The apparently better performance of "Top 14 Impact" than "All" is likely down to statistical fluctuations.

of the BDT compared to when all the available variables are included, or even that in which only the online variables are included, which can also be seen in Figure 7.5. It appears that the BDT variable importance method is flawed.

In order to see the effect of variable inclusion in more detail, variables were included one-by-one in order of their importance ranking. The effect is shown in Figure 7.6. The exclusion of some variables had only a small impact on performance, and some the exclusion of some had a positive effect. Some variables which had a lower importance ranking had a large impact on performance. The variable making the biggest impact on performance was *fromwall* (the distance from the recon. vertex to the detector wall) - from what is known about SK it is not surprising that this is an important variable, but it does not appear consistent with the BDT variable importance ranking.

Including only those variables that seemed to have the most positive impact on the classifier, by the method shown in Figure 7.6, another set of BDTs was trained, and the performance compared again. This time 14 variables were included. Performance was as good as when all 26 variables were included, also shown in Figure 7.5. The variables included are listed in Table 7.2. Note that there is limited overlap with Table 7.1, shown with the asterisk. Comparing the best performing BDTs in this study with that used in the SK publication on pre-SN [3], which did not use a few of these variables, there is marginal improvement, shown in Figure 7.7. Correlation matrices for the different variables are shown in Figure 7.10.

A justification is given below for each of the variables listed in Table 7.2:

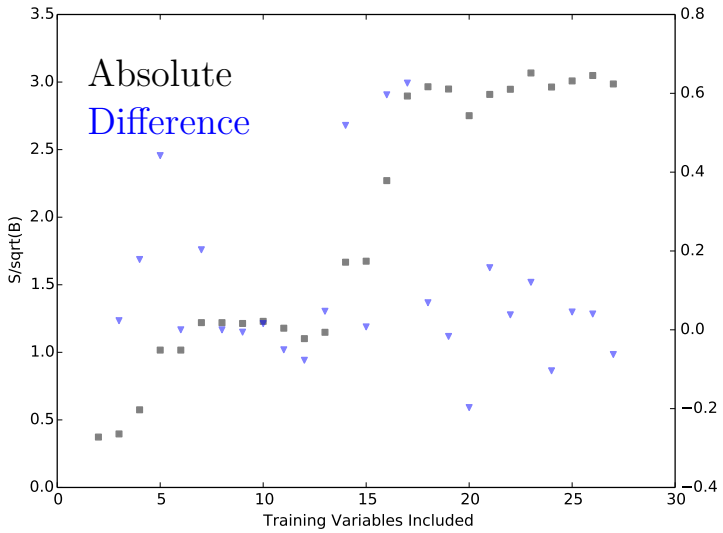


Figure 7.6: Performance comparison of BDTs, with feature variable changed in order of importance ranking.

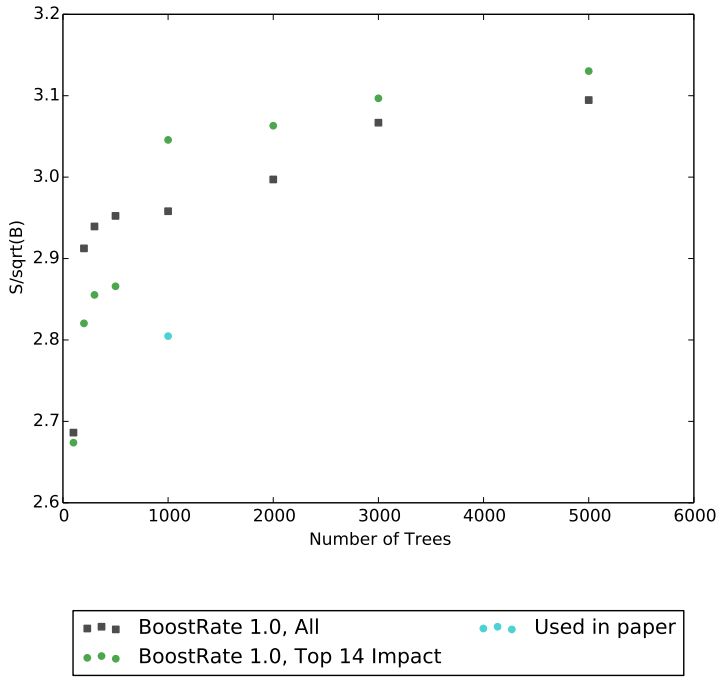


Figure 7.7: Best performing BDTs from this study compared to that used in [3]. There is marginal improvement.

	Variable	BDT score	Explanation	See also
∗	*bsenergy*	0.26	Recon. energy	section 4.9
	mean_cosCh3hit	0.19	Mean three hit cone cosine	subsection 4.9.4
	cldirks	0.083	(On-line) ClusFit direction KS test	section 4.9
	bgoodness	0.065	(On-line) BONSAI vertex goodness	section 4.9
	cgoodness	0.041	(On-line) Clusfit vertex goodness	section 4.9
∗	*cgoodness0*	0.041	(On-line) Clusfit vertex goodness	section 4.9
	pclose	0.040	Proportion of hit pairs with close angle	subsection 4.9.4
∗	*Beta[2]*	0.032	Isotropy parameter	subsection 4.9.4
	Beta[3]	0.031	Isotropy parameter	subsection 4.9.4
∗	*Beta[4]*	0.031	Isotropy parameter	subsection 4.9.4

Table 7.1: Variables selected for inclusion in BDT, based on BDT importance scores. Those not appearing in Table 7.2 are marked with an asterisk.

	Variable	Explanation	See also
*	*fromwall*	Distance from recon. vertex to detector wall	section 4.9
*	*effwall*	Distance in recon. direction from recon. vertex to detector wall	section 4.9
*	*MSG*	Multiple scattering goodness	section 4.9
	cgoodness	ClusFit goodness of fit	section 4.9
*	*bz*	Recon. vertex vertical location	section 4.9
	pclose	Proportion of hit pairs with close angle	subsection 4.9.4
*	*bsdirks*	BONSAI recon. direction KS test	section 4.9
*	*Beta[1]*	Isotropy parameter	subsection 4.9.4
*	*mode_ch3hit*	5 bin mode three hit cone angle	subsection 4.9.4
	mean_cosCh3hit	Mean three hit cone cosine	subsection 4.9.4
	Beta[3]	Isotropy parameter	subsection 4.9.4
	cldirks	ClusFit recon. direction KS test	section 4.9
	bgoodness	BONSAI goodness of fit	section 4.9
*	*n18*	In time hits	section 4.9

Table 7.2: Variables selected for inclusion in BDT, based on trial $\frac{S}{\sqrt{B}}$ impact. Those not appearing in Table 7.1 are marked with an asterisk.

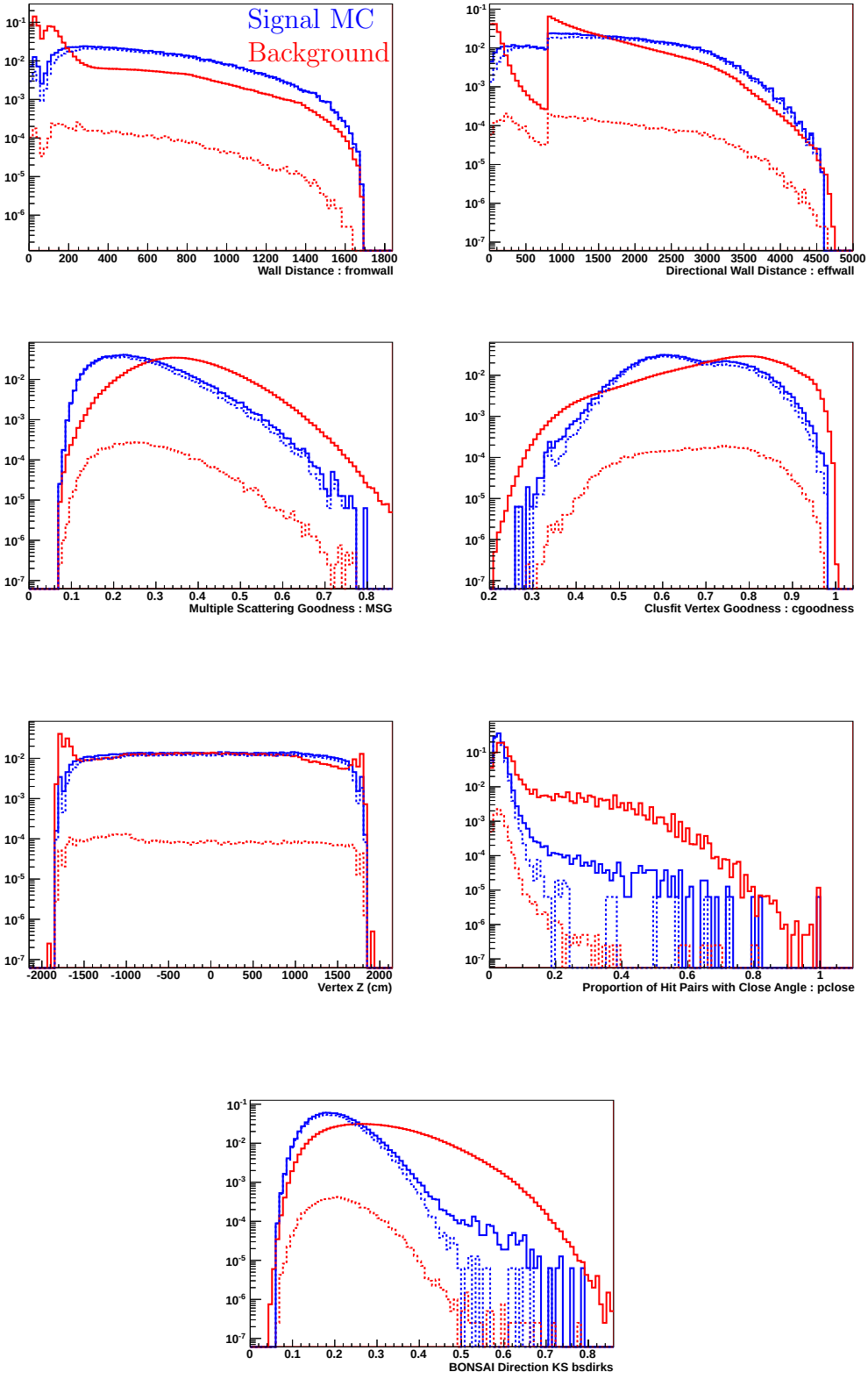


Figure 7.8: Variables (1-7) selected for inclusion in BDT. Solid lines show the full test sample, dashed shows only events with a BDT score >0, i.e. those likely to be selected.

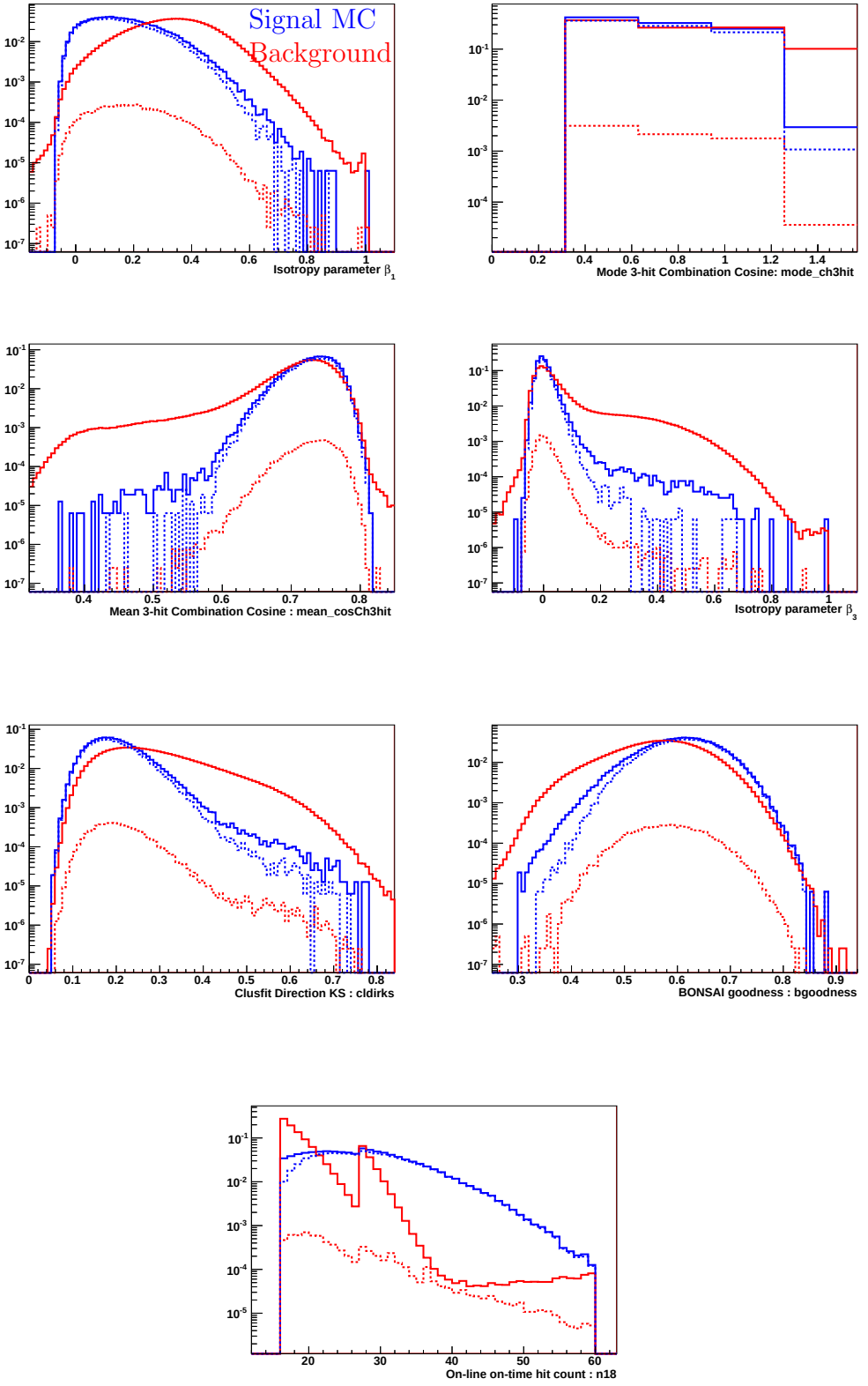


Figure 7.9: Variables (8-13) selected for inclusion in BDT. Solid lines show the full test sample, dashed shows only events with a BDT score >0, i.e. those likely to be selected.

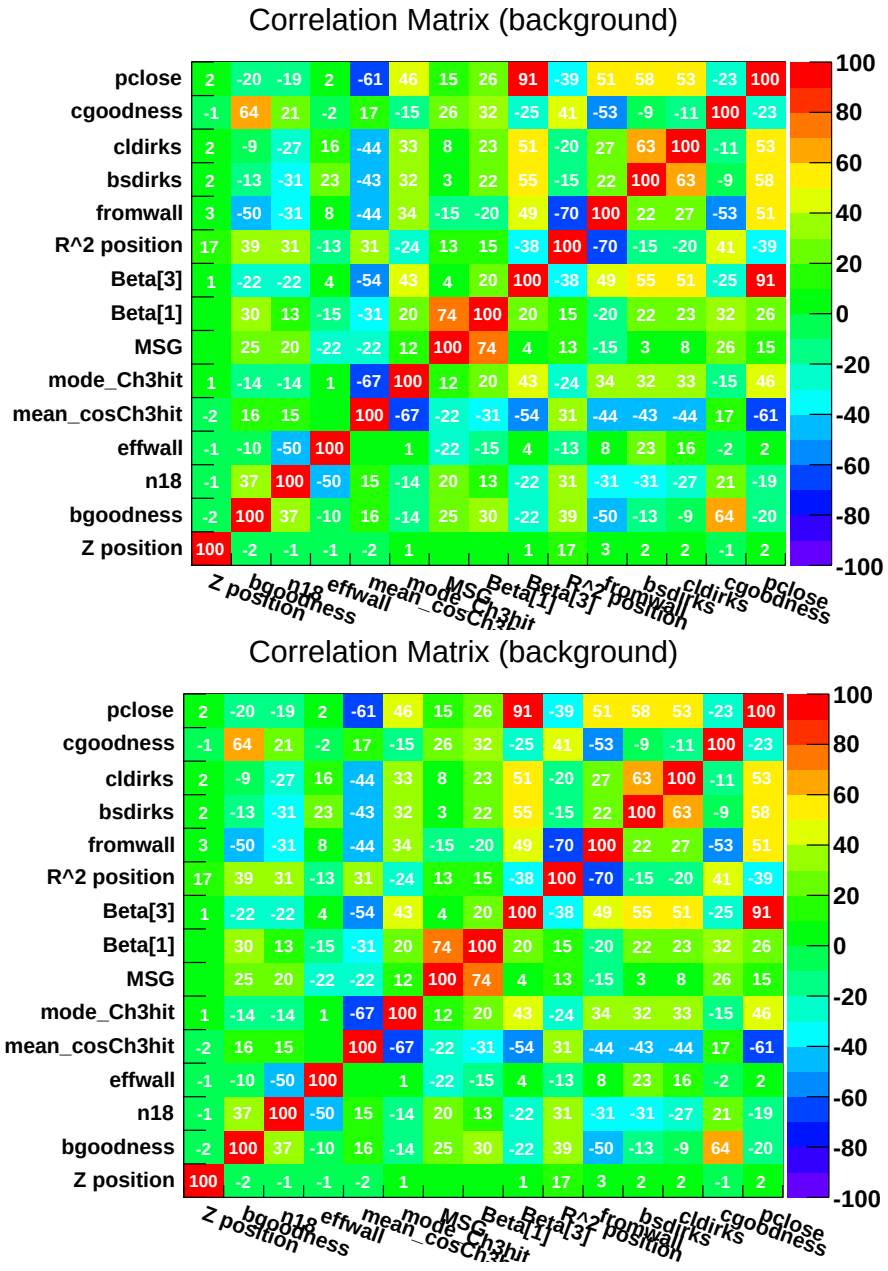


Figure 7.10: Correlation matrices for signal (above) and background (below) samples. Included are those variables in Table 7.2, plus radial position. Several variables are highly correlated or anti-correlated.

- *fromwall* - background events due to internal radioactivity often reconstruct close to the detector wall

- *effwall* - background events due to internal radioactivity often have reconstructed direction pointing towards the nearest PMT

- *MSG* - a measure of hit pattern, events which are more like the pattern produced by a single multiple scattered electron/positron have a high score. Signal has a low score, as TNC on GD produces multiple γ-rays.

- *cgoodness* - a measure of vertex goodness of fit. Some background events do not fit well due to being comprised of a high proportion of dark noise.

- *bz* - background is more likely to be found at the bottom of the detector due to the pattern of contamination

- *pclose* - a measure of hit pattern, background events are more likely to have hits that are close in angle to each other.

- *Beta[1]* - a measure of hit pattern. Events with a more isotropic distribution of hits has a score closer to 0. TNC on Gd produces a more isotropic hit pattern because it consists of multiple γ-raysemitted (it is assumed) isotropically.

- *mode_ch3hit* - the binned modal opening angle of 3 hit combinations. Background events are more likely to contain opening angles close to $\frac{\pi}{2}$.

- *mean_cosCh3hit* - the mean cosine opening angle of 3 hit combinations. Events where hits were produced by a Cherenkov emission will have cosine angles close to the Cherenkov angle. This is still true if there are multiple electrons/positrons emitting Cherenkov light, provided that each one produces enough hits. A similar method is used in the DSNB analysis to separate positrons from pions by their Cherenkov angles.

- *Beta[3]* - an isotropy parameter, see Beta[1]

- *cldirks* - KS test of the hit pattern against expected for single electron in reconstructed direction. TNC on GD has a lower score as it is comprised of multiple γ-rays.

- *bgoodness* - another measure of vertex goodness of fit, see cgoodness

- *n18* - number of selected on-time hits - background has a steeply falling energy distributionand therefore hit number distribution, although the distribution is distorted by the preselection cuts.

7.4.3 Performance

The BDT with the best performance was then evaluated on the rest of the background data-set, and on independent signal MC data-sets. The distribution of BDT scores is shown in Figure 7.11. The training and testing background data used earlier in this chapter comprise a 5% sub-set of the BG data-set. The signal MC samples were 10^6 events each before pre-selection, and were generated fully independently of the earlier training and test data-sets. The alternate signal MC model is that based on GLG4SIM, as described

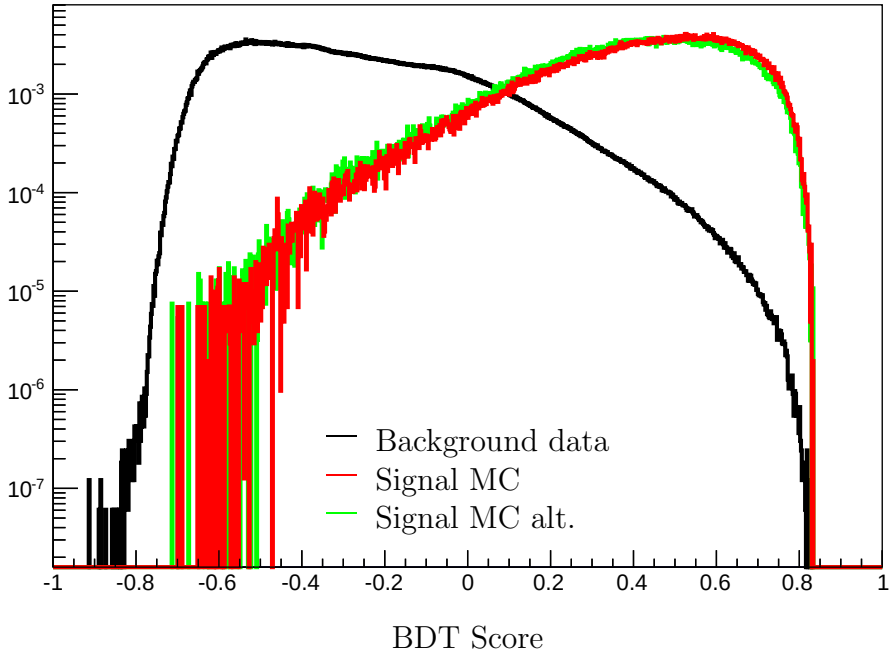


Figure 7.11: BDT scores evaluated on large datasets.

in chapter 5.

Much better performance is achieved using a BDT than is possible with rectangular cuts or a linear discriminant. Optimisation of the discriminator was much faster and more straightforward than if an ANN had been used. Performance is assessed in the context of pre-SN detection in chapter 8.

As can be seen in Figure 3.13, in the case of a pre-SN star at 200 pc, the expected rate of IBD reactions in 32 kt water would be on the order 500-1000 in 12 hours. In order for this to be observable, the background needs to be brought down to the same scale as the signal without reducing the signal too much. From the 1.3×10^7 events per hour collected by WIT, the target background level was $\sim$100 in 12 hours, and the total signal efficiency target $> 10\%$. As explained in chapter 6, the efficiency of the trigger conditions and

pre-selection for TNC on Gd is 58%, and pre-selection background reduction is a factor ~ 400. In order to achieve this, the background reduction factor target for the MVA was ~ 4000, with a signal efficiency target for the MVA $> 17\%$. Figure 7.12 shows the background rejection factor against signal efficiency for the BDT used and a LD with the same variables; it clearly shows that the target efficiency/background rejection is achievable with the BDT, but not with the LD.

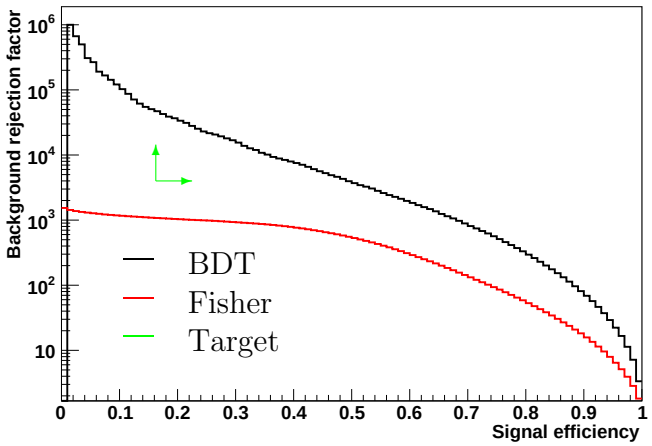


Figure 7.12: Background rejection factor against signal efficiency for final BDT and an LD using the same variables. Evaluated on a test sample independent of the training sample.

7.4.4 Variability

Runs within the background data sample are not totally consistent in their BDT response. There are some runs for which the SK detector was in an unusual configuration for test purposes. Noteably there is a period in which convection was deliberately created for calibration purposes. As radon is usually concentrated at the edges and bottom of the detector, convection

introduces radon into the FV. These periods stand out in event rate plots - there are many more events with higher BDT scores, as shown by Figure 7.13.

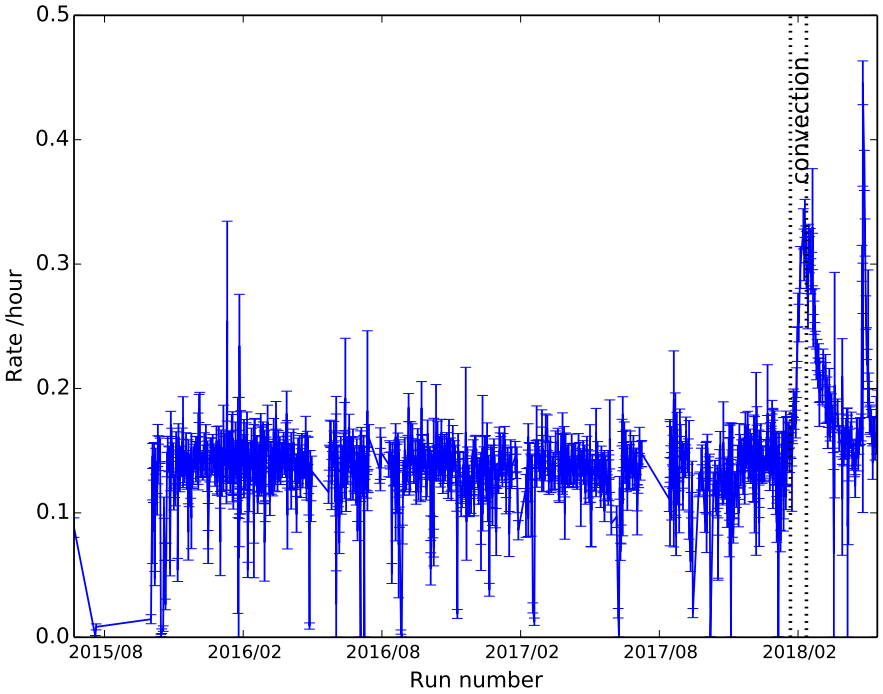


Figure 7.13: Variation in BDT response in background data sample. Plotted is the rate of events with BDT score > 0.56. The period in which convection was deliberately created is marked. There was also a period of water system experimentation at the end of SK-IV. Error bars show sample error based on $\sqrt{N}$ for each run. Other than this, the event rate is generally stable within expected statistical fluctuations.

Chapter 8

Sensitivity to Pre-SN Neutrinos

Using the response models developed in chapter 6 and chapter 7, the ability of SK-Gd to detect and identify pre-SN $\overline{\nu}_{\mathrm{e}}$ is evaluated in this chapter. In section 8.1, some of the practical aspects of implementation of a pre-SN alert are considered. Estimates made by other authors are discussed in section 8.2. The final selection of signal parameter space, using coincidence variables, the energy of the prompt event and the BDT score of the delayed event, was optimised as described in section 8.3. Detection strategy and figures of merit are considered in section 8.4. The final results of the study are given by section 8.5. Using simplified assumptions, these results are scaled up to the next generation of neutrino detectors in section 8.8. Event rates in the pure water data are examined as a time series in section 8.7, showing how event rate prediction might work in practice, and considering the effect of background integration time. The possibility of combining multiple neutrino detectors for increased range is considered in section 8.9.

8.1 Implementation

Firstly, although the majority of the necessary prerequisite modifications have been made to SK, gadolinium loading has not yet begun. The baseline assumption in this chapter is that SK will be loaded to 0.2% $Gd_2(SO_4)_3$ by mass. However, loading will first be to 0.02% $Gd_2(SO_4)_3$ loading by mass, meaning that 50%, rather than 90%, of neutrons will capture on gadolinium. Signal efficiency will therefore be lower during this initial phase, although any internal backgrounds coming from remaining radioisotope contamination of $Gd_2(SO_4)_3$ will be lower too. The higher loading level has been assumed for all of this chapter except section 8.6, which covers the results for a lower loading level.

This study assumed effective spallation reduction. Currently, spallation reduction is applied offline, at the point at which the data are being incorporated into an analysis. If spallation reduction is not applied online, then background from the products of spallation could become dominant in the coincidence channel.

In this study, it was assumed that the WIT triggering scheme and thresholds would be unchanged. However, efficiency for low energy prompt events could be improved by using relaxed trigger thresholds for events in coincidence, or simultaneous fitting of both parts of the DC event. The necessary online software and data pipeline has not yet been implemented.

Finally, the software that implements the pre-SN alert itself will need to be created and tested. The role of this software will be to interface with the online triggering computers, and receive a sub-set of events which are iden-

tified as being consistent with the low energy neutrino selection described in this study. This will mean event candidates which are high quality and likely to be neutron captures on Gd, and events which form the prompt part of a delayed coincidence with such events. The software will need to actively monitor background rates, and detect a significant increase in the candidate rate, accurately accounting for uncertainty, random fluctuation, and variability in the background rate. Some random and non-random fluctuations in the pure-water background data are investigated in section 8.7. An alert would then need to be automatically issued, giving easy to understand information. False alerts due to, e.g., calibration sources, or gaps in the background data, must be avoided. Consideration needs to be given to acceptable levels of false positive alerts and alarm efficiency.

8.2 Previous Estimates

Estimates of SK's ability to detect pre-SN neutrinos have been made previously by both astrophysicists and members of SK. The variation in the estimates is very large, with some predicting that SK will be able to confidently detect a pre-SN up to 2 kpc away, and others predicting that not even Betelgeuse going pre-SN could be detected with high confidence.

Assuming that geoneutrinos and reactor neutrinos form an irreducible background to pre-SN neutrinos, Patton et al [37] note that the greatest distance at which signal would exceed background in an ideal detector is 30 kpc. Assuming normal neutrino MO, a positron total energy threshold of 4.5 MeV, 100% efficiency and 22.5 kt FV, they predict 0.43(2.27) IBD

events at 1 kpc for a 15(25) $M_\odot$ progenitor, which corresponds to 10.8(56.8) events at 0.2 kpc. This estimate covers the entire pre-collapse period, and no background assumption is made.

In a 2004 paper, Odrzywolek et al. [49] estimated 41 IBD events per day during silicon burning at 1 kpc for SK, and gave a maximum range for SK-Gd of 2 kpc by assuming that 10 events per day are required for confident detection. Using the same assumption, plus some assumption about the distribution of the galaxy, for Hyper-K leads to an estimated 75% chance of detection in 20 years.

In his thesis, P. Fernandez-Menendez [88] made an estimate based on an integrated flux estimate by Odrzywolek, Misiaszek, and Kutschera [34]. A 3 MeV positron kinetic energy threshold, 11% efficiency based on the SK solar analysis, and 80% tagging efficiency are assumed. This leads to an expected number of events from a progenitor at 0.2 kpc of just 16.4. Background is estimated at 30 per day, so a 3 σ detection is not possible for even Betelgeuse (α Ori) by this estimate.

There are large discrepancies between these predictions. The study in this thesis should be more accurate and reliable than previous estimates, because it uses a detailed model of the efficiency and background at low energy in SK, and the full energy and time dependent information for multiple models of pre-SN $\overline{\nu}_e$ emission. Sensitivity is also evaluated in a more nuanced way, taking into account false positive rates, and producing sensitivity estimates for both maximum warning time and maximum detection range.

8.3 Final Selection

From the flux as a function of true neutrino energy and time, the expected rate of IBD reactions at SK-Gd are calculated. The effect of distance is simply a $1/R^2$ effect. The number of targets for IBD is the number of hydrogen nuclei in the SK ID. Detection efficiency is dependent on the energy of the positron, and energy resolution is taken into account with a smearing matrix calculated from detector simulation.

Starting from the detector response model developed in chapter 6, cuts were optimised to give the greatest range for efficient detection of a 25 $M_\odot$ pre-SN star using the model of [43] 0.1 hour before core collapse, assuming the more optimistic background and efficiency cases. The distribution of the variables used in the final selection of DC events is shown in Figure 8.1 for the two largest backgrounds in the most important variables. The cuts shown in Figure 8.1 are as follows: delayed candidate BDT score > 0, coincidence distance $< 300\ cm$, and coincidence time $< 100\ \mu s$. These cuts are justified as follows:

- Events with a higher BDT score are more like the model of TNC on Gd, according to the selection designed in chapter 7.

- Real coicidences are more likely to be close together in time and space.

. While the accidental backgrounds are well controlled by the combination of coincidence variables and the neutron BDT, the background from pairs of neutrons is harder to reduce. Selection of single neutrons was based mostly on the BDT classifier, with distributions in the final selection shown in Fig-

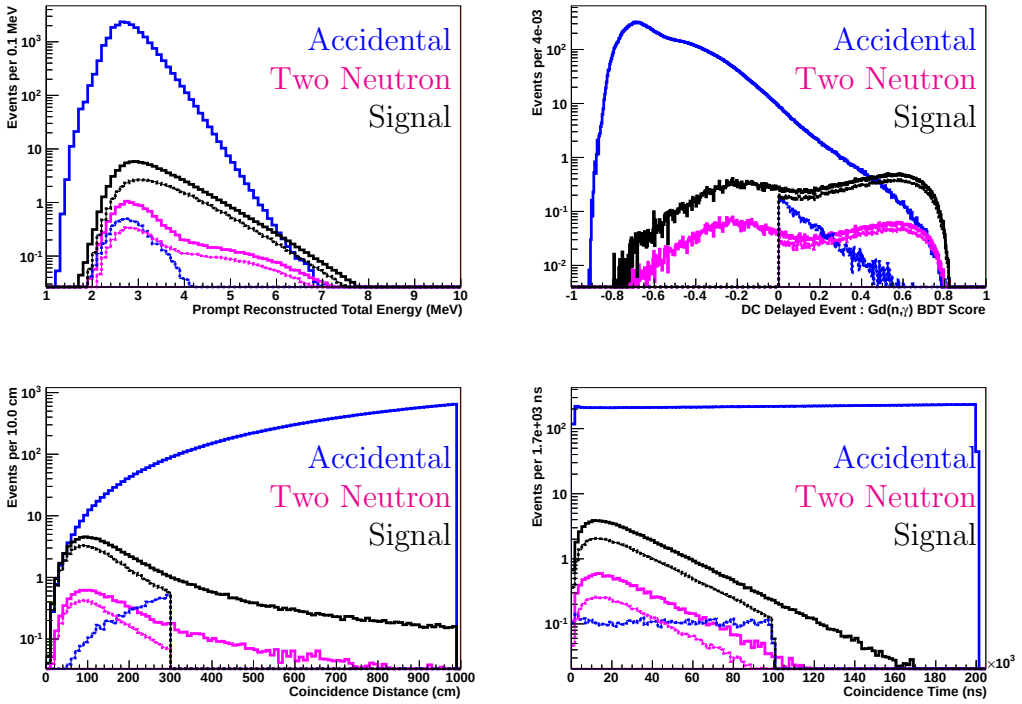


Figure 8.1: Distribution of DC channel variables in final selection for signal and largest backgrounds. Solid lines show before selection, dotted after. Background is normalised to 12 hours. Signal is normalised to the flux in the final 12 hours before CCSN for a 20 $M_\odot$ star at 500 pc.

ure 8.2. The cut on BDT score shown in Figure 8.2 keeps candidates with a score greater than 0.56.

Total signal trigger and selection efficiency depends on the energy distribution of the flux. In the final 12 hours before core collapse, the proportion of all IBD events which are triggered and selected is 4.3-6.7% for DC events, and 9.5-10% for neutron singles (upper and lower values depending on neutrino spectrum model). Using the alternative MC for the γ-rays from TNC on gadolinium, these numbers are 3.9-6.1% and 7.3-8.0% respectively. A range is given as these are flux averaged efficiencies, and therefore depend

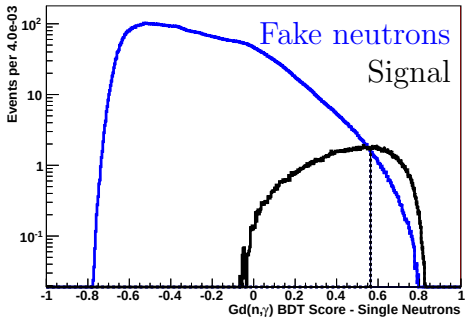


Figure 8.2: Distribution of single neutron channel variables in final selection for signal and largest background. Solid lines show before selection, with the dotted line showing the cut point. Background is normalised to 12 hours. Signal is normalised to the flux in the final 12 hours before CCSN for a 20 $M_{\odot}$ star at 500 pc. The distribution of the Gd BDT classifier is different from that shown in Figure 8.1 as single neutron events had a higher hit threshold applied in pre-selection. Events exceeding a score of 0.56 are kept.

on the flux spectrum. The selection requirements on the DC time, and the positron quality requirements, are very efficient for signal. DC signal efficiency is lower at low energies due to the lower trigger efficiencies, and worse vertex reconstruction leading to increased DC distance. Figure 8.3 shows the total efficiency for DC events against the true positron energy. The efficiency for selecting TNC on Gd does not depend on the true positron energy. Note that this efficiency curve has been directly optimised for detecting the pre-SN flux in the final 12 hours, so should not be used in higher energy contexts. It should not be alarming that this efficiency is lower and these backgrounds higher than are typically quoted for other SK analyses (such as the SN relic neutrino analysis), which are at higher energy. At higher energy, reconstruction is much better, and backgrounds much lower. Almost all prompt events in this analysis reconstruct below the energy threshold of any other analysis at SK. If the TNCs were only on H, rather than Gd, there

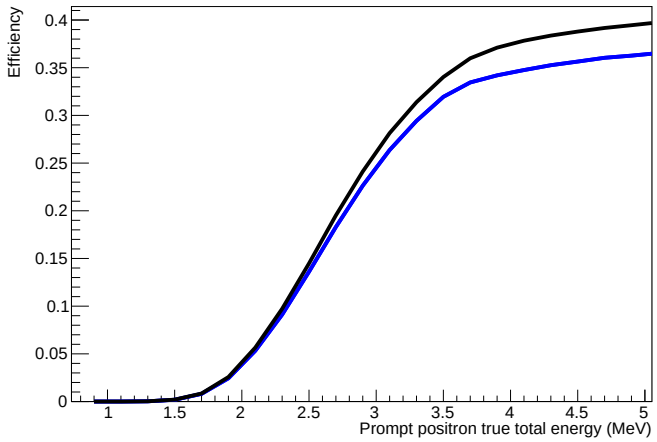


Figure 8.3: Trigger and selection efficiency for DC events against prompt positron true total energy. Above 4 MeV positrons are efficiently triggered and reconstructed, and so the efficiency is determined by the triggering and selection of the delayed part of the event. The result with the alternative Gd γ-ray-cascade model is shown in blue.

would be no sensitivity at all in this analysis.

Remaining backgrounds for single neutrons, dominated by fake neutrons from the intrinsic radioactivity of the detector, total 66-140 per 12 hour window. For DC events, remaining backgrounds are 5 to 11 accidental, 0.3 to 0.4 from SF γ-rays in coincidence with neutrons, 12 to 25 from pairs of neutrons, 0.2 to 3.0 from reactor and geo neutrinos; in total 17 to 39 per 12 hour window.

8.4 Detection Strategy

The simplest way of searching for a rapid excursion in the candidate event rate is to define some signal time window (e.g. 12 hours), and background window (e.g. 30 days), then perform a hypothesis test. The null hypothesis

is that the observed rate in the signal window is consistent with the observed rate in the background window, taking into account Poissonian fluctuations. The alternative hypothesis is simply that the rate in the signal window is higher than that in the background window. A Poisson likelihood for the null hypothesis is calculated for the total detected event rate, combining both the DC and single neutron channels.

The DC background is expected to be highly correlated with the single neutron background. Therefore, the likelihood calculation cannot assume that the two channels are independent. The rates of the two channels are simply added together into a single bin. If the channels were independent, then a much greater range might be achieved, as the null hypothesis likelihood of both channels having an upward fluctuation would be lower. However, if the channels are assumed to be independent when they are not, then the false positive rate would be higher than expected.

The time from the start of a data block for reconstruction, conversion to offline data format, data reduction, and hypothesis testing will be around 10 minutes. This sets an estimated typical latency for an alarm.

The length of the signal window should be similar to the timescale over which the event rate would change if a pre-SN star was detected. The choice of signal window size can have a dramatic effect on the sensitivity of the analysis, as it affects the statistical fluctuations, the background level, and the trial factor. A number of window sizes, from 1-48 hours, were tested (see Figure 8.4), and the 12 hour signal window was chosen. For the model used, the $\overline{\nu}_{\mathrm{e}}$ flux multiplied by the IBD cross section, integrated over the final 12 hours before collapse is summarised in Table 8.1.

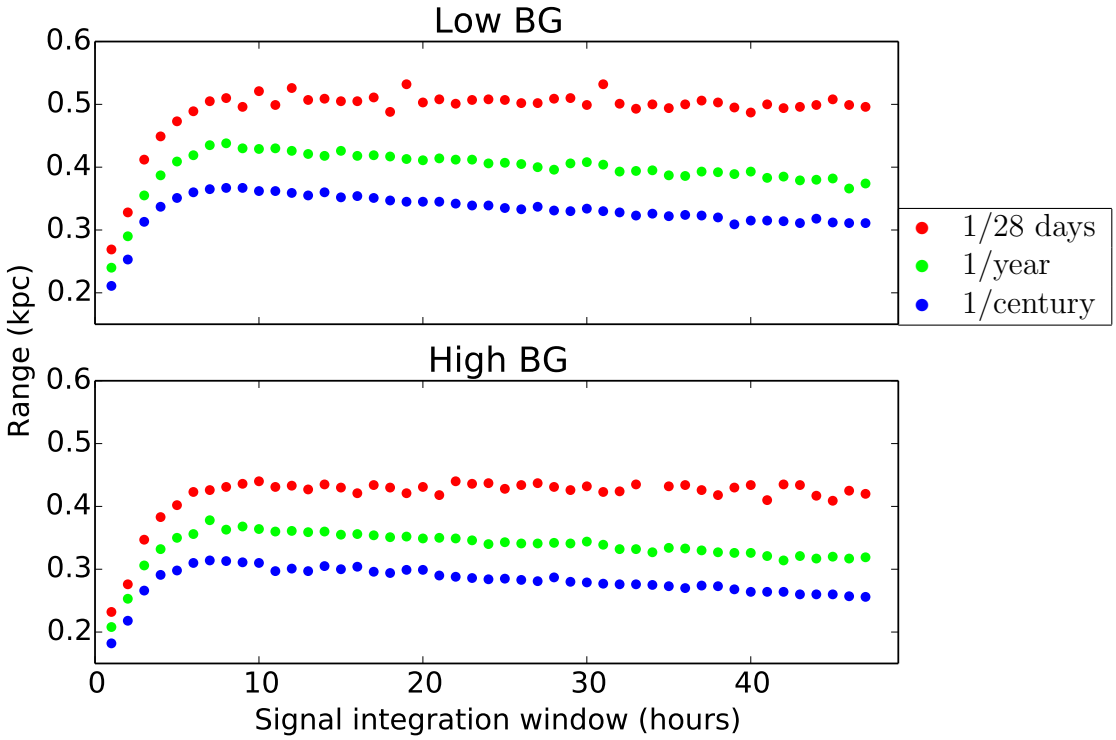


Figure 8.4: Maximum range of detection against signal window size, for different FPR and background case. The window size chosen was 12 hours.

MO	Mass ($M_\odot$) ($M_\odot$)	Model	IBDs in final 12 hours 10^{12} cm^2 per nucleon	in 32 kton at 200 pc
NO	15	Odrzywołek	1.6	1.4×10^3
	15	Patton	1.9	1.7×10^3
	25	Odrzywołek	3.3	3.0×10^3
	30	Patton	3.8	3.4×10^3
IO	15	Odrzywołek	0.44	3.9×10^2
	15	Patton	0.53	4.7×10^2
	25	Odrzywołek	0.93	8.3×10^2
	30	Patton	1.2	1.1×10^3

Table 8.1: Anti-electron neutrino flux multiplied by IBD cross section for models considered.

A longer background window would always be better due to reduced uncertainty in the background rate, however the background rate may change slowly over time. A gradual change might be expected, due to the gradual increase in PMT gain, seasonal variations in the radon concentration in the mine air ([116, 72]), changes in water flow affecting radon activity in the FV, or changes in nearby nuclear power station activity. In this study it is assumed that the background level is known precisely when the signal is detected. The effect of background window length is examined in pure-water SK-IV data in section 8.7.

These methods are chosen for the purpose of benchmarking performance. In practice, greater sensitivity can be achieved by properly accounting for the likelihood of the event rate across separate bins, and by assuming a more complicated alternative hypothesis, for example by calculating the rate of increase of the candidate event rate. Furthermore, models of how backgrounds vary with time, have measurement uncertainty, and have correlated bins, should be included when a large enough background sample has been collected during SK-Gd.

In attempting to get a SN early warning from the detection of pre-SN neutrinos, there are four variables which together describe a detector's performance.

1. Alarm efficiency, i.e. the probability of correctly detecting a true pre-SN

2. false positive rate (FPR)

3. Expected time of early warning that the detector would provide

4. Expected distance to which the warning would be efficient

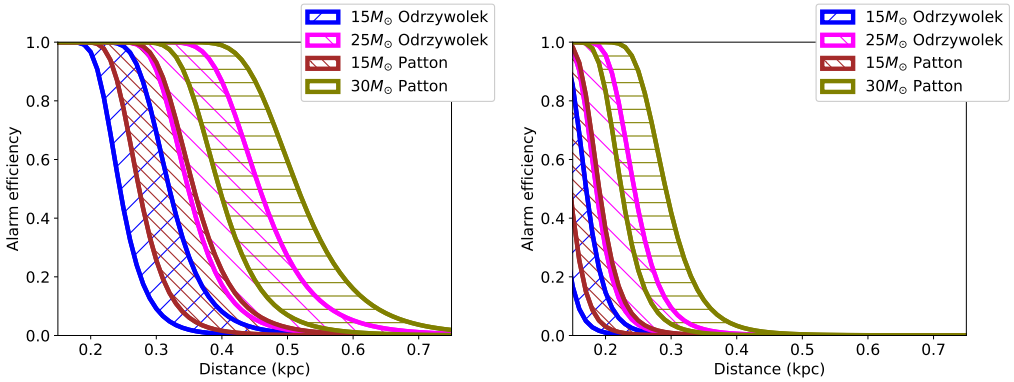
Tolerating a higher FPR would allow for greater range and more warning, but would reduce confidence in the warning system; a choice needs to be made on what FPR is acceptable. Note that a SN within 1 kpc is a rare occurence - on the order of 1 in 10,000 years based on historical data [46]. FPR levels shown in this study are 1 per year and 1 per century (cy.), and are assumed to be set by Poisson fluctuations only. Range is defined as the point at which alarm efficiency is 50%. By formulating the problem in terms of FPR, a trials factor is incorporated.

8.5 Baseline Results

Figure 8.5 shows the distance to the pre-SN star at which the null hypothesis would be rejected before core collapse. Figure 8.6 shows the largest amount of time before core collapse at which a pre-SN is expected to be detected. The width of the bands shows uncertainty due to levels of background and the difference between models of γ-ray emission from TNC on Gd. The distances at which alarm efficiency is above 50% are summarised in Table 8.2.

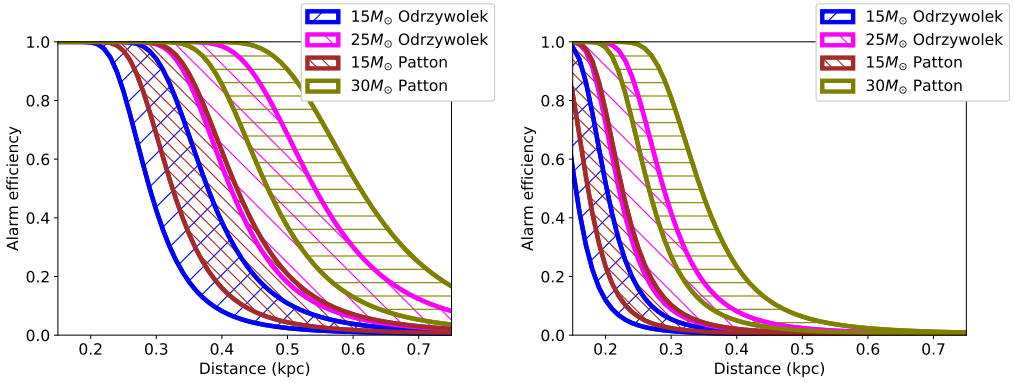
Results depend on the neutrino MO (normal *NO* or inverted *IO*), the ZAMS mass of the star, the distance to the star, and the background level in SK-Gd. Questions of detector model uncertainty will be resolved by in-situ measurements once SK-Gd is loaded. An inverted neutrino MO is detrimental to this analysis as it reduces the $\overline{\nu}_{\mathrm{e}}$ fraction of the pre-SN flux.

Discussions of pre-SN stars often focus on α Ori (Betelgeuse) as an example of a nearby massive star, although α-Sco(Antares) has a similar mass



(a) NO, FPR=1/cy.

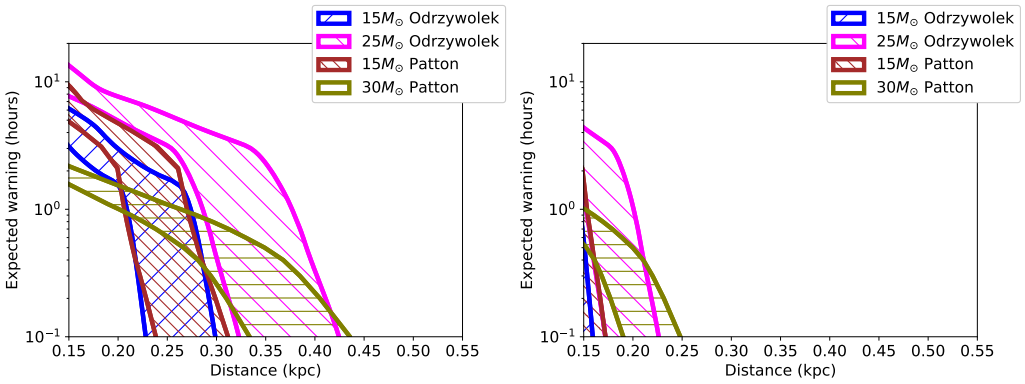
(b) IO, FPR=1/cy.



(c) NO, FPR=1/year

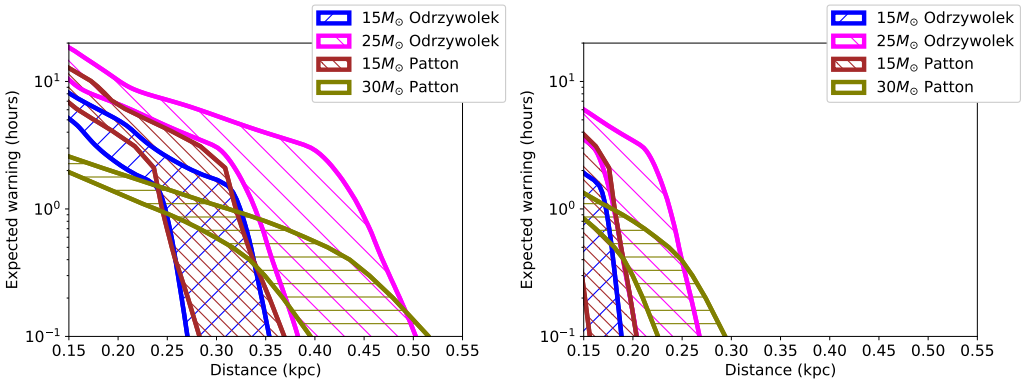
(d) IO, FPR=1/year

Figure 8.5: Expected maximum range of detection in the final 12 hours before collapse, for 15 $M_\odot$ and 25 $M_\odot$ stars. The width of the bands shows uncertainty due to levels of background in SK-Gd, and the difference between models of γ-ray emission from TNC on Gd.



(a) NO, FPR=1/cy.

(b) IO, FPR=1/cy.



(c) NO, FPR=1/year

(d) IO, FPR=1/year

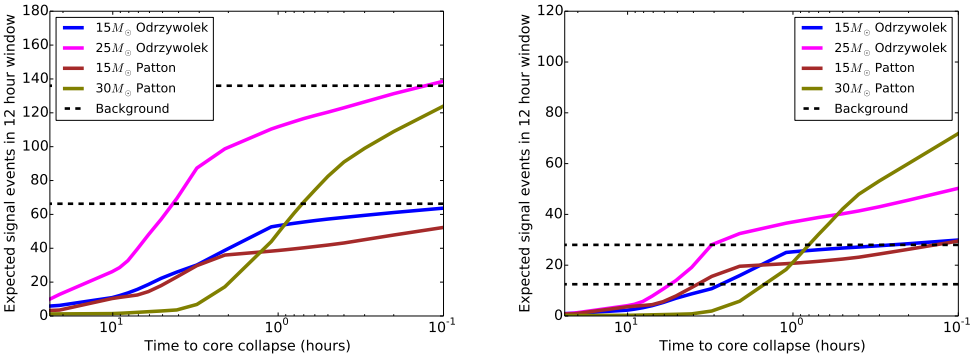
Figure 8.6: Expected early warning against range of detection, for 15 $M_\odot$ and 25 $M_\odot$ stars. The range is defined as the largest distance at which probability of detection is greater than 50%.

	Mass ($M_\odot$)	Model	Max. range (pc) given FPR 1/year	Max. range (pc) given FPR 1/cy.
NO	15	Odrzywolek	300 - 400	250 - 300
	15	Patton	420 - 600	360 - 500
	25	Odrzywolek	330 - 400	280 - 400
	30	Patton	480 - 600	410 - 500
IO	15	Odrzywolek	160 - 200	130 - 200
	15	Patton	220 - 300	190 - 200
	25	Odrzywolek	180 - 200	150 - 200
	30	Patton	270 - 400	230 - 300

Table 8.2: Maximum range of detection under various assumptions. Detection range is defined to be the highest distance at which alarm efficiency is greater than 50%. Uncertainty comes from TNC γ-ray model, and background uncertainty. The same information is contained in Figure 8.5.

and distance. For the purpose of this study α Ori is assumed to be 200 pc from Earth, with a mass between 15 and 25 $M_\odot$. Estimates of Betelgeuse's mass are correlated with its distance ([117]), so two extremes chosen for benchmarking performance are that it is 150 pc away and 15 $M_\odot$, or 250 pc away and 25 $M_\odot$. These values are chosen for comparison to [44], rather than to match the most up-to-date precise estimates of α Ori's distance and mass. Figure 8.7 shows the expected number of detected events at SK-Gd under these assumptions, after detection efficiencies are taken into account. The model with 30 $M_\odot$ is also included for the sake of comparison. The expected number of detected events in the final 12 hours before collapse are summarised in Table 8.3, and the expected amount of warning is summarised in Table 8.4.

The KamLAND collaboration published an analysis of its own sensitivity to pre-SN neutrinos [44], which is compared to the expected sensitivity of SK-



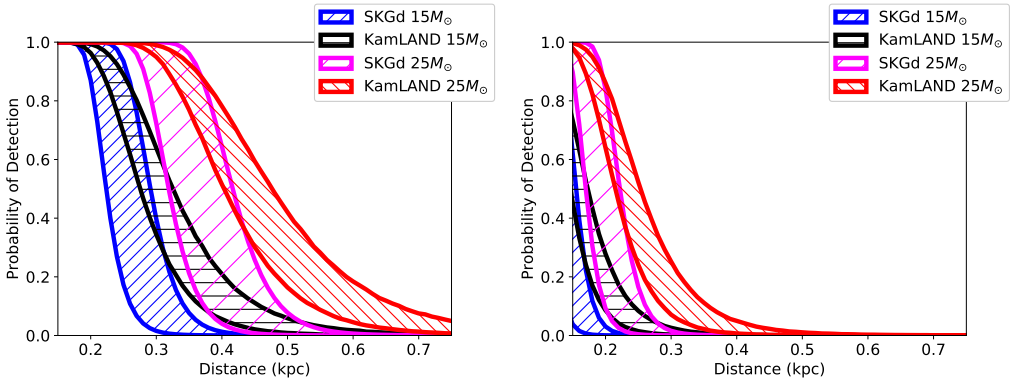
(a) Neutron singles expected signal rate

(b) DC expected signal rate

Figure 8.7: Expected signal events in 12 hour time window, after detection efficiencies are taken into account as per chapter 4. A distance of 200 pc and NO is assumed. Two background levels are shown in line with the range of background estimates in section 8.3, with uncertainty mainly in the future internal decay-chain contamination of SK-Gd.

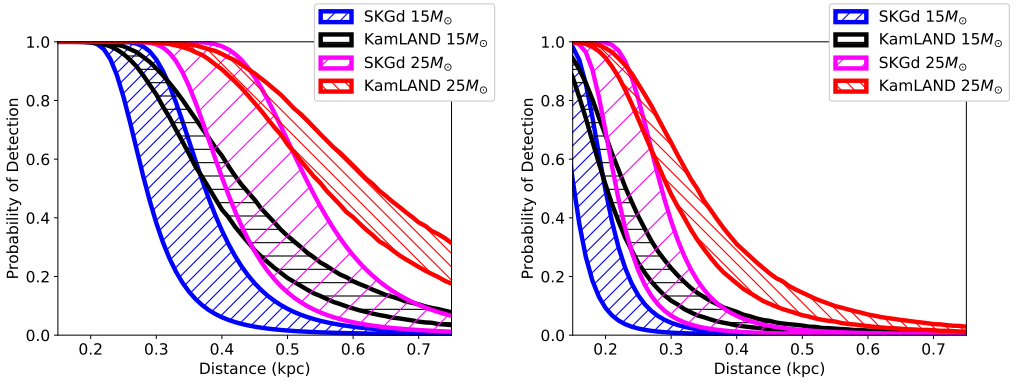
	Model	Mass ($M_\odot$)	Single neutrons	DC
NO	Odrzywolek	15	55 - 71	33 - 36
	Patton	15	65 - 84	45 - 50
	Odrzywolek	25	120 - 160	59 - 65
	Patton	30	130 - 170	100 - 110
IO	Odrzywolek	15	16 - 20	9 - 10
	Patton	15	18 - 23	13 - 15
	Odrzywolek	25	34 - 44	17 - 18
	Patton	30	40 - 52	34 - 37

Table 8.3: Expected numbers of events at 200 kpc in the final 12 hours before collapse at SK-Gd. Uncertainty comes from TNC γ-ray model only.



(a) NO, 5 σ/48 hours FPR equivalent

(b) IO, 5 σ/48 hours FPR equivalent



(c) NO, 3 σ/48 hours FPR equivalent

(d) IO, 3 σ/48 hours FPR equivalent

Figure 8.8: As Figure 8.5, but with reference numbers for KamLAND included. The FPR is fixed at the equivalent of 5 σ/3 σ with a trial factor of 1 per 48 hours. Differences in expected alarm latency are not taken into account. pre-SN models shown are those of Odrzywołeket al.

MO	Mass ($M_\odot$)	Model	Assumed distance (pc)	Warning (hours) given FPR 1/year	1/cy.
NO	15	Odrzywolek	150	5.3 - 8.4	3.4 - 6.3
	15	Patton	150	7.1 - 14.1	5.1 - 9.8
	25	Odrzywolek	250	4.7 - 7.4	3.3 - 5.7
	30	Patton	250	1.0 - 1.6	0.7 - 1.1
IO	15	Odrzywolek	150	0.1 - 2.0	0.0 - 0.8
	15	Patton	150	0.3 - 4.1	0.0 - 2.2
	25	Odrzywolek	250	0.0 - 0.6	0.0 - 0.0
	30	Patton	250	0.1 - 0.4	0.0 - 0.1

Table 8.4: Time at which expected signal exceeds threshold, for some assumptions chosen to represent Betelgeuse. $30M_\odot$ at 250 pc is far from the range of mass estimates for Betelgeuse, but is provided anyway for comparison. Uncertainty comes from TNC γ-ray model, and background uncertainty.

Gd. KamLAND is a liquid scintillator detector based in the same mine as SK. It has lower energy thresholds than SK, and so would detect IBD events from a pre-SN more efficiently, and has lower background rates. However, the mass of SK is more than 20 times larger than that of KamLAND, so more events are seen in total.

The nominal performance of KamLAND is taken from [44]. KamLAND background rates are 0.071-0.355 events per day depending on Japanese nuclear reactor power. Events are integrated over a 48 hour sliding window each 15 minutes. Assumed signal rates in the final 48 hours at 200 pc are 25.7(7.28) in the 25 $M_\odot$ case, 12.0(3.38) in the 15 $M_\odot$ case, for the NO(IO) case. The pre-SN models used were those of [43]. Not enough information is provided in [44] to directly and fairly compare warning times.

Figure 8.8 shows the distance to the pre-SN star at which the null hypothesis would be rejected before core collapse (t=0). The estimated range

for KamLAND is also shown. KamLAND has a latency of 25 minutes, which is not taken into account. The FPR is set to match that of the 3 σ and 5 σ with a 48 hour signal window used by KamLAND, for the sake of comparison. That is, the FPR is set to $\frac{1}{370}$ per 48 hours (approximately 1 per 2 years) for 3 σ and $\frac{1}{1744278}$ per 48 hours (approximately 1 per 10^5 years) for 5 σ. By this comparison, the maximum detection range of SK-Gd is slightly shorter than that of KamLAND.

Note that in low energy IBD, the direction of the incoming $\overline{\nu}_e$ cannot be reconstructed from the direction of the emitted positron [21], and the number of elastic scattering events will be small for a pre-SN, so this technique will not have any SN pointing ability. The direction of neutron travel cannot be resolved in SK, so the positron-neutron vector cannot be used to infer the $\overline{\nu}_e$ direction either.

8.6 Low Loading Case

The calculations in section 8.5 were repeated assuming that SK would be loaded to 0.02% gadolinium sulfate. As the additional background was assumed to come from decay chain isotope contamination of gadolinium sulfate, the intrinsic backgrounds are assumed to increase by only 10% in the high background case, rather than 100%. Final cut optimisation was re-processed, as looser cuts are expected to be favoured. Results are shown for expected warning time (Table 8.5) and range (Table 8.6 and Figure 8.9). In the interest of brevity, only the headline results are shown.

Compared to the 0.2% gadolinium sulfate loading case, the range and

warning time are reduced, but pre-SN neutrino emission could still be observed in a very nearby star such as α Ori provided the neutrino MO is normal. The most optimistic detection range is decreased from 600 pc to 400 pc, and the most optimistic warning time for α Ori is decreased from 14.1 to 5.9 hours (1/year FPR, 15 $M_\odot$ Patton et al., low background case; compare Table 8.5 and Table 8.4).

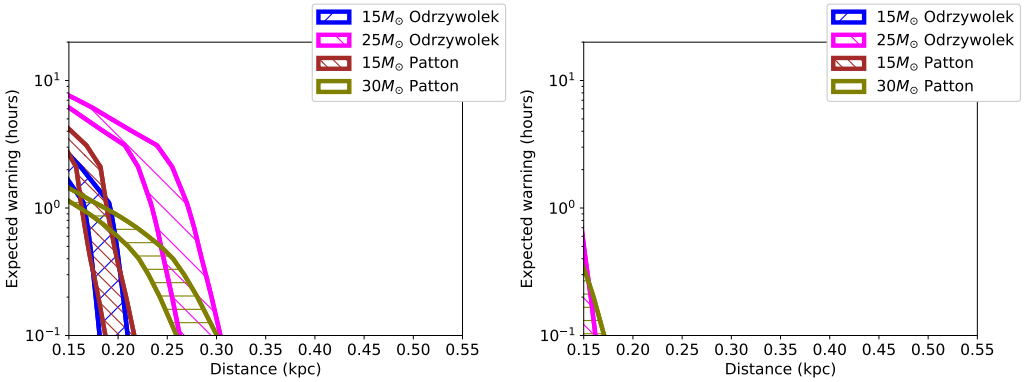
MO	Mass ($M_\odot$)	Model	Assumed distance (pc)	Warning (hours) given FPR 1/year	1/cy.
NO	15	Odrzywolek	150	2.8 - 4.5	1.7 - 2.7
	15	Patton	150	4.4 - 5.9	2.7 - 4.2
	25	Odrzywolek	250	2.8 - 4.1	0.3 - 2.4
	30	Patton	250	0.5 - 0.8	0.2 - 0.4

Table 8.5: As Table 8.4, but for the low (0.02%) gadolinium loading case. In this case if the neutrino MO is inverted no warning is expected. Time at which expected signal exceeds threshold, for some assumptions chosen to represent Betelgeuse. $30M_\odot$ at 250 pc is far from the range of mass estimates for Betelgeuse, but is provided anyway for comparison. Uncertainty comes from TNC γ-ray model, and background uncertainty.

8.7 Stability of Event Rate

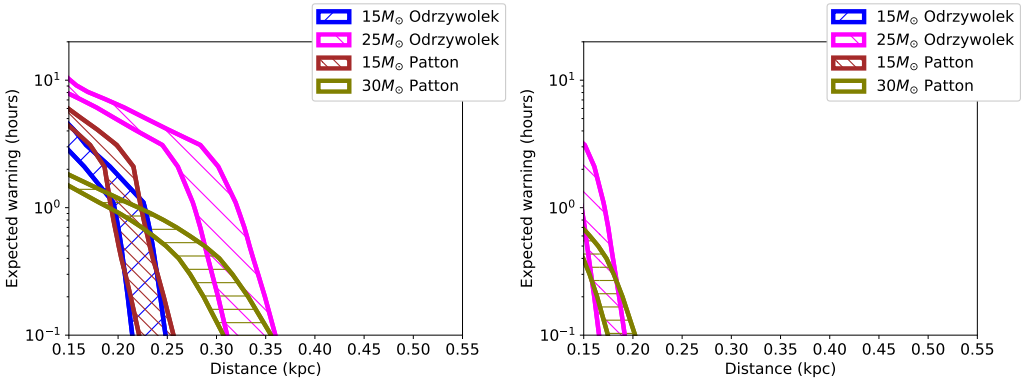
In this section the assumption that fluctuations in the event rate are Poissonian is examined more closely. This will need to be done again in more detail once gadolinium is loaded.

Only the pure-water SK-IV background data sample was considered; none of the events are truly TNC on Gd. Some runs had to be removed as the length of the run appeared to be incorrectly calculated and there was not time to debug this particular issue. The convection period was initially excluded



(a) NO, FPR=1/cy.

(b) IO, FPR=1/cy.



(c) NO, FPR=1/year

(d) IO, FPR=1/year

Figure 8.9: As Figure 8.6, but for the low (0.02%) gadolinium loading case. Expected early warning against range of detection, for 15 $M_\odot$ and 25 $M_\odot$ stars. Detection range is defined as the largest distance at which probability of detection is greater than 50%.

	Mass ($M_\odot$)	Model	Max. range (pc) given FPR 1/year	1/cy.
NO	15	Odrzywolek	230 - 300	190 - 200
	25	Odrzywolek	330 - 400	280 - 300
	15	Patton	250 - 300	210 - 200
	30	Patton	360 - 400	300 - 300
IO	15	Odrzywolek	120 - 100	100 - 100
	25	Odrzywolek	180 - 200	150 - 200
	15	Patton	130 - 200	110 - 100
	30	Patton	200 - 200	170 - 200

Table 8.6: As Table 8.2, but for the low (0.02%) gadolinium loading case. Maximum range of detection under various assumptions. Range is assumed to be the highest distance at which alarm efficiency is greater than 50%. Uncertainty comes from TNC γ-ray model, and background uncertainty.

(see subsection 7.4.4). The average rate of events with a passing BDT score are treated as a time series. A one-sided likelihood was calculated for each signal window. The mean of the distribution was assumed to be set by the mean of the event rate in the background window.

From a set of event counts C, live times L for a set of time periods, the predicted count rate K_{i+1} for the next time period $i+1$ is assumed to be the moving average of the count rate in the previous N time periods, scaled to by the live time

$$K_{i+1} = \frac{L_{i+1}}{N} \times \sum_{j=i-N}^{i} \frac{C_j}{L_j}. \tag{8.1}$$

The predicted standard deviation S_i of the predicted count is assumed to be due to Poissonian fluctuations on both the signal and background windows:

$$S_{i+1} = K_{i+1} \times \sqrt{\frac{1}{K_{i+1}} + \frac{1}{\sum_{j=i-N}^{i} C_j}} \tag{8.2}$$

If these assumptions are a good model for the variation in measurements of the background rate, then one would expect the residuals divided by the expected standard deviation

$$D_i = \frac{(K_i - C_i)}{S_i} \tag{8.3}$$

to have a Gaussian distribution with mean 0, standard deviation 1.

Equations 8.3 is tested in Figure 8.10, in which the residual D_i (equation 8.3) is plotted, assuming a 30 day rolling background window. Agreement is generally good when visually compared with a standard Gaussian. There appears to be an upward bias in the predictions K, producing more outliers at the negative end; this could be explained by the approximation of the Poisson distribution as Gaussian with slightly too low statistics, as the Poisson distribution has a longer positive tail, producing a negative tail in D_i. When outliers $> 3\sigma$ are excluded, the standard deviation of the residuals D_i is 1.1, the mean is 0.12, and the median is 0.14.

In Figure 8.11, the effect of the size of the background window is tested by varying the background integration window and plotting the mean and standard deviation of the residual (D_i, Equation 8.3). Outliers were not excluded from the calculation. Agreement was best when the background integration window was between roughly 5-40 days.

When the data collected during deliberate convection are included, very small likelihoods are produced (shown in Figure 8.12 and Figure 8.13). This is as expected, as convection introduces radioactive backgrounds into the FV.

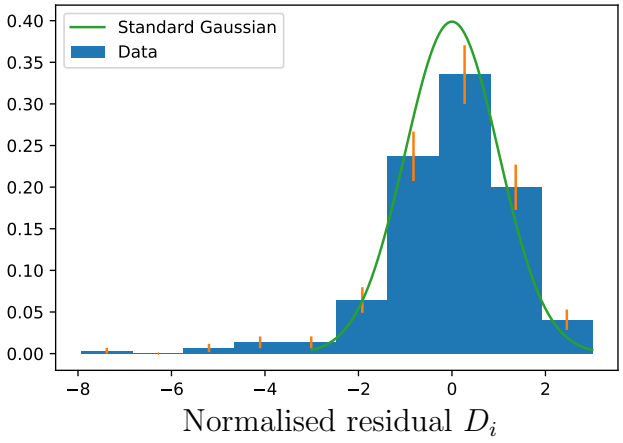


Figure 8.10: Residuals of data compared to preidction divided by the expected standard deviation. (D_i, equation 8.3)

8.8 Next Generation Detectors

Hyper-Kamiokande (HK) is a planned successor to Super-Kamiokande which will begin construction in 2020, with data taking expected to begin in 2027. Like SK, HK will be a water-Cherenkov detector. HK has multiple goals, including precise measurements of the leptonic CP violating phase, $sin^2\theta_{23}$ and Δm^2_{32} using an upgraded neutrino beam from J-PARC, extending the search for proton decay, as well as improved solar and atmospheric neutrino measurements and astrophysical goals such as improved SN neutrino detection capability [118]. The dimensions of each tank (Figure 8.14) will be such that the FV of HK will be 8.4× that of SK, with plans to build two tanks. Official plans for HK do not currently include gadolinium loading, but if SK-Gd is sucessful there would be a strong incentive to do so, as all of the same benefits apply. If HK were gadolinium loaded, it could be a powerful pre-SN detector.

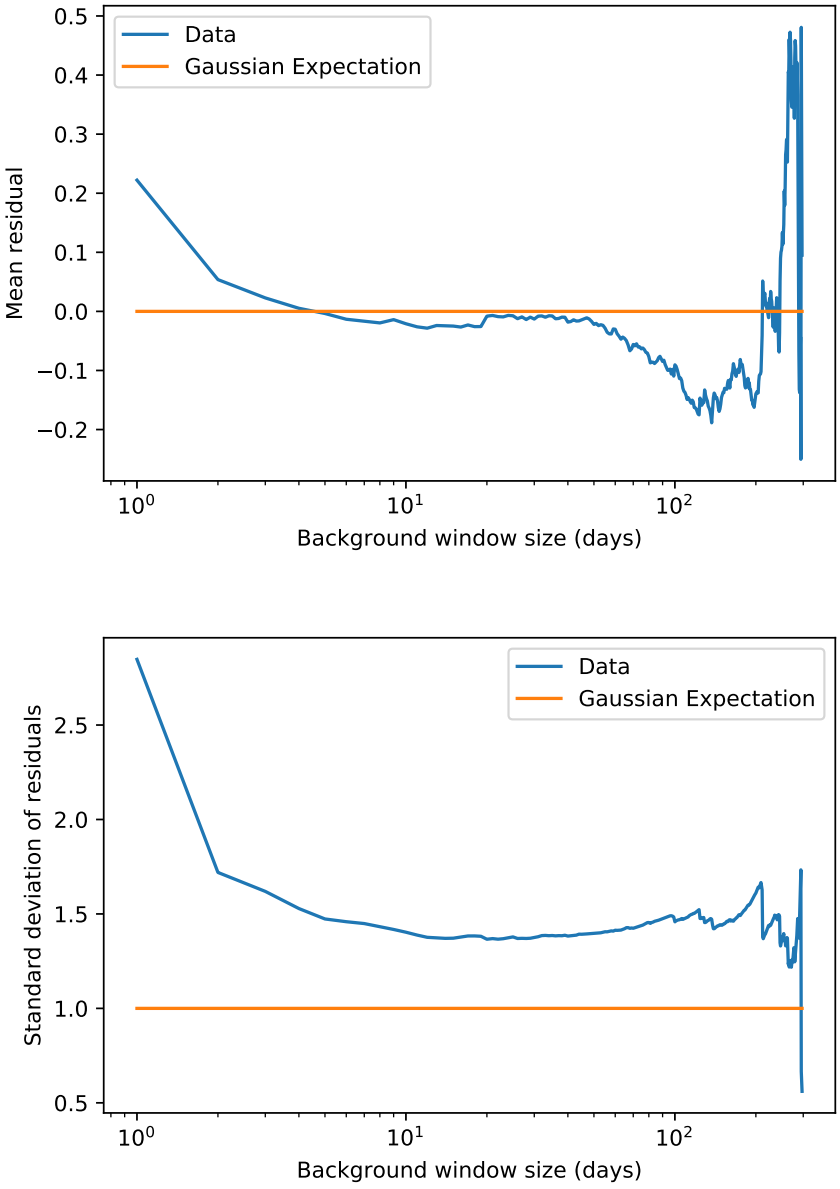


Figure 8.11: Effect of background window size on bias and accuracy of the event rate predictions. The background integration window is varied in size between 1 day and the maximum size possible. The mean (above) and standard deviation (below) of the residual (D_i, Equation 8.3) are plotted, along with the expectations if a Gaussian were a good model.

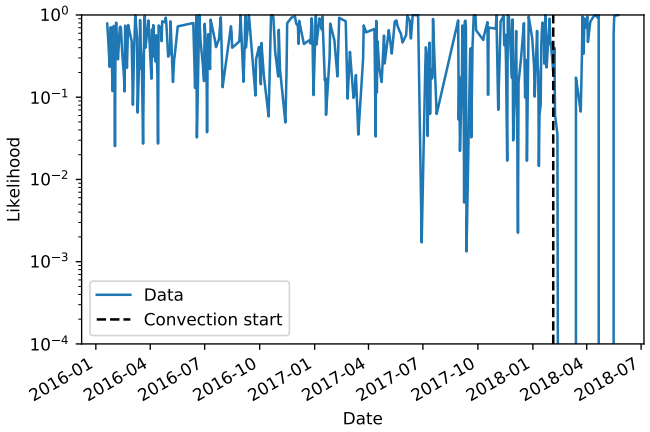


Figure 8.12: Gaussian one-sided likelihood of D_i assuming a Gaussian distribution, including period of deliberate convection, plotted against date. Points with low likelihood in 2017 may be due to gaps in the event data not properly accounted for in the run lengths.

Jiangmen Underground Neutrino Observatory (JUNO) is a proposed liquid scintillator detector with a mass of 20 kt [119]. The main motivation is the resolution of the neutrino mass ordering, and precise measurement of neutrino mixing parameters, using reactor $\overline{\nu}_e$. JUNO also has the potential to detect large numbers of pre-SN $\overline{\nu}_e$.

The simplest possible estimates of the range of detection for these next generation neutrino experiments were produced by assuming the only difference is the target mass. The problems with this assumption are obvious, but the approach provides some preliminary estimates without much difficulty. Background from internal contamination for HK was assumed to be at the lower end of the mass adjusted estimate used for SK-Gd. The higher flux case was assumed for reactor neutrinos. No uncertainty range is used for the backgrounds, as there is no reason to think they are particularly accurate.

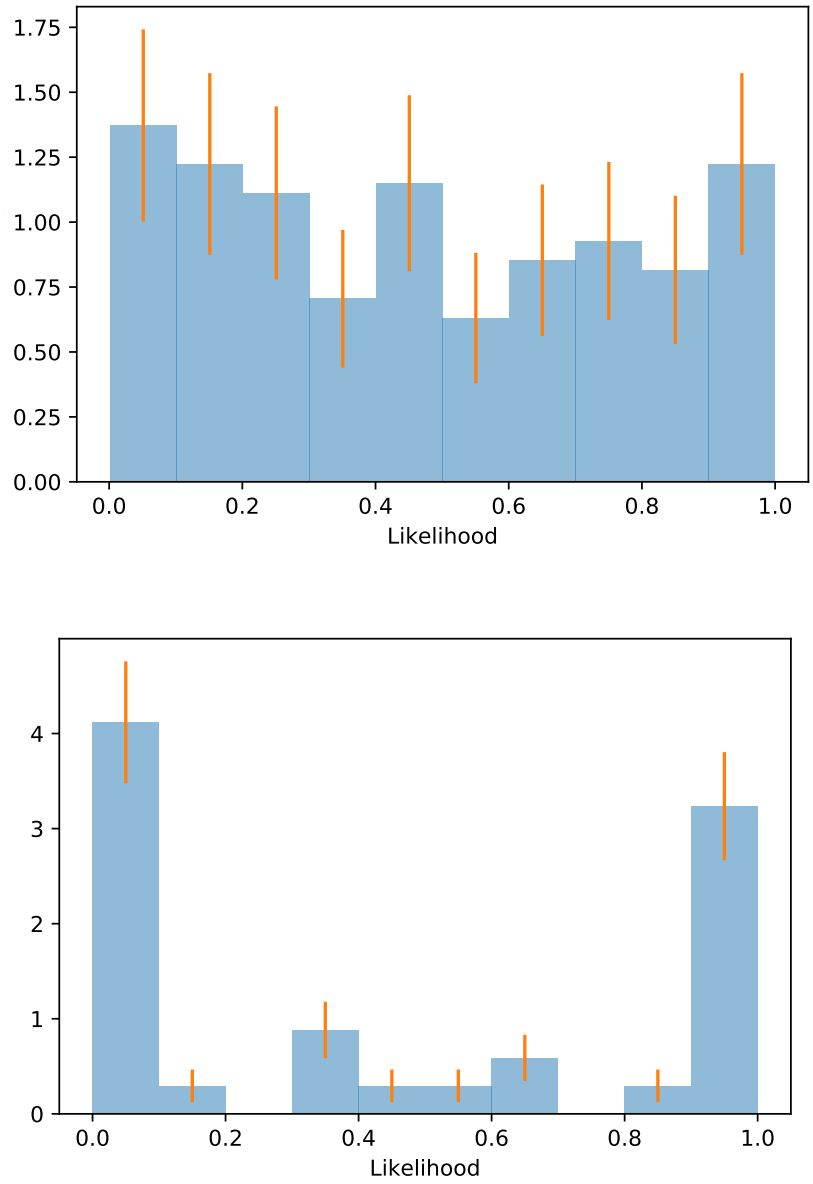


Figure 8.13: Histogram (normalised to 1) of Gaussian one-sided likelihood of D_i. Before (above) and during (below) a period of deliberate convection.

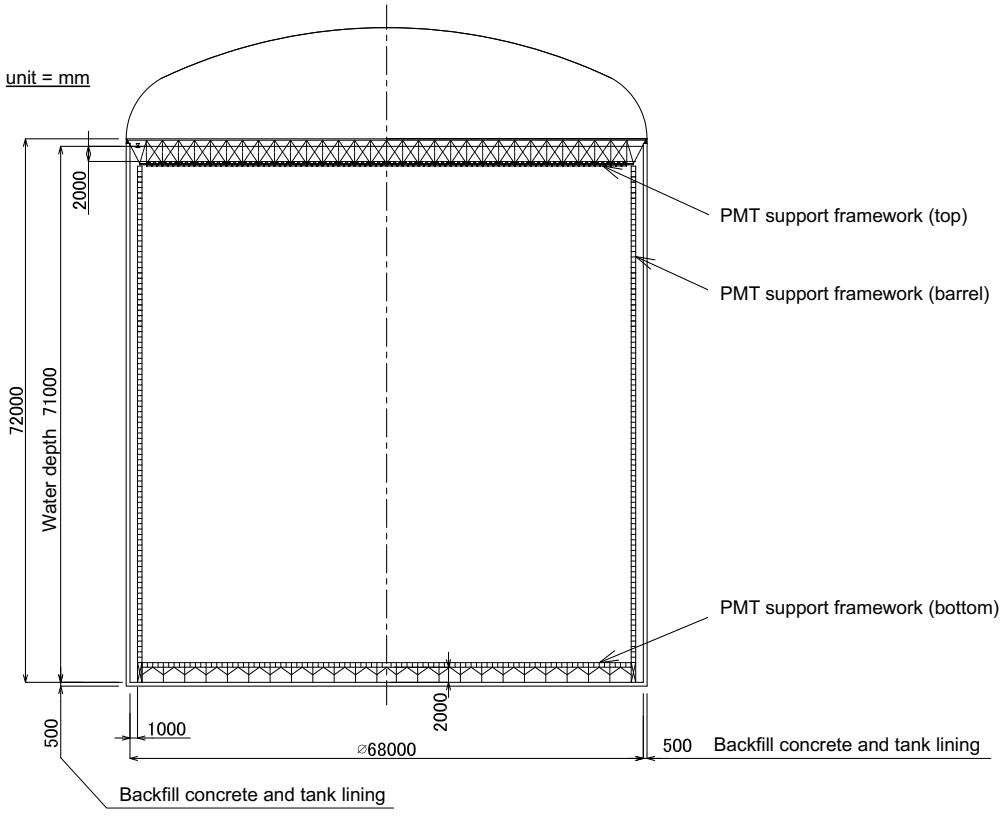


Figure 8.14: Cross sectional dimensions of a Hyper-Kamiokande water tank.

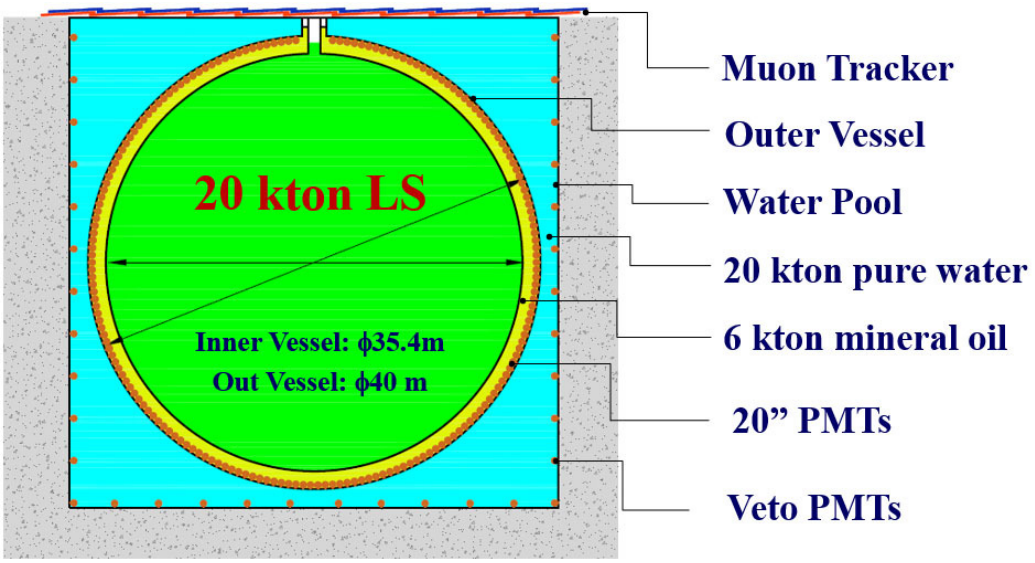
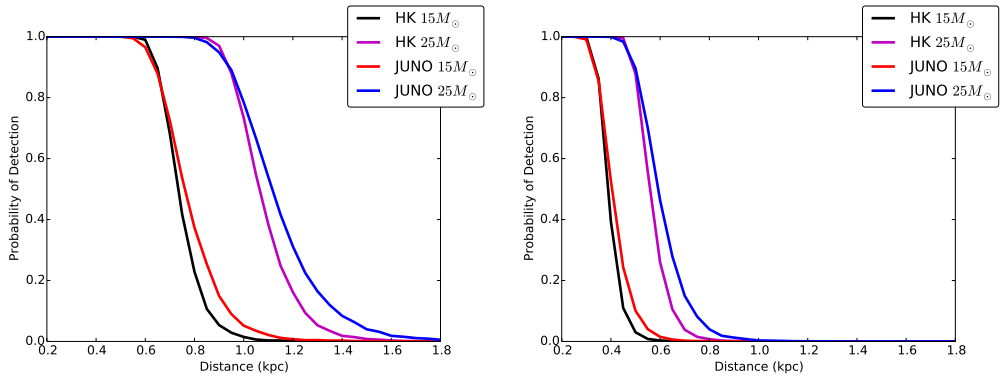


Figure 8.15: Schematic cross section of JUNO, reproduced from JUNO CDR [119].

For the sake of simplicity, a 48 hour time window is used for JUNO and a 6 hour window for Hyper-K, which may not be optimal.

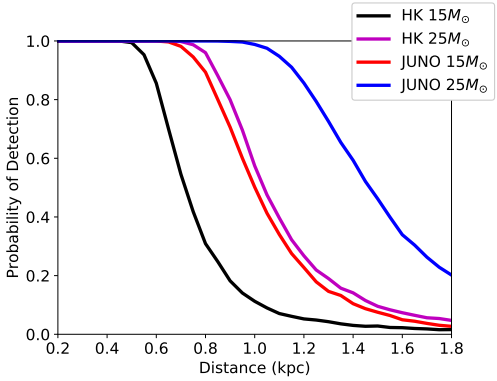
The probability of detection is plotted against distances for JUNO and and HK in Figure 8.16. By this estimate, both JUNO and Hyper-K will be able to achieve detection ranges in excess of 1 kpc.

A future dark-matter direct-detection experiment could also detect significant numbers of pre-SN neutrinos through coherent scattering, with the advantage of being sensitive to all flavours. An O(100 ton) liquid-argon based detector could detect O(10-100) events from α Ori, and provide an alarm up to 10 hours in advance of a CCSN [120].

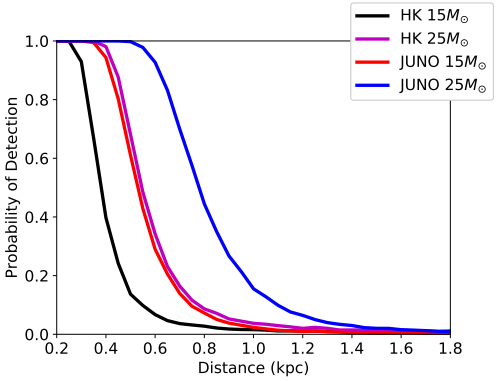


(a) NO, FPR=1/cy.

(b) IO, FPR=1/cy.



(c) NO, FPR=1/year



(d) IO, FPR=1/year

Figure 8.16: Expected maximum range of detection of pre-SN $\overline{\nu}_e$ for Hyper-K and JUNO, for 15 $M_\odot$ and 25 $M_\odot$ stars.

8.9 Combining Multiple Detectors

By combining the signal in multiple neutrino detectors it would be possible to extend detection range considerably.

It is reasonable to assume that backgrounds at the SK-Gd and KamLAND will be fully independent of each other provided the reactor neutrino background is small compared to the intrinsic background at SK-Gd. In this case the estimated null hypothesis likelihood can be calculated for a set of detectors as the product of the null hypothesis likelihoods of all detectors.

A simplified calculation was performed assuming the same signal and background assumptions as in section 8.8. The range was increased until the null hypothesis likelihood for the expected signal rate fell below a threshold. The thresholds used were equivalent to FPRs of 1 per year and 1 per century. The issue of not-quite-equal trial frequency was ignored. The result is tabulated in Table 8.7, showing that considerable gains in maximum range can be achieved by combining detectors.

Detector combination	Range (pc) with FPR	
	∼1/y.	∼1/cy.
SK only	630	490
KL only	710	540
SK+KL	840	630
HK	1000	810
JUNO	1620	1320
HK+JUNO	1870	1450

Table 8.7: Simplified range calculations for combined signal of multiple detectors.

Chapter 9

Conclusion

It is expected that electron anti-neutrinos from a pre-SN star precede those from a CCSN by hours or days, increasing in flux and energy rapidly over a period of hours: this, however, has never been detected. In the next stage of SK, gadolinium loading will enable efficient identification of neutrons, enabling the reduction in the energy threshold for the detection of $\overline{\nu}_{\mathrm{e}}$.

The background rates and signal efficiencies for an SK-Gd low energy analysis capable of detecting pre-SN $\overline{\nu}_{\mathrm{e}}$ have been quantified. This requires detection of events below the usual energy thresholds of SK, for which trigger efficiency and reconstruction are poorer, and backgrounds higher. Gadolinium loading is essential to detecting these events. Through a rapid increase in the number of event candidates, additional warning of a very nearby SN can be achieved, and useful information provided about late stellar burning processes that lead up to a supernova.

Based on this and the predicted fluxes of [43] and [37], estimates were produced of the distance at which a pre-SN star could be observed, and the

amount of additional early warning that could be expected. Gadolinium sulfate loading was assumed to be 0.2% by mass. Uncertainty in the future capabilities of the detector arises mainly from the future internal contamination of the SK detector, which is the main source of backgrounds at low energy. This uncertainty will be reduced once in-situ measurements of background become available. An inverted neutrino mass ordering would have a detrimental effect on the range of this technique by reducing the $\overline{\nu}_e$ fraction of the $\overline{\nu}$ flux leaving the star.

The nearest red supergiant star to Earth is α Ori, which is assumed to have an initial mass of 15-25$M_\odot$ and distance from Earth of 150-250 pc. Assuming normal neutrino mass ordering, 0.2% gadolinium sulfate loading at SK, α Ori going pre-SN could lead to the detection of more than 200 events in SK-Gd in the final 12 hours before core collapse, well exceeding the expected background. Assuming a statistical false positive rate of 1 per century, if it were pre-SN, α Ori could be detected 3 to 10 hours before core collapse, and the greatest distance at which a pre-SN star could be detected is 500 pc. Allowing a higher false positive rate of 1 per year, 5 to 14 hours of early warning could be achieved for α Ori, and maximum detection range could extend to 600 pc. With a lower gadolinium sulfate loading level (0.02% by mass), the maximum range and maximum amount of early warning are reduced.

A pre-SN alert can be provided by SK to the astrophysics community following gadolinium loading. Future large neutrino detectors will improve the potential range of detection, especially if they have a sufficiently small low energy threshold and the ability to tag neutrons from IBD. It could also

be possible to use multiple detectors in combination to provide a pre-SN alert with higher confidence or at increased range.

Appendices

Appendix A

Catalogue of Nearby RSGs

Name	Distance (kpc) (kpc)	V-band magnitude	Spectral type	Alt. name
HD 206778	0.15	2.39	K2 Ib	epsilon Peg
HD 148478	0.16	0.91	M1 Ib	alpha Sco
HD 78647	0.19	2.21	K5 Ib	lambda Vel
HD 39801	0.2	0.42	M2 I	alpha Ori
HD 210745	0.2	3.35	K1.5 I	zeta Cep
HD 89388	0.36	3.38	K5 Ib	q Car
HD 36389	0.37	4.33	M2 I	119 Tau
HD 93070	0.39	4.58	K3 Ib	w Car
HD 196093	0.39	4.66	K2 Ib + B	47 Cyg
HD 200905	0.39	3.73	K4.5 I	xi Cyg
HD 68553	0.42	4.42	K3 Ib	h^1 Pup
HD 56577	0.44	4.79	K3 Ib	145 CMa
HD 62576	0.44	4.59	K3 Ib	1 Pup

HD 50877	0.48	3.87	K2.5 I	o^1 CMa
HD 52877	0.48	3.47	M1.5 I	sigma CMa
HD 160371	0.48	5.6	K2.5 I	BM Sco
HD 80108	0.54	5.13	K3 Ib	HR 3692
HD 207089	0.6	5.28	K0 Ib	12 Peg
HD 213310	0.6	4.37	M0 II	5 Lac
HD 214806	0.6	6.85	M0	V418 Lac
HD 216946	0.6	4.94	M0 I	V424 Lac
HD 217694	0.6	7.3	K4 III	
BD+48 3958	0.6	10.07	M6	ES And
HD 44537	0.71	4.75	M0 I	psi^1 Aur
HD 52005	0.71	5.69	K5 I	41 Gem
HD 137709	0.71	5.26	K5 Ib	HR 5742
HD 205349	0.79	6.25	K1 I	HR 8248
HD 239978	0.79	9.7	M3 I	ST Cep
HD 196725	0.86	5.71	K3 Ib	theta Del
HD 202380	0.87	6.62	M2 I	V419 Cep
HD 203338	0.87	5.75	M1ep Ib + B	
HD 204409	0.87	10.8	M	SW Cep
V577 Cep	0.87	12.8	M7?	
HD 206936	0.87	4.08	M1 I	mu Cep
RT Cep	0.87	11.7 (B)	M6	
HD 208816	0.87	4.9	M2Ia-Iab	VV Cep
BD+58 2396	0.87	10.03	M1 III	AZ Cep

CK Cep	0.87	11.6	M7	
HD 219978	0.87	6.74	M1 I	V809 Cas
HD 17958	1	6.22	K2 I	HR 861
HD 42474	1	7.38	M2 eIab + B	WY Gem
HD 4817	1.05	6.18	K5 Ib	HR 237
HD 37387	1.1	7.53	K1 Ib	
HD 58061	1.14	7.95	M3e Iab	VY CMa
HD 185622	1.14	6.39	M0 Iab-Ib	V340 Sge
HD 11092	1.25	6.57	K5 Iab-Ib	
BD+39 4208	1.32	8	M3 I	RW Cyg
HD 33299	1.38	6.69	K1 I	
HD 35601	1.38	7.32	M1.5 I	V362 Aur
HD 37536	1.38	6.21	M2 I	NO Aur
HD 42475	1.38	6.56	M1 I	TV Gem
HD 42543	1.38	6.39	M0 I	6 Gem
CD-53 6474	1.45	8.79	K2 I	
CPD-53 7364	1.45	9.13	K2 I	
CPD-53 7366	1.45	9.69	K3 Ib	IDS 16052-53
HD 165674	1.5	6.52	M4 Ia	VX Sgr
HD 155603	1.51	6.44	K0 0-Ia	HR 6392
HD 163428	1.58	6.65	K5 Ib	
BD+35 4077	1.58	9.72	M2.5 I	V1749 Cyg
BD+36 4025	1.58	8.4	M3-M4 I	BI Cyg
BD+37 3903	1.58	11.3	M3 I	BC Cyg

KY Cyg	1.58	13.5	M3-M4 I	
HD 90586	1.8	6.93	M2 Iab	V348 Vel
HD 44391	1.82	7.68	K0 Ib	
HD 45829	1.86	6.71	K0 Iab	
HD 207991	1.9	6.88	K5 Ib	
HD 236915	1.91	8.38	M2 I	V778 Cas
BD+59 372	1.91	9.39	K5-M0 I	
HD 12401	1.91	8.2	M4 Ib	XX Per
HD 236947	1.91	8.63	M2 Iab-Ib	
HD 13136	1.91	7.74	M2 Iab	KK Per
HD 13658	1.91	8.92	M1 Iab	V550 Per
BD+57 530a	1.91	9.94	M0 Iab0Ib	BD+57 530
BD+57 530a	1.91	9.16	M0 Iab-Ib	PP Per
BD+56 512	1.91	10.4	M3 I	BU Per
HD 14142	1.91	8.45	M2 Iab	T Per
HD 14242	1.91	8.36	M2 Iab	V605 Cas
HD 14270	1.91	7.88	M3 Iab	AD Per
HD 14330	1.91	7.96	M1 Iab	FZ Per
HD 14404	1.91	8	M2 Iab	PR Per
HD 14469	1.91	9.4	M3-M4 I	SU Per
HD 14528	1.91	7.9	M4.5 I	S Per
BD+56 595	1.91	8.18	M1 I	V439 Per
HD 14580	1.91	8.47	M1 I	V403 Per
HD 14826	1.91	8.22	M2 I	V441 Per

HD 236979	1.91	10.01	M2 I	YZ Per
BD+58 501	1.91	11.5	M2 Iab	GP Cas
HD 237006	1.91	9.26	M1 Ib + B	
HD 237008	1.91	9.62	M4.5 I	W Per
HD 237010	1.91	9.38	M2 I	V648 Cas
HD 150675	1.91	7.1	K1 Ib	
HD 201065	1.92	7.55	K5 Ib	
BD+00 4064	1.96	8.8	M0 Iab	UW Aql
HD 9366	—	6.9	K3 Ib	
BD+59 420	—	9.38	K5 Ia	
HD 13686	—	7.04	K3 Ib	
HD 16682	—	7.91	M4 II	W Tri
HD 17306	—	7.93	K3 Iab + B	
IO Per	—	13.7 (B)	K2 Iab	
HD 22764	—	5.78	K4 Ib	
HD 23475	—	4.48	M2.5 II	BE Cam
HD 25725	—	8.59	M6 II	V Eri
HD 48640	—	6.93	K1 Ib	
HD 49331	—	5.11	M2 IIab	HR 2508
HD 63302	—	6.33	K2 I	QY Pup
HD 65412	—	7.12	M2.5 Iab	V407 Pup
HD 73766	—	7.87	M5 II	RV Hya
HD 300933	—	8.29	M2 Iab-Ib + B	
CD-57 3502	—	10.86	M1.5 Iab-Ib	

CD-59 4459	—	7.66	M2 Iab	DU Cru
HD 143796	—	7.31	M2 Iab-Ib	V362 Nor
HD 144386	—	6.88	K5 Ib	V365 Nor
CD-44 11324	—	9.38	M0 Ib	
HD 326947	—	8.62	M1 Ib	
HD 155161	—	8.1	M5 Ia-Iab	AH Sco
HD 156014	—	3.06	M5 I	alpha Her
HD 160810	—	6.96	M0 Ib	
HD 163755	—	5.03	M2 Ib-II	
HD 163869	—	8.99	M5 Iab	V540 Sgr
HD 312919	—	9.4	M2.5 Ib	
FR Sct	—	11.6	M2.5 Iab + B	
BD-12 5055	—	11.2	M3 Iab	UY Sct
HD 172380	—	6.05	M4-5 II	XY Lyr
HD 175309	—	7.44	M5 II	V913 Aql
HD 175588	—	4.3	M4 II	delta^2 Lyr
HD 181475	—	6.96	M1 II	
HD 193469	—	6.3	K5 Ib	
HD 197812	—	6.38	M5-6 II	U Del
BD+45 3349	—	8.85	M2-4 Iab	AZ Cyg
HD 200527	—	6.23	M3 Ib-II	V1981 Cyg
HD 218942	—	9.16	M6 II	SS And

Table A.1: List of nearby red supergiant candidates, with distance estimates when available. Those with distance estimates > 2 *kpc* in the original table have been omitted for brevity. Reproduced from Nakamura et al. [65]. Note that red supergiants are not the only candidates for supernova progenitors.

Bibliography

[1] A. Strumia and F. Vissani, "Precise quasielastic neutrino/nucleon cross-section," *Phys. Lett.* **B564** (2003) 42–54, arXiv:astro-ph/0302055 [astro-ph].

[2] **Super-Kamiokande** Collaboration, K. Abe *et al.*, "Solar neutrino results in Super-Kamiokande-III," *Phys. Rev.* **D83** (2011) 052010, arXiv:1010.0118 [hep-ex].

[3] **Super-Kamiokande** Collaboration, C. Simpson *et al.*, "Sensitivity of Super-Kamiokande with Gadolinium to Low Energy Antineutrinos from Pre-supernova Emission," *Astrophys. J.* **885** (2019) 133, arXiv:1908.07551 [astro-ph.HE].

[4] W. Pauli, "Dear radioactive ladies and gentlemen," *Phys. Today* **31N9** (1978) 27.

[5] H. Bethe and R. Peierls, "The 'neutrino'," *Nature* **133** (1934) 532.

[6] E. Fermi, "Trends to a Theory of beta Radiation. (In Italian)," *Nuovo Cim.* **11** (1934) 1–19. [,535(1934)].

[7] E. Fermi, "An attempt of a theory of beta radiation. 1.," *Z. Phys.* **88** (1934) 161–177.

[8] S. L. Glashow, "Partial Symmetries of Weak Interactions," *Nucl. Phys.* **22** (1961) 579–588.

[9] S. Weinberg, "A Model of Leptons," *Phys. Rev. Lett.* **19** (1967) 1264–1266.

[10] A. Salam, "Weak and Electromagnetic Interactions," *Conf. Proc.* **C680519** (1968) 367–377.

[11] F. Reines, C. L. Cowan, F. B. Harrison, A. D. McGuire, and H. W. Kruse, "Detection of the free anti-neutrino," *Phys. Rev.* **117** (1960) 159–173.

[12] **Particle Data Group** Collaboration, M. Tanabashi *et al.*, "Review of Particle Physics," *Phys. Rev.* **D98** no. 3, (2018) 030001.

[13] T. Kajita, "Nobel Lecture: Discovery of atmospheric neutrino oscillations," *Rev. Mod. Phys.* **88** no. 3, (2016) 030501.

[14] A. B. McDonald, "Nobel Lecture: The Sudbury Neutrino Observatory: Observation of flavor change for solar neutrinos," *Rev. Mod. Phys.* **88** no. 3, (2016) 030502.

[15] **Super-Kamiokande** Collaboration, Y. Fukuda *et al.*, "Evidence for oscillation of atmospheric neutrinos," *Phys. Rev. Lett.* **81** (1998) 1562–1567, `arXiv:hep-ex/9807003 [hep-ex]`.

[16] **SNO** Collaboration, Q. R. Ahmad *et al.*, "Measurement of the rate of $\nu_e + d \to p + p + e^-$ interactions produced by ^8B solar neutrinos at the Sudbury Neutrino Observatory," *Phys. Rev. Lett.* **87** (2001) 071301, `arXiv:nucl-ex/0106015 [nucl-ex]`.

[17] K. S. Hirata *et al.*, "Observation in the Kamiokande-II Detector of the Neutrino Burst from Supernova SN 1987a," *Phys. Rev.* **D38** (1988) 448–458.

[18] **IMB** Collaboration, C. B. Bratton *et al.*, "Angular Distribution of Events From Sn1987a," *Phys. Rev.* **D37** (1988) 3361.

[19] E. N. Alekseev, L. N. Alekseeva, I. V. Krivosheina, and V. I. Volchenko, "Detection of the Neutrino Signal From SN1987A in the LMC Using the Inr Baksan Underground Scintillation Telescope," *Phys. Lett.* **B205** (1988) 209–214.

[20] G. L. Fogli, E. Lisi, A. Mirizzi, and D. Montanino, "Probing supernova shock waves and neutrino flavor transitions in next-generation water-Cerenkov detectors," *JCAP* **0504** (2005) 002, `arXiv:hep-ph/0412046 [hep-ph]`.

[21] P. Vogel and J. F. Beacom, "Angular distribution of neutron inverse beta decay, anti-neutrino(e) + p —> e+ + n," *Phys. Rev.* **D60** (1999) 053003, `arXiv:hep-ph/9903554 [hep-ph]`.

[22] **ALEPH, DELPHI, L3, OPAL, SLD, LEP Electroweak Working Group, SLD Electroweak Group, SLD Heavy**

Flavour Group Collaboration, S. Schael *et al.*, "Precision electroweak measurements on the Z resonance," *Phys. Rept.* **427** (2006) 257–454, `arXiv:hep-ex/0509008 [hep-ex]`.

[23] N. Cabibbo, "Unitary Symmetry and Leptonic Decays," *Phys. Rev. Lett.* **10** (1963) 531–533. [,648(1963)].

[24] M. Kobayashi and T. Maskawa, "CP Violation in the Renormalizable Theory of Weak Interaction," *Prog. Theor. Phys.* **49** (1973) 652–657.

[25] P. F. de Salas, D. V. Forero, C. A. Ternes, M. Tortola, and J. W. F. Valle, "Status of neutrino oscillations 2018: 3σ hint for normal mass ordering and improved CP sensitivity," *Phys. Lett.* **B782** (2018) 633–640, `arXiv:1708.01186 [hep-ph]`.

[26] H. A. Bethe, "Possible explanation of the solar-neutrino puzzle," *Phys. Rev. Lett.* **56** (Mar, 1986) 1305–1308. `https://link.aps.org/doi/10.1103/PhysRevLett.56.1305`.

[27] J. P. Kneller, G. C. McLaughlin, and J. Brockman, "Oscillation Effects and Time Variation of the Supernova Neutrino Signal," *Phys. Rev.* **D77** (2008) 045023, `arXiv:0705.3835 [astro-ph]`.

[28] S. E. Woosley, A. Heger, and T. A. Weaver, "The evolution and explosion of massive stars," *Rev. Mod. Phys.* **74** (2002) 1015–1071.

[29] T. A. Kirsten, "Solar neutrino experiments: Results and implications," *Rev. Mod. Phys.* **71** (1999) 1213–1232.

[30] The IceCube Collaboration, Fermi-LAT, MAGIC, *et al.*, "Multimessenger observations of a flaring blazar coincident with high-energy neutrino icecube-170922a," *Science* (2018) , http://science.sciencemag.org/content/early/2018/07/11/science.aat1378.

[31] **Super-Kamiokande** Collaboration, K. Abe *et al.*, "Real-Time Supernova Neutrino Burst Monitor at Super-Kamiokande," *Astropart. Phys.* **81** (2016) 39–48, arXiv:1601.04778 [astro-ph.HE].

[32] P. Antonioli *et al.*, "SNEWS: The Supernova Early Warning System," *New J. Phys.* **6** (2004) 114, arXiv:astro-ph/0406214 [astro-ph].

[33] J. F. Beacom and P. Vogel, "Can a supernova be located by its neutrinos?," *Phys. Rev.* **D60** (1999) 033007, arXiv:astro-ph/9811350 [astro-ph].

[34] A. Odrzywolek, M. Misiaszek, and M. Kutschera, "Future neutrino observations of nearby presupernova stars before corecollapse," *AIP Conference Proceedings* **944** no. 1, (2007) 109–118. http://aip.scitation.org/doi/abs/10.1063/1.2818538.

[35] C. Kato, M. D. Azari, S. Yamada, *et al.*, "Pre-supernova neutrino emissions from ONe cores in the progenitors of core-collapse supernovae: are they distinguishable from those of Fe cores?," *Astrophys. J.* **808** no. 2, (2015) 168, arXiv:1506.02358 [astro-ph.HE].

[36] T. Yoshida, K. Takahashi, H. Umeda, and K. Ishidoshiro, "Presupernova neutrino events relating to the final evolution of

massive stars," *Phys. Rev.* **D93** no. 12, (2016) 123012, arXiv:1606.04915 [astro-ph.HE].

[37] K. M. Patton, C. Lunardini, R. J. Farmer, and F. X. Timmes, "Neutrinos from beta processes in a presupernova: probing the isotopic evolution of a massive star," arXiv:1709.01877 [astro-ph.HE].

[38] V. Barger, P. Huber, and D. Marfatia, "Supernova neutrinos can tell us the neutrino mass hierarchy independently of flux models," *Phys. Lett.* **B617** (2005) 167–173, arXiv:hep-ph/0501184 [hep-ph].

[39] K. Scholberg, "Supernova Neutrino Detection," *Ann. Rev. Nucl. Part. Sci.* **62** (2012) 81–103, arXiv:1205.6003 [astro-ph.IM].

[40] K. Scholberg, "Supernova Signatures of Neutrino Mass Ordering," *J. Phys.* **G45** no. 1, (2018) 014002, arXiv:1707.06384 [hep-ex].

[41] H. Duan, G. M. Fuller, and Y.-Z. Qian, "Collective Neutrino Oscillations," *Ann. Rev. Nucl. Part. Sci.* **60** (2010) 569–594, arXiv:1001.2799 [hep-ph].

[42] E. Akhmedov, J. Kopp, and M. Lindner, "Collective neutrino oscillations and neutrino wave packets," *JCAP* **1709** no. 09, (2017) 017, arXiv:1702.08338 [hep-ph].

[43] A. Odrzywolek and A. Heger, "Neutrino signatures of dying massive stars: From main sequence to the neutron star," *Acta Physica Polonica B* **41** (July, 2010) .

[44] **KamLAND** Collaboration, K. Asakura *et al.*, "KamLAND Sensitivity to Neutrinos from Pre-Supernova Stars," *Astrophys. J.* **818** no. 1, (2016) 91, arXiv:1506.01175 [astro-ph.HE].

[45] W. Li, R. Chornock, J. Leaman, *et al.*, "Nearby Supernova Rates from the Lick Observatory Supernova Search. III. The Rate-Size Relation, and the Rates as a Function of Galaxy Hubble Type and Colour," *Mon. Not. Roy. Astron. Soc.* **412** (2011) 1473, arXiv:1006.4613 [astro-ph.SR].

[46] S. M. Adams, C. S. Kochanek, J. F. Beacom, M. R. Vagins, and K. Z. Stanek, "Observing the Next Galactic Supernova," *Ap.J.* **778** (2013) 164, arXiv:1306.0559 [astro-ph.HE].

[47] W. D. Arnett, J. N. Bahcall, R. P. Kirshner, and S. E. Woosley, "SUPERNOVA SN1987A," *Ann. Rev. Astron. Astrophys.* **27** (1989) 629–700.

[48] C. Giunti and C. W. Kim, *Fundamentals of Neutrino Physics and Astrophysics*. Oxford Univ. Pr., 2007.

[49] A. Odrzywolek, M. Misiaszek, and M. Kutschera, "Detection possibility of the pair-annihilation neutrinos from the neutrino-cooled pre-supernova star," *Astropart. Phys.* **21** (2004) 303–313, arXiv:astro-ph/0311012 [astro-ph].

[50] K. M. Patton, C. Lunardini, and R. J. Farmer, "Presupernova neutrinos: realistic emissivities from stellar evolution," *Astrophys. J.* **840** no. 1, (2017) 2, arXiv:1511.02820 [astro-ph.SR].

[51] V. Trimble, "1987A: The greatest supernova since Kepler," *Rev. Mod. Phys.* **60** (1988) 859–871.

[52] K. Nakazato, K. Sumiyoshi, H. Suzuki, *et al.*, "Supernova Neutrino Light Curves and Spectra for Various Progenitor Stars: From Core Collapse to Proto-neutron Star Cooling," *Astrophys. J. Suppl.* **205** (2013) 2, arXiv:1210.6841 [astro-ph.HE].

[53] G. Sonneborn, B. Altner, and R. P. Kirshner, "The progenitor of SN 1987A - Spatially resolved ultraviolet spectroscopy of the supernova field," *Ap.J.Lett.* **323** (Dec., 1987) L35–L39.

[54] D. N. Schramm and J. W. Truran, "New physics from supernova 1987a," *Physics Reports* **189** no. 2, (1990) 89 – 126. http://www.sciencedirect.com/science/article/pii/0370157390900203.

[55] T. J. Loredo and D. Q. Lamb, "Bayesian analysis of neutrinos observed from supernova SN 1987A," *PRD* **65** no. 6, (Mar, 2002) 063002, arXiv:astro-ph/0107260 [astro-ph].

[56] S. Horiuchi, J. F. Beacom, and E. Dwek, "The Diffuse Supernova Neutrino Background is detectable in Super-Kamiokande," *Phys. Rev.* **D79** (2009) 083013, arXiv:0812.3157 [astro-ph].

[57] **Super-Kamiokande** Collaboration, H. Zhang *et al.*, "Supernova Relic Neutrino Search with Neutron Tagging at Super-Kamiokande-IV," *Astropart. Phys.* **60** (2015) 41–46, arXiv:1311.3738 [hep-ex].

[58] **Super-Kamiokande** Collaboration, K. Bays *et al.*, "Supernova Relic Neutrino Search at Super-Kamiokande," *Phys. Rev.* **D85** (2012) 052007, arXiv:1111.5031 [hep-ex].

[59] **LBNE** Collaboration, T. Akiri *et al.*, "The 2010 Interim Report of the Long-Baseline Neutrino Experiment Collaboration Physics Working Groups," arXiv:1110.6249 [hep-ex].

[60] H. Zhang, *Study of Low Energy Electron Anti-neutrinos at Super-Kamiokande IV*. PhD thesis, Tsinghua University, 2012. http://www-sk.icrr.u-tokyo.ac.jp/sk/publications. Tsinghua University, Ph.D. Thesis.

[61] J. F. Beacom and M. R. Vagins, "GADZOOKS! Anti-neutrino spectroscopy with large water Cherenkov detectors," *Phys. Rev. Lett.* **93** (2004) 171101, arXiv:hep-ph/0309300 [hep-ph].

[62] A. Odrzywolek, "Pre Supernova Neutrino Spectrum." http://web.archive.org/web/20181109002141/http://th.if.uj.edu.pl/~odrzywolek/psns/, Web.

[63] K. M. Patton, C. Lunardini, R. J. Farmer, and F. X. Timmes, "Neutrinos from Beta Processes in a Presupernova: Probing the Isotopic Evolution of a Massive Star." Data table, Apr., 2019. https://doi.org/10.5281/zenodo.2626645.

[64] A. Odrzywolek, "Nuclear statistical equilibrium neutrino spectrum," *Phys.Rev. C* **80** no. 4, (Oct., 2009) 045801, arXiv:0903.2311 [astro-ph.SR].

[65] K. Nakamura, S. Horiuchi, M. Tanaka, *et al.*, "Multimessenger signals of long-term core-collapse supernova simulations: synergetic observation strategies," *Mon. Not. Roy. Astron. Soc.* **461** no. 3, (2016) 3296–3313, arXiv:1602.03028 [astro-ph.HE].

[66] P. A. Cerenkov, "Visible radiation produced by electrons moving in a medium with velocities exceeding that of light," *Phys. Rev.* **52** (1937) 378–379.

[67] S. Fukuda *et al.*, "The Super-Kamiokande detector," *NIM A* **501** no. 2, (2003) 418 – 462. http://www.sciencedirect.com/science/article/pii/S016890020300425X.

[68] M. Ikeda *et al.*, "Evaluation of Gadolinium's Action on Water Cherenkov Detector Systems with EGADS," *submitted to NIM* (2019) , arXiv:1908.11532 [physics.ins-det].

[69] K. Abe *et al.*, "Calibration of the Super-Kamiokande detector," *NIM A* **737** (2014) 253 – 272. http://www.sciencedirect.com/science/article/pii/S016890021301646X.

[70] **Super-Kamiokande** Collaboration, K. Abe *et al.*, "Solar Neutrino Measurements in Super-Kamiokande-IV," *Phys. Rev.* **D94** no. 5, (2016) 052010, arXiv:1606.07538 [hep-ex].

[71] Y. Takeuchi *et al.*, "Measurement of radon concentrations at super-kamiokande," *Physics Letters B* **452** no. 3, (1999) 418 – 424. http://www.sciencedirect.com/science/article/pii/S0370269399003111.

[72] Y. Nakano, H. Sekiya, S. Tasaka, *et al.*, "Measurement of radon concentration in super-kamiokandes buffer gas," *NIM A* **867** (2017) 108 – 114. http://www.sciencedirect.com/science/article/pii/S0168900217305004.

[73] **Super-Kamiokande** Collaboration, J. Hosaka *et al.*, "Solar neutrino measurements in super-Kamiokande-I," *Phys. Rev.* **D73** (2006) 112001, arXiv:hep-ex/0508053 [hep-ex].

[74] T. Tanimori, H. Ikeda, M. Mori, *et al.*, "Design and performance of semi-custom analog IC including two TACs and two current integrators for 'Super-Kamiokande'," *IEEE Transactions on Nuclear Science* **36** no. 1, (Feb, 1989) 497–501.

[75] H. Nishino, K. Awai, Y. Hayato, *et al.*, "High-speed charge-to-time converter ASIC for the Super-Kamiokande detector," *NIM A* **610** no. 3, (2009) 710 – 717. http://www.sciencedirect.com/science/article/pii/S0168900209017495.

[76] S. Yamada, Y. Hayato, Y. Obayashi, and M. Shiozawa, "New online system without hardware trigger for the Super-Kamiokande experiment," in *2007 IEEE Nuclear Science Symposium Conference Record*, vol. 1, pp. 111–114. Oct, 2007.

[77] G. Carminati, "The new wide-band solar neutrino trigger for super-kamiokande," *Physics Procedia* **61** (2015) 666 – 672. http://www.sciencedirect.com/science/article/pii/

S1875389214006816. 13th International Conference on Topics in Astroparticle and Underground Physics, TAUP 2013.

[78] **Super-Kamiokande** Collaboration, K. Abe *et al.*, "Real-Time Supernova Neutrino Burst Monitor at Super-Kamiokande," *Astropart. Phys.* **81** (2016) 39–48, arXiv:1601.04778 [astro-ph.HE].

[79] M. Nakahata, Y. Fukuda, T. Hayakawa, *et al.*, "Calibration of super-kamiokande using an electron linac: The super-kamiokande collaboration," *Nuclear Instruments and Methods in Physics Research Section A: Accelerators, Spectrometers, Detectors and Associated Equipment* **421** no. 1, (1999) 113 – 129. http://www.sciencedirect.com/science/article/pii/S0168900298012005.

[80] E. Blaufuss, G. Guillian, Y. Fukuda, *et al.*, "16n as a calibration source for super-kamiokande," *Nuclear Instruments and Methods in Physics Research Section A: Accelerators, Spectrometers, Detectors and Associated Equipment* **458** no. 3, (2001) 638 – 649. http://www.sciencedirect.com/science/article/pii/S0168900200009001.

[81] **SUPERKAMIOKANDE** Collaboration, M. Smy, "Low Energy Event Reconstruction and Selection in Super-Kamiokande-III," in *Proceedings, 30th International Cosmic Ray Conference (ICRC 2007): Merida, Yucatan, Mexico, July 3-11, 2007*, vol. 5, pp. 1279–1282. 2007. http://indico.nucleares.unam.mx/contributionDisplay.py?contribId=213&confId=4.

[82] J. A. Dunmore, *The Separation of CC and NC Events in the Sudbury Neutrino Observatory*. PhD thesis, University of Oxford, 2004. `https://sno.phy.queensu.ca/sno/publications.html`.

[83] T. Mori, *Development of A Gadolinium-doped Water Cherenkov Detector for The Observation of Supernova Relic Neutrinos*. PhD thesis, Okayama University, February, 2015. `http://www-sk.icrr.u-tokyo.ac.jp/sk/_pdf/articles/2015/mori.pdf`. Okayama University, Ph.D. thesis.

[84] **Super-Kamiokande** Collaboration, L. Wan *et al.*, "Measurement of the neutrino-oxygen neutral-current quasielastic cross section using atmospheric neutrinos at Super-Kamiokande," *Phys. Rev.* **D99** no. 3, (2019) 032005, `arXiv:1901.05281 [hep-ex]`.

[85] **SNO** Collaboration, B. Aharmim *et al.*, "Electron energy spectra, fluxes, and day-night asymmetries of B-8 solar neutrinos from measurements with NaCl dissolved in the heavy-water detector at the Sudbury Neutrino Observatory," *Phys. Rev.* **C72** (2005) 055502, `arXiv:nucl-ex/0502021 [nucl-ex]`.

[86] http://commons.wikimedia.org/wiki/User:Tosaka. CC BY 3.0 (https://creativecommons.org/licenses/by/3.0).

[87] http://commons.wikimedia.org/wiki/User:BatesIsBack. CC BY-SA 3.0 (https://creativecommons.org/licenses/by-sa/3.0).

[88] P. Fernandez Menendez, *Neutrino Physics in Present and Future Kamioka Water-Cerenkov Detectors with Neutron Tagging*. PhD

thesis, Autonomous University of Madrid, 2017. http://www-sk.icrr.u-tokyo.ac.jp/sk/publications.

[89] https://commons.wikimedia.org/wiki/User:YassineMrabet. CC BY-SA 4.0 (https://creativecommons.org/licenses/by-sa/4.0/).

[90] **Super-Kamiokande** Collaboration, H. Watanabe *et al.*, "First Study of Neutron Tagging with a Water Cherenkov Detector," *Astropart. Phys.* **31** (2009) 320–328, arXiv:0811.0735 [hep-ex].

[91] S. Valenta, F. Bečvář, J. Kroll, M. Krtička, and I. Tomandl, "Two-step γ cascades following thermal neutron capture in ^{155,157}Gd," *Phys. Rev. C* **92** (Dec, 2015) 064321. https://link.aps.org/doi/10.1103/PhysRevC.92.064321.

[92] S. Agostinelli *et al.*, "Geant4a simulation toolkit," *NIM A* **506** no. 3, (2003) 250 – 303. http://www.sciencedirect.com/science/article/pii/S0168900203013688.

[93] J. Allison *et al.*, "Recent developments in geant4," *NIM A* **835** (2016) 186 – 225. http://www.sciencedirect.com/science/article/pii/S0168900216306957.

[94] K. Zbiri, "Additional gadolinium support for GLG4sim." https://web.archive.org/web/20060907034310/neutrino.phys.ksu.edu/~GLG4sim/Gd.html, 2006. Archived 2006-09-07, but original unavailable.

[95] **2012B0025, 2014B0126** Collaboration, T. Yano, "Measurement of gamma-ray production from thermal neutron capture on gadolinium for neutrino experiments," *Nucl. Instrum. Meth.* **A845** (2017) 425–428.

[96] P. K. Das *et al.*, "Measurement of Relative Intensity of the discrete γ rays from the thermal neutron capture reaction ^{155,157} Gd (n, γ) using ANNRI detector (JPARC)," *PoS* **KMI2017** (2017) 045.

[97] K. Hagiwara *et al.*, "Comparison of γ production from thermal neutron capture of gadolinium with the MonteCarlo simulation," *PoS* **KMI2017** (2017) 035.

[98] I. Ou, T. Yano, Y. Yamada, *et al.*, "Measurement of the Energy, Multiplicity and Angular Correlation of γ-rays from the Thermal Neutron Capture Reaction Gd(n, γ)," *JPS Conf. Proc.* **1** (2014) 013053.

[99] **Super-Kamiokande** Collaboration, G. Carminati, "The new Wide-band Solar Neutrino Trigger for Super-Kamiokande," *Phys. Procedia* **61** (2015) 666–672.

[100] Y. Nakano and The Super-Kamiokande Collaboration, "Radon background study in super-kamiokande," *Journal of Physics: Conference Series* **888** no. 1, (2017) 012191. `http://stacks.iop.org/1742-6596/888/i=1/a=012191`.

[101] W. B. Wilson, R. T. Perry, E. F. Shores, *et al.*, "SOURCES 4C: a code for calculating (α,n), spontaneous fission, and delayed neutron sources and spectra," *LA-UR–02-1839* (Jan, 2002) .

[102] J. Verbeke, C. Hagmann, and D. Wright, "Simulation of neutron and gamma ray emission from fission," *Lawrence Livermore National Laboratory* (March, 2007) .

[103] H. W. Sobel, A. A. Hruschka, W. R. Kropp, *et al.*, "High-Energy Gamma Rays from Spontaneous Fission of ^{238}U," *Phys. Rev. C* **7** (Apr, 1973) 1564–1579. https://link.aps.org/doi/10.1103/PhysRevC.7.1564.

[104] **Super-Kamiokande Collaboration** Collaboration, Y. Zhang *et al.*, "First measurement of radioactive isotope production through cosmic-ray muon spallation in super-kamiokande iv," *Phys. Rev. D* **93** (Jan, 2016) 012004. https://link.aps.org/doi/10.1103/PhysRevD.93.012004.

[105] S. W. Li and J. F. Beacom, "Spallation backgrounds in super-kamiokande are made in muon-induced showers," *Phys. Rev. D* **91** (May, 2015) 105005. https://link.aps.org/doi/10.1103/PhysRevD.91.105005.

[106] S. W. Li and J. F. Beacom, "Tagging Spallation Backgrounds with Showers in Water-Cherenkov Detectors," *Phys. Rev.* **D92** no. 10, (2015) 105033, arXiv:1508.05389 [physics.ins-det].

[107] S. W. Li and J. F. Beacom, "First calculation of cosmic-ray muon spallation backgrounds for mev astrophysical neutrino signals in super-kamiokande," *Phys. Rev. C* **89** (Apr, 2014) 045801. https://link.aps.org/doi/10.1103/PhysRevC.89.045801.

[108] X. Mougeot *Phys.Rev.C* **91** .

[109] B. Singh *et al.*, "ENSDF." From ENSDF database as of february 26, 2019. version available at http://www.nndc.bnl.gov/ensarchivals/.

[110] A. Barna and S. Dye, "Web Application for Modeling Global Antineutrinos," arXiv:1510.05633 [physics.ins-det].

[111] M. Baldoncini, I. Callegari, G. Fiorentini, *et al.*, "Reference worldwide model for antineutrinos from reactors," *Phys. Rev.* **D91** no. 6, (2015) 065002, arXiv:1411.6475 [physics.ins-det].

[112] Y. Huang, V. Chubakov, F. Mantovani, R. L. Rudnick, and W. F. McDonough, "A reference earth model for the heat-producing elements and associated geoneutrino flux," *Geochemistry, Geophysics, Geosystems* **14** no. 6, (2013) 2003–2029, https://agupubs.onlinelibrary.wiley.com/doi/pdf/10.1002/ggge.20129. https://agupubs.onlinelibrary.wiley.com/doi/abs/10.1002/ggge.20129.

[113] IAEA, "Power Reactor Information System (PRIS)," 2018. https://pris.iaea.org/PRIS/About.aspx.

[114] A. Hoecker, P. Speckmayer, J. Stelzer, *et al.*, "TMVA: Toolkit for Multivariate Data Analysis," *PoS* **ACAT** (2007) 040, arXiv:physics/0703039.

[115] A. Hoecker, P. Speckmayer, J. Stelzer, *et al.*, "TMVA - Toolkit for Multivariate Data Analysis," *arXiv e-prints* (Mar, 2007) physics/0703039, arXiv:physics/0703039 [physics.data-an].

[116] G. Pronost, M. Ikeda, T. Nakamura, H. Sekiya, and S. Tasaka, "Development of new radon monitoring systems in the kamioka mine," *Progress of Theoretical and Experimental Physics* **2018** no. 9, (2018) 093H01.

[117] M. M. Dolan, G. J. Mathews, D. D. Lam, *et al.*, "Evolutionary Tracks for Betelgeuse," *Ap. J.* **819** (Mar., 2016) 7, arXiv:1406.3143 [astro-ph.SR].

[118] **Hyper-Kamiokande** Collaboration, K. Abe *et al.*, "Hyper-Kamiokande Design Report," arXiv:1805.04163 [physics.ins-det].

[119] **JUNO** Collaboration, Z. Djurcic *et al.*, "JUNO Conceptual Design Report," arXiv:1508.07166 [physics.ins-det].

[120] N. Raj, V. Takhistov, and S. J. Witte, "Pre-Supernova Neutrinos in Large Dark Matter Direct Detection Experiments," arXiv:1905.09283 [hep-ph].